EXPERIMENTAL AND SIMULATION STUDIES ON PHASE BEHAVIOR OF PETROLEUM FLUIDS IN NANOPOROUS MEDIA

A Dissertation

by

SHENG LUO

Submitted to the Office of Graduate and Professional Studies of
Texas A&M University
in partial fulfillment of the requirements for the degree of

DOCTOR OF PHILOSOPHY

Chair of Committee,	Hadi Nasrabadi
Co-Chair of Committee,	Jodie L. Lutkenhaus
Committee Members,	John Killough
	Eduardo Gildin
Head of Department,	Jeff Spath

December 2018

Major Subject: Petroleum Engineering

ABSTRACT

The phase behavior of petroleum fluids is an important factor in evaluating the hydrocarbon reserves and forecasting the oil and gas production behavior. Due to the existence of nano-scale pores, the fluid phase behavior in unconventional shale reservoirs differs significantly from that in unconventional reservoirs. Practically, the complexities of phase behavior in shale is associated with several factors, such as confinement effect, pore size distribution, surface uncertainty and heterogeneous distribution of hydrocarbon species. Previous work has mostly focused on theoretical studies and simulations. However, there are relatively few experimental data to verify the theories and models. A comprehensive picture of pressure-volume-temperature (PVT) behavior for the confined hydrocarbons remains uncertain.

This study, combined with laboratory and simulation studies, is dedicated to understand fluid phase behavior under nano-confinement effect from both experimental and theoretical aspects. Firstly, we developed an experimental technique of differential scanning calorimetry to measure the hydrocarbon liquid-vapor phase transition temperature in nanopores. Next, the experimental data is used to correlate a pore-size-dependent equation of state (EOS). The confinement parameters in EOS are determined and the EOS is shown to predict experimental results. With the pore-size-dependent EOS, a multi-scale PVT simulator is developed for shale's nano-scale pore size distribution systems. The PVT simulator realistically models the constant composition expansion and

swelling behavior in gas injection for the shale reservoir fluids under macro- to nano-scale porous geometries.

DEDICATION

To my wife Di Fan

ACKNOWLEDGMENTS

I am deeply indebted to my advisor, Professor Hadi Nasrabadi, for the academic guidance and support throughout my Ph.D. study. His continuous encouragement and unreserved guidance has helped me overcome difficulties and are extremely beneficial to my future career.

I would like to sincerely thank my co-advisor, Professor Jodie L. Lutkenhaus, for her thoughtful guidance, innovative ideas and continuous support throughout my study. Without her guidance, I wouldn't be able to complete this doctoral degree.

I would like to express my thanks to Professor John Killough and Professor Eduardo Gildin for serving as my committee members and providing valuable insight.

I would also like to thank Nasrabadi research group members – Bikai Jin, Zachary Ross Benamram, Kingsley Madiebo, Mohammad Al-Dossary, Qi Yang, Ran Bi, David Higuera and Dariya Reid, Fei Li, Yanpu Zhang from Lutkenhaus research group for their discussions and support.

Finally, special thanks to my parents and beloved wife, Di.

CONTRIBUTORS AND FUNDING SOURCES

This work was supported by a dissertation committee consisting of Professor Hadi Nasrabadi [advisor] of the Department of Petroleum Engineering, Professor Jodie L. Lutkenhaus [co-advisor] of the Department of Chemical Engineering, Professor John Killough of the Department of Petroleum Engineering and Professor Eduardo Gildin of the Department of Petroleum Engineering. All the work conducted for the dissertation was completed by the student independently.

This research is sponsored by the Crisman Institute for the Petroleum Research in Texas A&M University.

NOMENCLATURE

a	Conventional energy parameter for PR EOS
A	Helmholtz free energy
a_p	Confinement-modified energy parameter for PR-C EOS
b	Conventional volume parameter for PR EOS
b_p	Confinement-modified volume parameter for PR-C EOS
B_o	Oil formation volume factor
d	Cylindrical pore diameter
f_i^L	Liquid phase fugacity for component i
f_i^V	Vapor phase fugacity for component i
$F_{pr,i}$	Fraction of fluid within the pore surface attractive field under random distribution
k_{ij}	Binary Interaction parameters between component i and j
k_B	Boltzmann constant
MW	Molecular weight
N_{av}	Avogadro's number
NC	Number of components
n_i	Moles of component i
P	Pressure
P_b	Bubble point pressure
P_C	Critical pressure

R	Ideal gas constant
R_s	Solution gas-oil ratio
r_p	Cylindrical pore radius
T	Temperature
T_C	Critical temperature
v	Molar volume
V	Volume
VSP	Volume shift parameter
x_i	Mole fraction of component i
δ_p	Square well depth of fluid-pore wall surface interaction potential
ε_p	Square well depth of fluid-pore wall surface interaction potential
θ	Geometric term in expression of F_p
κ	Fluid-pore surface affinity factor
λ	de Broglie wavelength
μ_i	Chemical potential of component i
ρ	Fluid density
σ_i	Molecular diameter of component i
ω	Acentric factor

TABLE OF CONTENTS

Page

LIST OF FIGURES

Page

LIST OF TABLES

Page

1. INTRODUCTION

1.1 Background

1.1.1 The shale fluid challenge

The productions from unconventional tight/shale reservoirs constitute an important component in petroleum fluids production. In 2017, tight oil productions has contributed to 50% of crude oil production and tight/shale gas production has contributed to almost 70% of natural gas production in United States (Figures 1 and 2). As projected by U.S. Energy Information Administration,[1] the U.S. crude oil and natural gas liquids production will continue to grow through 2050 as a result of the further development of tight oil and shale gas resources, especially under the circumstances of high oil and gas resource technology.

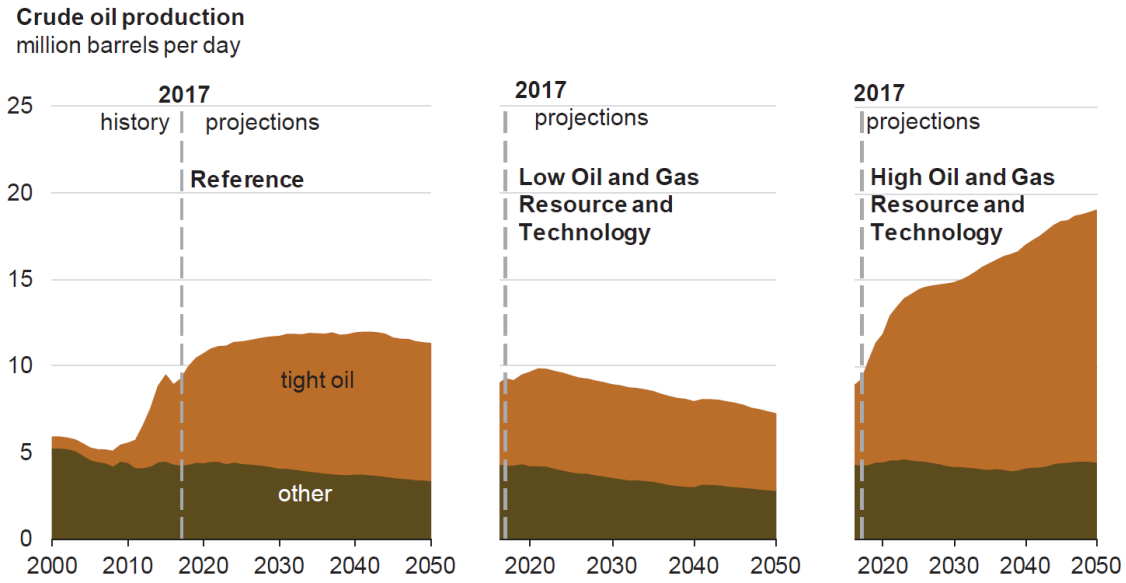

Figure 1. U.S. tight oil productions and projections through 2050 (reprinted from US EIA Annual Energy Outlook 2018).[1]

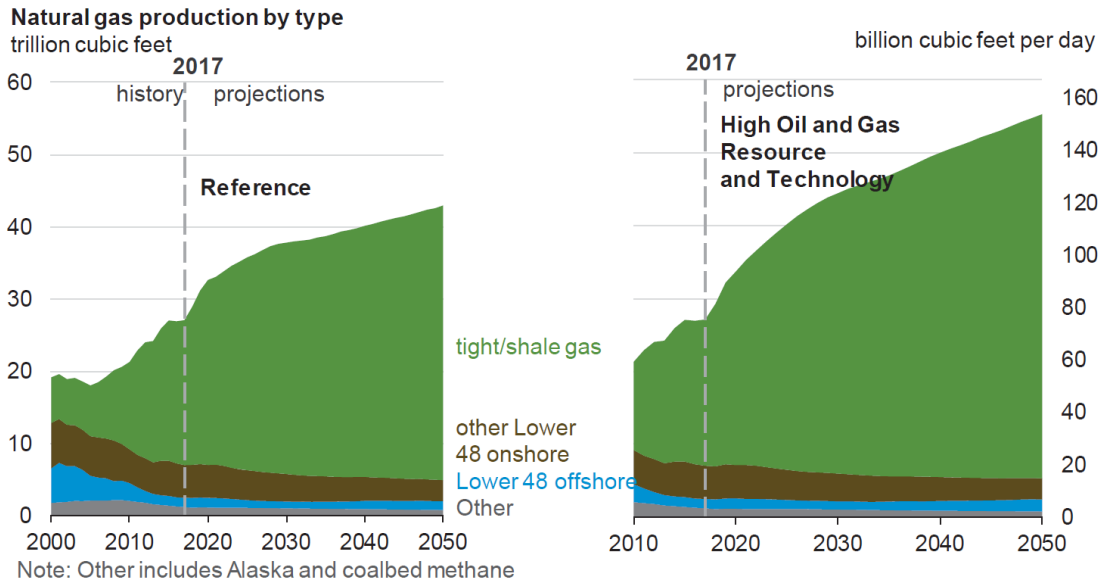

Figure 2. U.S. tight and shale gas productions and projections to 2050 (reprinted from US EIA Annual Energy Outlook 2018).[1]

However, the tight/shale oil and gas productions are poised with many challenges. The wells drilled in unconventional reservoir suffer a rapid production rate decline, and the ultimate oil recovery is very low compared to the recovery from conventional reservoirs. The uncertainty in phase behavior is one of the greatest challenges in developing unconventional shale resources. The complex phase behavior is due to the broad range of pore size distribution in shale. In macro-scale geometries such as fractures and macropores, the fluid behavior is bulk-like; in nano-scale pores, the fluid behavior is significantly altered by confinement effects. In nanopores, the fluid molecules interact with pore surfaces and these interactions can lead to a heterogeneous distribution of molecules, which the conventional bulk-phase thermodynamics fails to describe.

The deviated fluid phase behavior results in disconnections in industrial practice. The current industrial process of fluid PVT characterization utilizes the bulk-scale PVT cell measurement, but PVT for shale reservoirs cannot be measured in bulk-scale PVT cell because the phase behavior is significantly altered from bulk behavior by the nanopores in shale rock. The unknown fluid phase behavior results in two major challenges:[2] firstly, the actual fluid compositions in shale reservoir is unknown; secondly, the behavior of fluids depletes in the shale system is not understood. The latter challenge is associated with fluid flow, with contributes to another dimension of uncertainty in fluid production from shale reservoirs. Anomalous production behavior caused by fluid behavior is commonly observed with shale well productions, such as extended understaturated production stage (suppressed bubble point),[3,4] leaner-than-expected fluid produced in the wellstreams,[5] low recovery and its association with the degree of undersaturation.[5]

1.1.2 Experimental approaches

Past experimental approaches largely use isothermal sorption to evaluate various fluids in mesoporous media.[6-10] Adsorption behavior of argon, nitrogen, light hydrocarbons (methane to *n*-butane) and some intermediates (*n*-pentane and *n*-hexane) in nanoporous media have been experimentally studied.[11-13] It is generally observed that the adsorption pore filling happens at a very low relative pressure (p/p^o) in pores of less than 2 nm because the proximity of pore surfaces results in stronger interaction between the adsorbate and pore surface; pore filling later happens at an increased p/p^o in pores with diameter larger than 2 nm, and both monolayer-multilayer adsorption and capillary condensation may be

observed; finally, in very large pores (diameter > 50 nm), pore filling occurs near or at $p/p^o = 1$, i.e., phase behavior is almost the same as bulk.[14] Based on these observations, IUPAC adopts the notations:[14,15] (1) micropore: pore diameter < 2 nm; (2) mesopores: 2 nm < pore diameter < 50 nm; (3) macropore: pore diameter > 50 nm. Also, the criticality of the confined fluid deviates from bulk values, and the confined critical temperature decreases related to that of bulk.[7] Furthermore, hysteresis is commonly observed in sorption isotherms, for which the loop undergoes a reduction in size with increasing temperature.[6,16] It is also reported that chemical properties, texture and degree of disorder of pore surface affect the adsorption/desorption behavior.[8,9]

Other experimental approaches include neutron diffraction,[17] vibrating tube densimetry[18] and visual observation.[19-21] As observed in these experiments, fluid shows bulk phase behavior in pores larger than 50 nm, while in nanopores smaller than 50 nm, the phase behavior is distinctly altered by the confinement effect.

Table 1. Previous experimental methods for studying confined hydrocarbons.

Methods	Pros	Cons
Isothermal Adsorption	Good for light hydrocarbons	Not good for intermediates and heavy hydrocarbons
Visual Observation (Lab-on-a-Chip)	Allows the visualization of phase transitions	Limited to low viscosity fluid
Vibrating Tube Densimetry	Directly measures fluid density, HPHT suitable	Limited to low viscosity fluid
X-Ray/Neutron Diffraction	Gives the details of pore filling process	Indirect density information, instrument limitation

Table 1 summarizes the pros and cons of the previous experimental methods. Isothermal adsorptions is not suitable for measuring phase behavior of heavy hydrocarbons, because the vapor pressures of heavy hydrocarbons are very low. Visual methods and vibrating tube densimetry are limited to low viscosity fluid, and, therefore, the intermediate and heavy hydrocarbons are difficult to exam. X-Ray or neutron diffractions are very good methods to probe the pore filling process, however, the fluid density is indirectly obtained and the instrument is very expensive and not commonly accessible.

Therefore, the experimental studying of confined hydrocarbons, especially for the intermediate and heavy hydrocarbons, is very challenging using the previously developed experimental methods. A reliable and efficient method to access the phase behavior of hydrocarbon phase behavior in nanopores is highly desired.

1.1.3 Thermodynamic modeling

Fundamentally, there are two kinds of molecular interactions for the fluid in nanopores: one is the fluid-fluid interaction and the other is the fluid-pore wall interaction. The fluid-fluid interactions has been well-studied and described in the bulk-state thermodynamics. It is the extra interaction between fluid and pore wall that leads to the deviations of confined phase behavior from the bulk behavior. Therefore, to study the phase behavior of confined fluid, the description of fluid-pore wall interaction is necessary. Generally, there are two types of approaches to describe the fluid-pore wall interaction: one is to indirectly consider it as a capillary effect, which is quantified as a pressure difference

between the liquid and vapor phase, i.e. capillary pressure; the other method is to directly describe the fluid-pore wall interaction in form of a molecule-level potential function.

The capillary pressure method utilizes the Young-Laplace equation, Eq. (1.1). Δp is the pressure difference between liquid and vapor phase; γ is the surface tension; R_1 and R_2 are the principal radii of interface curvature. The interfacial tension γ between fluid in the nanopore and fluid in the bulk are assumed equal. Additionally, the equation does not include the interaction force between the fluid molecules and the pore wall, and it therefore ignores the surface-adsorbed fluid. The formulation based on capillary pressure yields the classical Kelvin equation. However, it needs to be noted that, in practice the Kelvin equation was found to severely underestimate pore size in determining pore size in nano-scale systems.[22-24] Recently, several studies have examined the nano-scale fluid phase behavior by implementing the capillary pressure in flash calculations using the Peng-Robinson equation of state (PR EOS).[4,25-28] Elsewhere, Tan and Piri[29,30] reported an equation-of-state modeling by PC-SAFT (perturbed chain-statistical associating fluid theory) coupled with a modified Young-Laplace equation.

$$\Delta p = \gamma \left(\frac{1}{R_1} + \frac{1}{R_2} \right) \tag{1.1}$$

For the approach of directly describing the fluid-pore wall interactions, several methods, such as extended equation of state (EOS), density functional theories (DFT) and molecular simulation, are developed. Recently, Travalloni *et al.* reported a pore-size-dependent equation of state (EOS) by extending the PR-EOS to nano-systems.[31-34] The Peng-Robinson-Confined (PR-C) EOS is formulated by describing the interaction between fluid

molecules and the pore wall as a square-well potential, Eq (1.2). u represents the interaction energy; r is the distance of molecule to the wall; σ is the diameter of fluid molecule; ε_p is the square-well depth and δ_p is the square-well width. The resulting EOS requires two parameters to describe the fluid-pore surface interaction by range and energy, which need to be determined from experiments. The advantage of PR-C EOS is that it embeds the molecular description of the fluid-pore surface interaction while keeping a relatively concise form, and also that the PR-C EOS describes the pore fluid by pore diameter and it naturally reverts to PR EOS at large pores.[32]

$$u(r) = \begin{cases} \infty & r < \dfrac{\sigma}{2} \\ -\varepsilon_p & \dfrac{\sigma}{2} < r < \dfrac{\sigma}{2} + \delta_p \\ 0 & r > \dfrac{\sigma}{2} + \delta_p \end{cases} \tag{1.2}$$

Density functional theory (DFT)[35,36] and molecular simulation[37-40] are sophisticated methods which employs more realistic potentials for molecule-molecule and molecule-pore wall interactions. The Lennard-Jones potential is the most commonly used potential function, Eq. (1.3).[41] Substantial insight into the phase transitions in nanopores have been obtained through DFT and molecular simulations. Li *et al.* [35] developed an engineering DFT technique combined with PR EOS and simulated adsorptions of single components and hydrocarbon mixtures in nano-scale slit pores. Jin and Nasrabadi[40] presented a modified gauge-Gibbs ensemble Monte Carlo (GEMC) molecular simulation to study phase equilibria of single and multi-component hydrocarbons and found that in nanopores the critical temperature is reduced and the density gap between liquid and vapor phase is narrowed. Jin and Firoozabadi[36] comparatively applied the methods of Langmuir

adsorption isotherm, solid-solution model, PR EOS/capillary pressure, DFT, and molecular simulation (GCMC) to model the phase behavior of hydrocarbons in shale, and concluded that in pores with sizes greater than 10 nm, the conventional equation of state may be applicable, while in pores less than 10 nm, the fluids become inhomogeneous and molecular level modeling is necessary. However, compared to EOS modeling, both DFT and molecular simulation are computationally expensive. DFT also suffers from the drawbacks such as difficulty in assigning proper pore-fluid potentials[42] and expensive computational cost for the adsorption integral equation.[43]

$$u(r) = 4\varepsilon\left(\left(\frac{\sigma}{r}\right)^{12} - \left(\frac{\sigma}{r}\right)^{6}\right) \tag{1.3}$$

1.2 Dissertation outline

The object of this research is to develop experimental method to assess the phase behavior of hydrocarbons in nanopores, advance the thermodynamic modeling of petroleum fluids in nanoporous media and develop PVT modeling solutions for shale reservoirs. The outline of this dissertation are as followed:

- Chapter 2 presents the experimental measurements of hydrocarbon phase transitions in nanoporous media by differential scanning calorimetry (DSC). The bubble point temperatures of hydrocarbons (*n*-hexane, *n*-octane and *n*-decane) are measured at different pore sizes. The effect of pore loading, fluid mixing and pore size distribution on phase behavior are also studied.
- Chapter 3 discusses the thermodynamic modelings for the experimental observations using equation of state (EOS). The capillary pressure coupled with

Peng-Robinson EOS method is found failed in modeling the experiments. The pore-size-dependent PR-C EOS models the experimental results and predicts the criticalities. The confinement parameters of hydrocarbons (methane to *n*-tetradecane) for PR-C EOS are accomplished and summarized as a data base.

- Chapter 4 presents the multi-scale phase behavior simulation for the shale fluids. Using the pore-size-dependent equation of state, the phase equilibrium among different sizes of nanopores and bulk geometries is calculated and found quite different from the bulk-state phase behavior. The simulation delivers a realistic fluid PVT picture for the petroleum fluids under macro- to nano-scale pore size distribution.
- Chapter 5 presents application of multi-scale phase behavior simulation for gas injections. The criticalities, bubble point shift and phase heterogeneities caused by methane injection is simulated. Additionally, the nanopore-fluid swelling behavior is studied and the oil extraction effect from nanopore is quantified in comparison to bulk fluid swelling behavior.
- Chapter 6 concludes the study and makes future work recommendations.

2. EXPERIMENTAL MEASUREMENT OF PHASE TRANSITIONS*

2.1 Methods

Silicate nanoporous materials CPG-35 (controlled pore glasses, from Sigma-Aldrich), SLG-15 (silica gel, from Sigma-Aldrich), MSU-H (Michigan State University silica-H, from Sigma-Aldrich), SBA-15 (Santa Barbara amorphous silica-15, from ACS Material), CPG-4 (controlled pore glasses, from SCHOTT), SBA-16 (Santa Barbara amorphous silica-16, from ACS Material), MCM-41 (Mobil Crystalline Material-41, from Sigma-Aldrich) were used. The materials properties are shown in Table 2. These silicates are a free-flowing white powder with a 200 to 400 mesh size. The pores are highly branched, connected, and approximately cylindrical in shape. The mean diameter, pore distribution, surface area, and pore volume are given in Table 2. The silicate materials were first cleaned with boiling 70% nitric acid at 100 ℃ for 10 h. Caution: Proper safety precautions should be taken. The nitric acid was decanted and the porous media were rinsed with copious deionized water until the aqueous residue was neutral, and then the porous media were dried under vacuum for 24 h at 240 ℃. The surface of the porous media was rendered oleophilic by surface-functionalization with hexamethyldisilazane (HMDS). The porous

* Part of this chapter is reprinted with permission from "Use of differential scanning calorimetry to study phase behavior of hydrocarbon mixtures in nano-scale porous media" by S. Luo, J. L. Lutkenhaus, and H. Nasrabadi, 2018. *Journal of Petroleum Science and Engineering*, Volume 163, Pages 731-738, Copyright [2018] by Elsevier B.V., and "Confinement-Induced Supercriticality and Phase Equilibria of Hydrocarbons in Nanopores" by S. Luo, J. L. Lutkenhaus, and H. Nasrabadi, 2016. *Langmuir*, Volume 32, Pages 11506-11513, Copyright [2016] by American Chemical Society, and "Experimental Study of Confinement Effect on Hydrocarbon Phase Behavior in Nano-Scale Porous Media Using Differential Scanning Calorimetry" by S. Luo, J. L. Lutkenhaus, and H. Nasrabadi, 2015. SPE Proceedings, SPE-175095-MS, Copyright [2015] by Society of Petroleum Engineers, and "Effect of confinement on the bubble points of hydrocarbons in nanoporous media" by S. Luo, H. Nasrabadi, and J. L. Lutkenhaus, 2016. *AIChE Journal*, Volume 62, Pages 1772-1780, Copyright [2016] by American Institute of Chemical Engineers.

media were reacted with neat HMDS at 55 ℃ for 20 h. The reagent was decanted, and the porous media were rinsed copiously with dichloromethane and dried under vacuum for 24 h at 100 ℃.[44] When not in use, the porous media were stored in a desiccator for up to three months. It is reported that silylation on silica nanopores resulted in a pore diameter decrease of ca. 0.2 nm.[8,45] The effective pore diameters of materials after surface treatment are obtained accordingly, as shown in Table 2.

Table 2. Properties of nanoporous materials.

Materials	MCM-41	SBA-16	CPG-4	SBA-15	MSU-H	SLG-15	CPG-35
Native Pore Diameter (nm)	2.4	3.5	4.3	6.2	10	15	38.1
Effective Pore Diameter after surface treatment (nm)	2.2	3.3	4.1	6	9.8	14.8	37.9
Surface Area (m^2/g)	1000	700-900	170	600	750	300	64.7
Pore Volume (cm^3/g)	0.98	0.98	0.22	0.68	0.91	1.15	1.17

In preparing test samples for differential scanning calorimetry (DSC), the porous media powder was weighed and transferred to the pan prior to adding the hydrocarbon. The pan was capped with a Tzero® hermetic lid bearing a 75-μm-diameter pinhole, sealed carefully with wax film and vinyl tape, and kept undisturbed for 24-48 h so that the pores were filled with hydrocarbons by capillary wetting. The film and tape were removed prior to DSC measurements.

Thermal analysis was performed using a TA Instruments Q200 differential scanning calorimeter and all measurements were performed under nitrogen atmosphere. The heating rate was selected to be 10 K/min and only the first scan was analyzed. We found that

slower heating rates resulted in significant fluid loss from vaporization and that faster heating rates gave an undesirable thermal lag. The bubble point was taken as the onset of the endothermic peak associated with vaporization, determined as the intersection of the tangent line at the point of greatest slope on the leading edge of the peak with the extrapolated baseline. The bulk octane and decane bubble points T_b were 398.72 ± 0.04 K and 447.4 ± 0.2 K, respectively, and are in good agreement with the literature.[46] These values were taken as the bulk values for reference in this study. The enthalpy of vaporization ΔH_{vap} was calculated from the integrated area of the endothermic peak, and was generally consistent among all results. However our measured ΔH_{vap} was about 10% less than the standard bulk enthalpy of vaporization. This deviation could be due to mass loss through the course of the sample preparation and experiment, since the pan was open to the atmosphere by the pinhole.

Thermogravimetric analysis (TGA) was performed using a Q500-TGA from TA Instruments and measurements were performed under nitrogen atmosphere. The same sample system are selected as that in DSC: the Tzero® hermetic pan and lid with pinhole were used and the heating rate was selected to be 10 K/min. According to the TGA analysis, the vaporization mass loss before reaching the bubble point was minimal, which was 3~5% of the total hydrocarbon mass loss.

2.2 Single component in single-sized nanopores

DSC thermograms of octane and decane-loaded in 37.9 nm pore diameter CPGs are presented for various loadings in which 100% represents the case of completely filled pores, Figure 3.[47] Below 100% the CPGs are under-filled, and above 100% the CPGs are over-filled. The loading is based on the known volume of fluid added relative to the pore volume. The thermogram for the bulk fluid (in the absence of CPGs) is presented as the bottom green trace. The heat flow is normalized against the mass of the hydrocarbon only. DSC scans for octane infiltrated into the 37.9 nm pores for various loadings of 135% (1.581 cm^3/g), 101% (1.181 cm^3/g), 90% (1.057 cm^3/g), 77% (0.902 cm^3/g), 49% (0.574 cm^3/g) and 19% (0.225 cm^3/g) are shown in Figure 3a; scans for decane infiltrated into the 37.9 nm pores for various loadings of 143% (1.743 cm^3/g), 96% (1.167 cm^3/g), 80% (0.966 cm^3/g), 59% (0.722 cm^3/g), 39% (0.475 cm^3/g) and 19% (0.232 cm^3/g) are shown in Figure 3b. T_b represents the bubble point of the bulk fluid and $T_{b,c}$ represents the bubble point of the confined fluid.

For octane loadings of 101% and 135%, the bulk-vaporization peak is observed at the bulk bubble point, which is due to excess octane outside the pore, Figure 3a. For $T_{b,c}$ at octane loadings of 90% and below, a single vaporization endotherm distinguished from the bulk peak was observed with an onset of 394-399 K, about 0-5 K below the bulk bubble point (399 K), Figure 3. The bubble point generally decreased slightly as loading decreased. At the lowest loading of 20 %, only a 2 to 5 K shift in bubble point was observed, which implies that confinement is not very strong at this length scale. This trend in loading can

be rationalized by considering that loading probably occurs first by surface wetting,[48] second by filling the remaining volume in the pore,[49] and third by existing as excess at high loadings. Accordingly, the thermal properties for low loadings should reflect fluid within the CPG pores, and high loadings should reflect both excess fluid and that within the pores. Here, the two peaks observed in Figure 3a are likely a result of excess octane and that within the CPGs. Decane behaved quite similarly, Figure 3b.

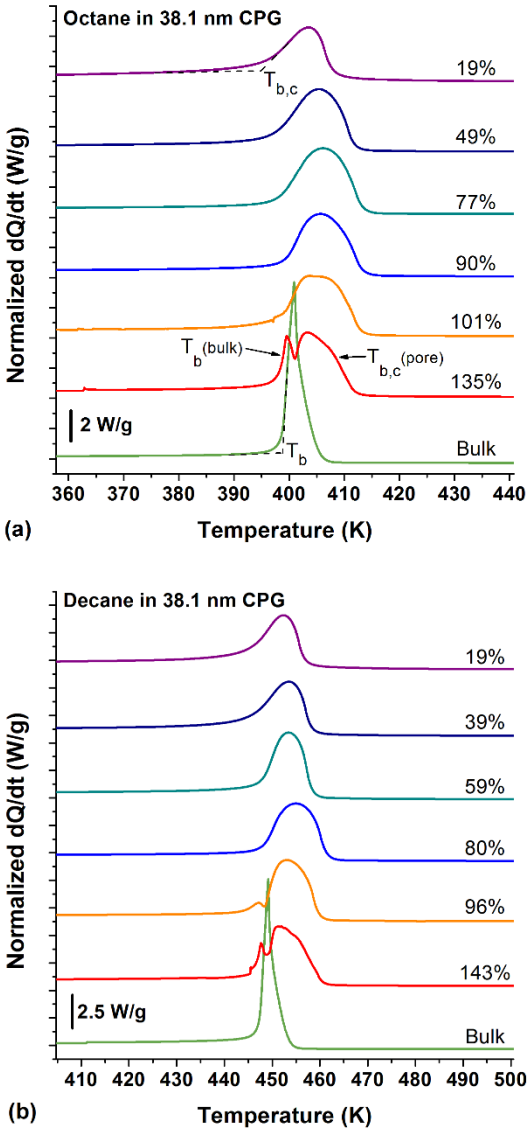

Figure 3. DSC thermograms for (a) octane and (b) decane infiltrated into 37.9 nm pore diameter CPGs. The heat flow is normalized against the mass of the hydrocarbon alone. Scan rate is 10 K/min.[47]

We next turn to the case of octane and decane infiltrated into CPGs bearing 4.1 nm diameter pores. Endotherms for octane at loadings of 120% (0.263cm^3/g), 103% (0.226 cm^3/g), 87% (0.192 cm^3/g), 73% (0.161 cm^3/g), 65% (0.143 cm^3/g) and 56% (0.124 cm^3/g)

and for decane at loadings of 138% (0.304 cm^3/g), 114% (0.250 cm^3/g), 86% (0.189 cm^3/g), 79% (0.174 cm^3/g), 69% (0.145 cm^3/g) and 56% (0.124 cm^3/g) are shown in Figure 4. Significant deviations in the bubble point behavior from the bulk fluid were observed. Specifically, all confined fluids exhibited two endothermic peaks (one above and one below the bulk vaporization peak). T_p represents the maximum peak temperature for the bulk case and $T_{p,c}$ represents the maximum peak temperature for the second endothermic peak of the confined fluid.

We first discuss the lower temperature peak, which follows a trend similar (but more pronounced) to that of the infiltrated 37.9 nm CPGs. From 87% to 56% octane loading, the onset of the low temperature peak ($T_{b,c}$) shifted downward from 388 K to 383 K, which is 11-16 K low temperature peak decreased relative to the bulk bubble point (399 K). For decane, a similar shift in the low temperature peak was observed; from 86% to 56% loading, $T_{b,c}$ shifted from 434 K to 423 K, which is 13-24 K lower than the bulk bubble point (447 K). The variation of octane and decane bubble points with loading indicates good wetting characteristics of the treated CPG surface, which is consistent with the results of hydrocarbons in the 37.9 nm CPG. On the other hand, the high temperature endothermic peak shifted to higher temperatures relative to the bulk vaporization peak. Since this second peak was broad and its onset overlapped at times with the first peak, the maximum peak temperature $T_{p,c}$ was applied to describe the bubble point shift relative to the maximum peak temperature for the bulk case T_p. Variation in the peak temperature was relatively small among the different loadings. For octane, the peak temperature $T_{p,c}$

was 415 K to 420 K for loadings from 56% (under-filled) to 120% (over-filled), which is 14-19 K greater than bulk T_p (401 K). Similar behavior was observed for decane: $T_{p,c}$varied from 464 K at 56% loading to 467 K at 138% loading, which is 15-18 K higher than the bulk T_p (449 K).

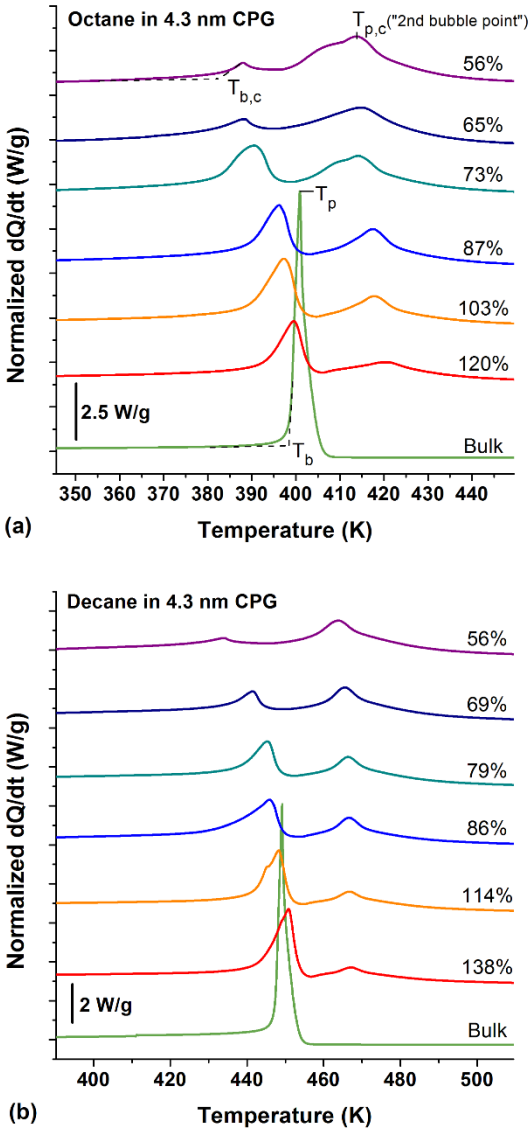

Figure 4. DSC thermograms for (a) octane and (b) decane infiltrated into 4.1 nm pore diameter CPGs for various loadings. The heat flow is normalized against the mass of the hydrocarbon alone. Scan rate is 10 K/min.[47]

We turned to thermogravimetric analysis to investigate the fluid vaporization (weight loss) to complement results from DSC, Figure 5. TGA of octane in 4.1 and 37.9 nm pore diameter CPGs was performed using conditions identical to that of DSC, and the weight

fraction is normalized against hydrocarbon weight (octane infiltrated in CPGs, red curve) and CPG weight (pure CPG, green curve). As shown in Figure 5, any weight loss is associated with the vaporization of octane, since the CPGs are inert over this temperature range. For the octane-loaded 37.9 nm CPG, one vaporization event observed, with an onset at 372 K; the weight percentage retained decreased from 97.8 wt% to 0.9 wt% over the course of vaporization, suggestive of complete vaporization of the hydrocarbon. For octane loaded 4.1 nm CPGs, two vaporization events occurred with onsets at 356.7 (98.8 wt% retained) and 400.8 K (56.1 wt%) and complete vaporization (0.6 wt% at 498.3 K). This result is consistent with DSC results for octane-loaded 4.1 nm CPGs, in low temperature endothermic peak almost disappears at 56% loading (purple curve, Figure 2a). The DSC and TGA results for nanoconfined octane are compared for similar loadings. The weight loss rate and heat flow rate both exhibit the same curve shape for octane in both 37.9 nm and 4.1 nm pore diameter CPGs. The peak onsets and maximums indicate that the bubble points measured from both techniques are consistent.[47]

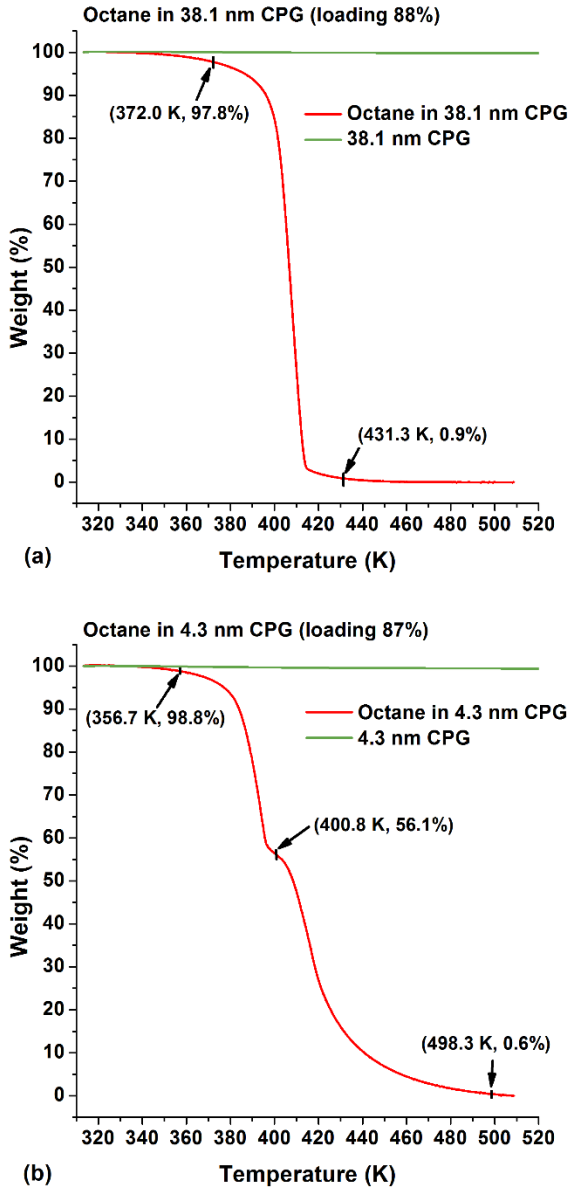

Figure 5. Thermogravimetric profiles for octane infiltrated into (a) 37.9 nm (loading 88%) and (b) 4.1 nm (loading 87%) pore diameter CPGs. The scan rate is 10 K/min and the weight % is normalized against hydrocarbon weight (octane infiltrated in CPGs, red curve) and CPG weight (pure CPG, green curve).[47]

Next we investigated the phase transition in the nanopores of a various pore diameters.[50] Nanoporous media of varying pore diameter (CPG-35: 37.9 nm, SLG-15: 14.8 nm, MSU-H: 9.8 nm, SBA-15: 6.0 nm, CPG-4: 4.1 nm, SBA-16: 3.3 nm, MCM-41: 2.2 nm) were filled with hydrocarbons (*n*-hexane, *n*-octane or *n*-decane) by capillary wetting.[47] Figure 6 shows the DSC traces for bulk hexane, octane and decane as green curves (without porous media). For confined fluid/media systems at various pore sizes, the media were over-filled with hydrocarbons and a clear separation between the confined and bulk fluid is observed.[47] The liquid-vapor phase transition under confinement is obtained as the onset of the confined vaporization peak. The confined fluid generally vaporized at a temperature higher than the bulk fluid, except the case at 2.2 nm. At 2.2 nm, the fluid show different phase behavior, observed as one major peak and several minor peaks at higher temperatures. For the example of hexane (Figure 7a), from 37.9 to 4.1 nm, the bubble point of the confined fluid increased from 342.6 to 357.0 K. From 4.1 to 3.3 nm, the bubble point the bubble point then decreased, from 357.0 to 348.4 K. It's worth noting that at 4.1–9.8 nm the bubble shift is 15.1–12.1 K from bulk; whereas at 14.8–37.9 nm, the bubble point shift is 2.8–0.7 K (Figure 7b, red triangles). It can be inferred that below 10 nm, the confinement effect is much greater than that over 15 nm pore diameter. Octane and decane behaved similarly (Figure 6b and 6c). In 37.9 nm pores, octane showed a bubble point of 398.8 K; as the pore size decreased to 4.1 nm, the bubble point increased to 416.5 K (Figure 7b, red triangles); further decreasing the pore size resulted in a decreased phase transition point down to 405.8 K (3.3 nm). For decane, the bubble point is 447.8 K at 37.9 nm; decreasing pore diameter resulted in an increased bubble point, which peaked at 4.1

nm (465.0 K) (Figure 7c, red triangles); from 4.1 to 3.3 nm, the phase transition point decreased to 455.5 K.

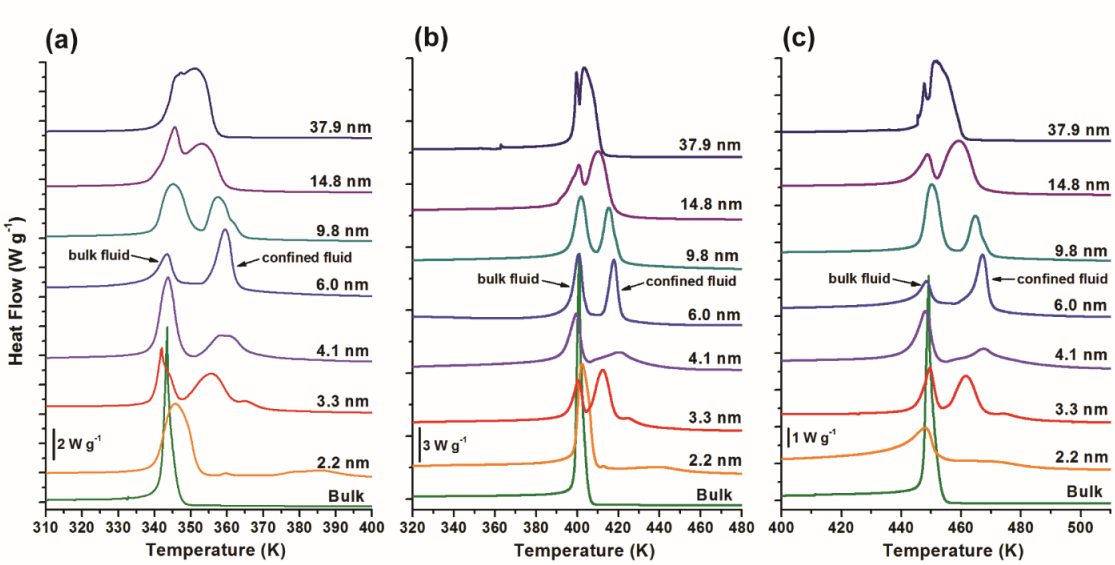

Figure 6. DSC thermograms of nanoconfined fluids (a) hexane, (b) octane and (c) decane at atmospheric pressure (101.325 kPa). Clear separation between bulk and confined fluid vaporization peaks was observed. The nanopores were infiltrated with hydrocarbons, and excess hydrocarbons existed as bulk fluid outside the pores. The pore loading percentages are included in supplementary information. The numbers on the right indicate the diameter of the nanoporous media in which the hydrocarbons were confined. Bulk refers to the scan of bulk fluid (green curves). The thermograms of octane and decane in 4.1 and 37.9 nm pores are from our previous work.[47,50]

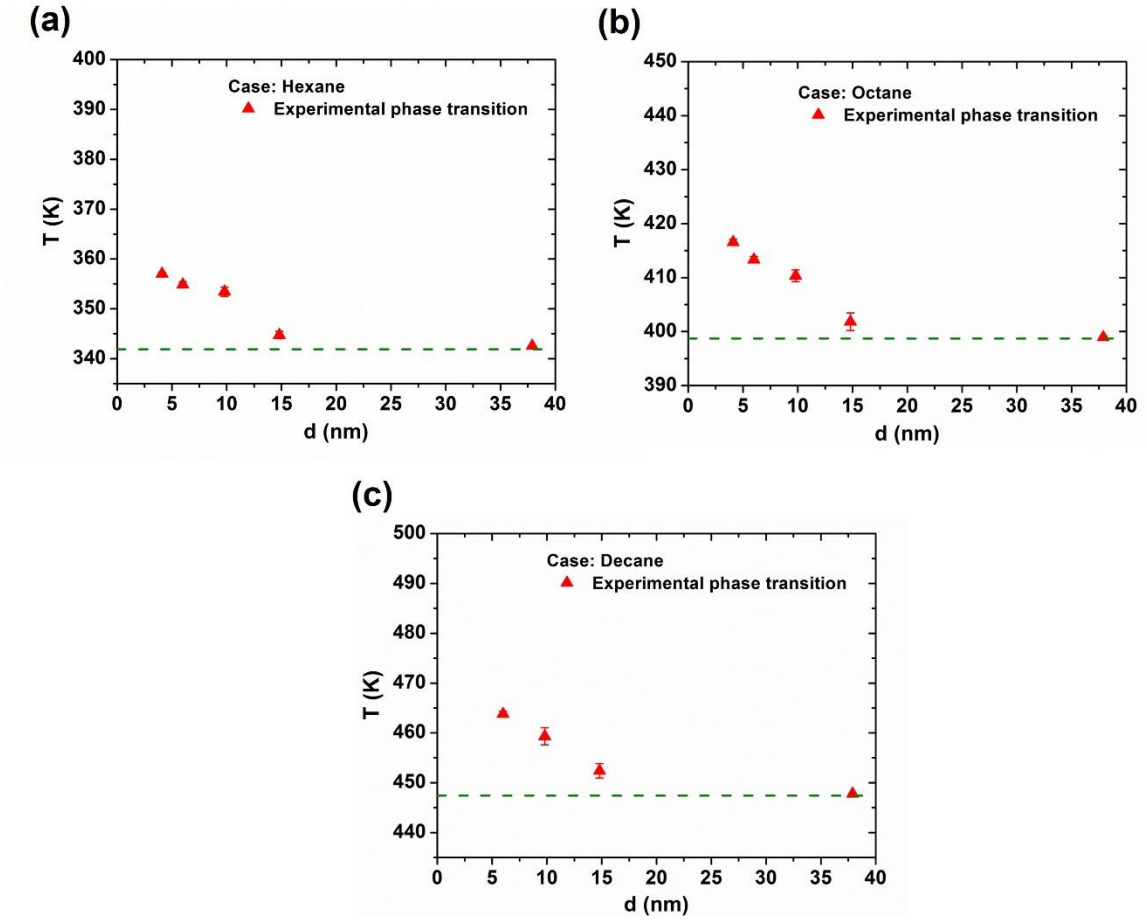

Figure 7. Results of the experimental bubble points and modeled T-d phase diagrams at atmospheric pressure (101.325 kPa) bulk vapor for (a) hexane, (b) octane and (c) decane. The experimental bubble points increased from 37.9 nm to 4.1 nm (red triangles with error bars). Error bars, s.e.m, are obtained from experiments repeated three times.[50]

The multiple enthalpic peaks in the thermograms for pore diameters less than 4 nm is expected mostly because of the layering effect and heterogeneous pore distribution. For example, at 2.2 nm, one major peak is assigned as the bulk fluid peak, and several broad and small peaks of confined fluids are observed at higher temperatures. The high temperature peaks may be attributed to the evaporation of the first few layers of adsorbed fluid in the pore. Li *et al.* reported phase transitions associated with layers of fluid in

narrow slit pores: after evaporation of the main fluid in the capillary, residual layers of fluid are removed consecutively from the pore at lower pressures.[51] Similar layering transitions have also been observed by Wongkoblap *et al.* in the study of argon adsorption in single wall nanotubes.[52] An alternative explanation is that the high temperature peak is associated to the molecules adsorbed in smaller micropores due to a heterogeneous pore size distribution. Hydrocarbon desorption temperature in micropores (dia. <2 nm) are reported to be much higher than in mesopores (dia. 2-50 nm). For example, *n*-nonane desorbed in 3.5 nm pore (SBA-15) at 325 K[53] while in 1 nm pore (zeolite) at 407 K[54] and in 0.5 nm pore (zeolite) at 493 K.[54] The complex desorption at high temperature in MCM-41 of our study could be due to the fluid in micropores of the heterogeneous media.

2.3 Mixtures in single-sized nanopores

In the following work, we extend the study to the bubble point of octane-decane binary mixtures.[55] Initially, the bulk fluid samples were subjected to DSC, as shown in Figure 8. Mixtures of various compositions (mol:mol) were studied. It was observed that the main peak was followed by a second shoulder on the right (e.g. 55%:45% mixture, in green), which is different from the results of the single components. We envision that the feature resulted from the compositional change occurring throughout the vaporization process: the heavy component was left behind from the initial vaporization, and the second shoulder was that residue mainly composed of decane. The shoulder matches well with the endotherm of bulk decane. The explanation is also supported by the trend that from high to low octane composition (i.e. 92% octane to 8% octane), the intensity of residue

shoulder gradually increases and finally merges with the main peak. The bubble point is taken as the onset of the main DSC peak, and the PR-EOS calculated bubble point temperatures are in agreement with the experimental results (Table 3).

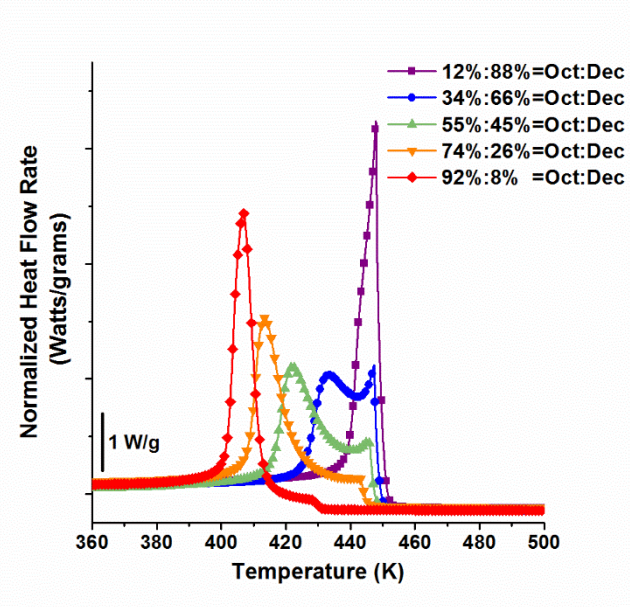

Figure 8. DSC thermograms for the bulk octane:decane binary mixtures (mol:mol).[55]

Table 3. DSC-measured and PR EOS-modeled bubble point temperatures of bulk fluids.[55]

Composition (octane:decane, mol:mol)	12%:88%	34%:66%	55%:45%	74%:26%	92%:8%
T_b (DSC) / K	439.6±0.2	425.5±0.06	415.7±0.09	407.7±0.4	401.7±0.1
T_b (Modeling) / K	438.3	424.5	414.6	407.2	401.3

The bubble points of various octane-decane compositions in 37.9 or 4.1 nm CPGs were investigated. Here, we compared the results from 90% loading (taken as the saturated case) and 19% and 58% loading (taken as the under-filled case) for pore diameters of 37.9 nm and 4.1 nm, respectively. At 37.9 nm, the bubble points of fluids in the pore are very close to that of the bulk throughout all compositions at 90% loading (Figure 9a), indicating that

the confinement effect is minor in 37.9 nm saturated pores. However, for the severely under-filled case of 19% loading, the bubble shifted downward by 1-7 K, which implies that the confinement effect emerges at low loadings.

The bubble points of hydrocarbon mixtures in 4.1 nm pores reveal interesting features (Figure 9b). Here, only the first peak (lower bubble point) is specifically discussed as the composition corresponding to the second peak is largely uncertain because of the prior evaporation event. At saturated loading (90%), the octane-decane binary mixture generally showed a bubble point ca. 20 K lower than the bulk bubble point. At the low loading of 58%, the bubble point curve was relatively flat; regardless of composition, the bubble points were close to that of single component octane. The observations can be rationalized by considering the fluid compositional heterogeneity between the surface-adsorbed state and confined bulk state. At the under-filled loading of 58%, the lighter component (octane) mainly populates the confined bulk state, while the heavier component (decane) shows greater affinity to the pore surface and mainly exists as a surface-adsorbed fluid. Consequently, the lower bubble points of the binary mixtures, corresponding to the confined bulk state fluid, are close to the single lighter component (octane) case. Similar compositional distribution has been observed by Ma and Jamili.[56] They reported that the wall favors the heavier component over the lighter component for an *n*-butane/methane mixture in a 20 nm slit pore.

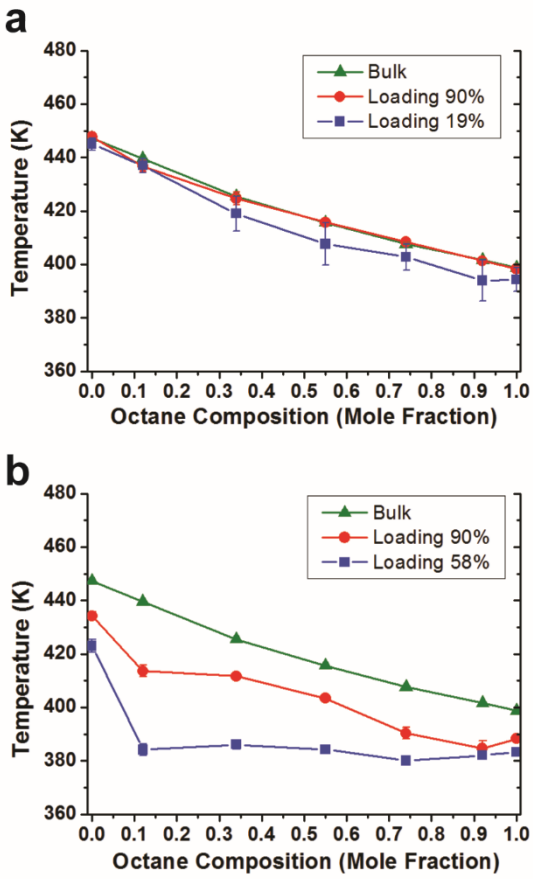

Figure 9. (a) Bubble point temperatures of octane-decane binary mixtures at loadings of 90% and 19% in 37.9 nm CPGs at various compositions. (b) Lower bubble point temperatures for octane-decane binary mixtures at loadings of 90% and 58% in 4.1 nm CPGs at various compositions.[55]

2.4 Single component in nanopores with pore size distribution

Herein, we present an experimental study of hydrocarbon phase behavior in synthetic media of broad pore size distribution representing shale rock. Two types of synthetic media representing the pore size distribution of natural shale rocks (Eagle Ford shale and Bakken shale) are studied. *n*-Hexane, *n*-octane and *n*-decane are infiltrated into nanoporous media, and DSC is used to measure the phase transition temperature of the confined hydrocarbons. We choose two representative pore size distributions for shale

rock: one for Eagle Ford shale[57] and the other for Bakken shale.[4] Eagle Ford shale has a major pore size of ca. 16 nm, and Bakken shale has a major pore size of ca. 40 nm. Experimental synthetic porous materials of specific pore diameters were physically mixed to mimic the shale pore size distribution. Figure 10 shows the pore size distributions of the two shale samples and the representative mixture samples used in this work.

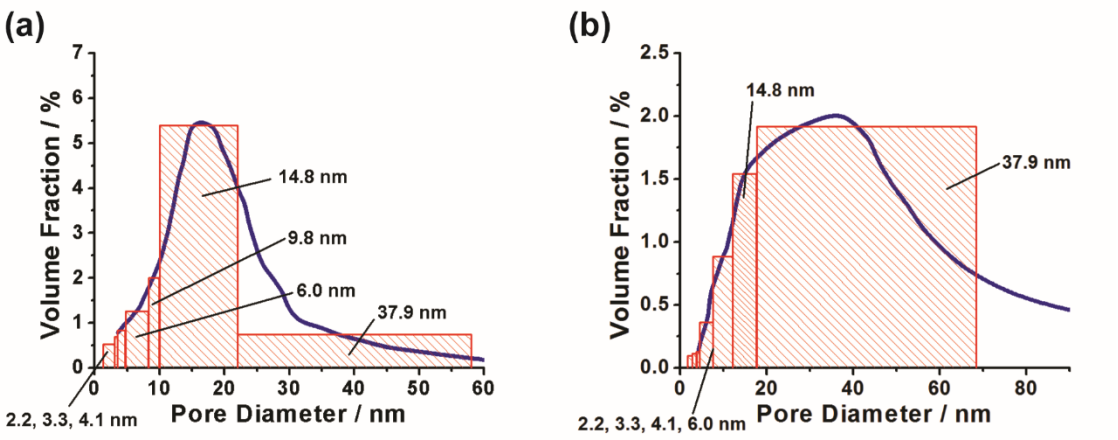

Figure 10. Pore size distribution are from two shale cores: (a) Eagle Ford shale[57] and (b) Bakken shale.[4] The laboratory pore size distribution of shale rocks are shown as blue lines. The shaded columns are the representative discretized pore volumes of synthetic nanoporous media with a specific pore diameter used in this work. The details are discussed in experimental section.

The porous materials in Table 2 were physically mixed to mimic the pore size distribution of shale rock (Figure 10). A specific portion of each type of material was used to represent the corresponding pore size portion of shale rock. An optimization method was used to determine the mass fractions of porous media. We note the pore diameters of *n* types of experimental porous media from smallest to the greatest as $d_1, d_2, \ldots, d_n$ and their pore

volumes per mass (cm^3/g) as $PV_1, PV_2, \dots, PV_n$. Their mass fractions in the synthetic mixture are $m_1, m_2, \dots, m_n$ and the pore volume fractions are $V_1, V_2, \dots, V_n$. The mass fraction relation and pore volumes can be written as:

$$m_1 + m_2 + \cdots + m_n = 1 \tag{2.1}$$

$$V_i = \frac{m_i \cdot PV_i}{\sum_{i=1}^{n} m_i \cdot PV_i} \tag{2.2}$$

The discrete pore volumes $V_1, V_2, \dots, V_n$ represent the pore size distribution. V_i is the area of shaded columns of the medium i in Figure 8. The height of the column is directly read from the PSD curve by the specific material's pore diameter, as h_i. The width w_i of the column is the range of PSD represented by the pore diameter in the center.

$$w_i \cdot h_i = V_i \tag{2.3}$$

Herein, we optimize the choices of column widths $w_1, w_2, \dots, w_n$ by minimizing the gaps between the columns, where the target function *g(w)* can be written as:

$$g(w) = \sum_{i=1}^{n-1} \left(\frac{w_i + w_{i+1}}{2} - (d_{i+1} - d_i) \right)^2 \tag{2.4}$$

The target function is minimized under the constraints of Eq. (2.1) and the relations of Eqs. (2.2) and (2.3) using the Matlab optimization toolbox. The results of mixing mass fractions for each case are listed in Table 4.

Table 4. Nanoporous media mixture representing the shale pore size distribution.

Porous Materials		MCM-41	SBA-16	CPG-4	SBA-15	MSU-H	SLG-15	CPG-35
Mass Fraction	Eagle Ford sample	0.4%	1.3%	1.2%	8.9%	1.6%	64.3%	22.3%
	Bakken sample	0.1%	0.2%	0.2%	2.1%	2.7%	11.6%	83.1%

DSC thermograms of octane confined in the synthetic Eagle Ford sample at different loadings are presented in Figure 10a. The loading is defined as the volume of added fluid to the cumulative volume of the pores (Table 2 and 4). A loading of 100% represents that all pores are completely filled, above 100% the pores are over-filled, and below 100% the pores are under-filled. The uncertainty of loading percentage is expected to be 3-10% due to uncertainties in fluid[58] and pore volume[59,60] calculations. At a loading of 107%, two major peaks were observed along with minor features below and above these peak temperatures. At a loading of 93%, four peaks are clearly observed. As found in our previous observations, the bulk fluid bubble point temperature is lower than that of the confined fluid.[50] The peak at the lowest temperature relates to the vaporization of bulk fluid, which exists outside the pores. It needs to be clarified that bulk fluid may be observed at a loading slightly less than 100% because fluid may fill the porous media heterogeneously and some minor amount of fluid may stay outside the nanopores. Consistent with our previous observations,[47] the bulk peak disappeared upon lowering the loading to 83%. At 83%, the onsets of the two major peaks were 396.7 K and 401.8 K. Further decrease of the pore loading to 68% resulted in a smaller peak at 396.7 K. At a pore loading of 46%, there was only one major peak at 401.8 K and a minor one at the higher temperature. By comparing with the scans of octane confined in porous media of a single pore size,[50] the bubble points were associated with vaporization from the corresponding pore sizes: 398.9 K for 37.9 nm, 401.8 K for 14.8 nm and 410.3-416.6 K for 9.8-4.1 nm. Thus, for the two major peaks at 83%, the one with a lower temperature is from fluid in the 37.9 nm pore, and the higher one is from the 14.8 nm pore. Additionally,

the loading tests indicate that when the pores are under-filled, the fluid will preferably fill the pores of smaller sizes. *n*-Hexane and *n*-decane showed similar discrete vaporization behavior among different pore sizes for the synthetic Eagle Ford PSD (Figure 9b and 9c), where the vaporization of bulk, confined fluid in 37.9 nm, 14.8 nm and smaller pores could be found (peaks from low to high temperature, respectively).

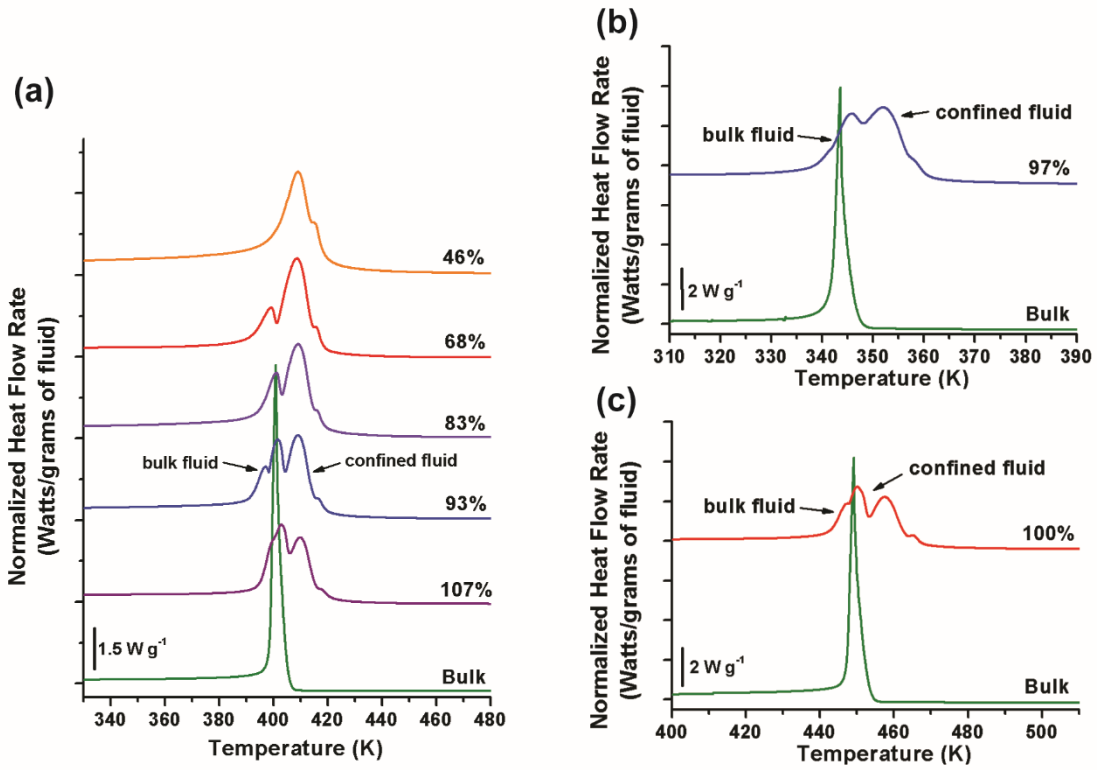

Figure 11. DSC thermograms for (a) octane (b) hexane (c) decane infiltrated in the sample with the synthetic Eagle Ford PSD at atmosphere pressure (101.325 kPa). The percentages on the right are the pore loadings (Loading percentage = $V_{fluid}/V_{total\ pore\ volume} \times 100\%$). Bulk is the scan of bulk fluid (green curves).

DSC thermograms of octane confined in the sample with the synthetic Bakken PSD at different loadings are presented in Figure 12a. At a loading of 108%, two overlapping major peaks were observed. At a loading of 89%, the left peak associated with bulk fluid

vaporization nearly disappeared. The onset of the main peak was measured as 398.6 K, in agreement with the bubble point of octane in 37.9 nm pores (398.9 K).[47] For loadings of 89% to 48%, the main vaporization peak at 398.9 K remains, and several minor peaks at higher temperatures were found. The minor peaks are rationalized to be associated with the vaporization of fluid in small pores (14.8 nm and below). Hexane and decane showed similar vaporization behavior for the synthetic Bakken PSD, where a clear separation of bulk fluid and a major confined peak from 37.9 nm can be recognized (Figures 12b and 12c).

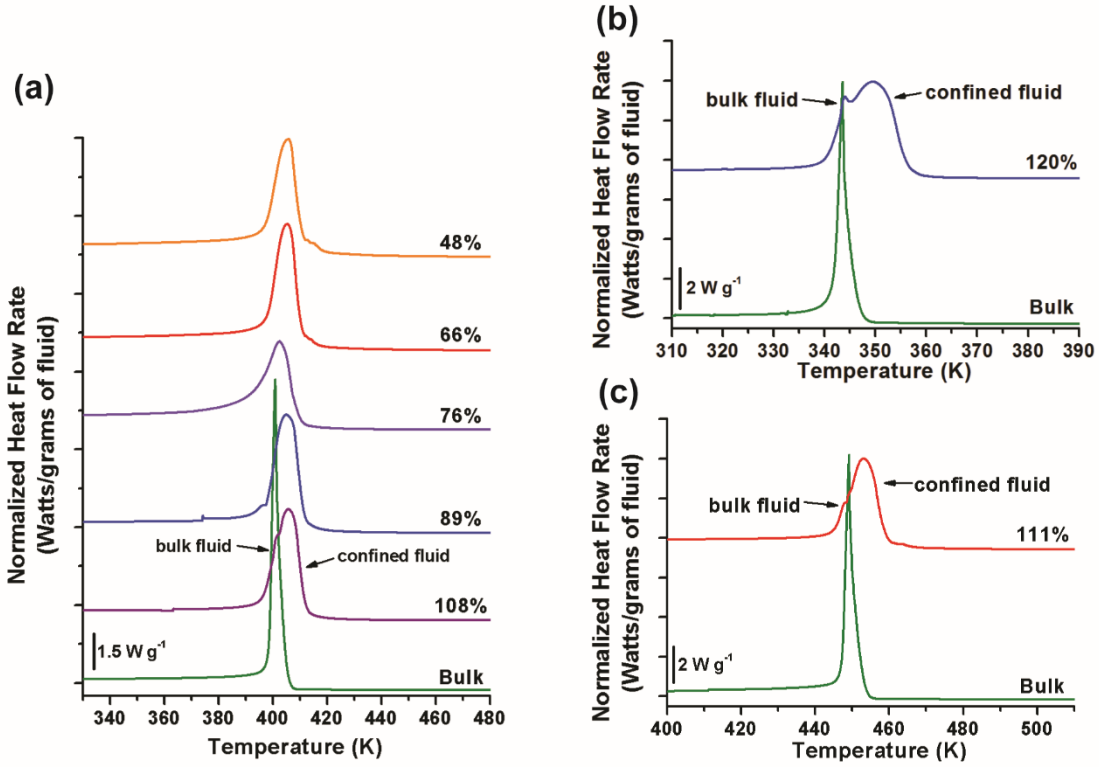

Figure 12. DSC thermograms for (a) octane (b) hexane (c) decane infiltrated in synthetic Bakken PSD at atmosphere pressure (101.325 kPa). The percentages on the right are the pore loadings (Loading percentage = $V_{fluid}/V_{total\ pore\ volume} \times 100\%$). Bulk is the scan of bulk fluid (green curves)

From the DSC analysis of hydrocarbons in the heterogeneous nanoporous media, it is concluded that the phase behavior of hydrocarbons in nanoporous media of a varying PSD varies with fluid saturation or loading. It is generally observed that from high loadings (>100%) to low loadings (<100%), the bulk fluid disappears first, then the large pores are unfilled, and at last the small pores are left empty. These observations indicate that, in the presence of different pore sizes, fluid infiltrates into the smaller pores before the larger pores, both prior to existing in bulk space. It can be explained that the nanopore walls result in stronger interactions between the fluid and pore surface.[61] On the other hand, under a given pore volume, smaller nanopores have the larger surface area, and fluid would preferably fill the smaller pores to lower the surface energy. Russo *et al.* experimentally studied the adsorption enthalpies of organic compounds (*e.g.*, toluene, *n*-pentane, neopentane) in different silica nanopore sizes and found that the isosteric enthalpies with capillaries are higher in narrower mesopores, indicating a stronger interaction or lower energy in narrower nanopores.[9]

3. MODELING PHASE TRANSITIONS IN NANOPORES*

3.1 Peng-Robinson equation of state/capillary pressure

3.1.1 Background

A flash calculation based on Peng-Robinson equation of state[62] including capillary pressure effect is applied to model the bubble point temperature of the nanoconfined hydrocarbons.[55] In conventional reservoirs, the phase behavior of petroleum fluid is well described with equation of state because the confinement effect is insignificant. In unconventional shale reservoirs, the phase behavior is greatly altered from the bulk under the confinement from the pore size at nano-scale. It is established that the effect of capillary pressure due to the curvature at the interface greatly affects the phase behavior.[63] Several studies have accommodated the capillary pressure in modeling the liquid-vapor equilibrium.[4,20,64-66] Herein, to model the experimental measured bubble point temperature of nanoconfined hydrocarbons, we performed a simulation with PR EOS and capillary pressure under isobaric condition.

* Part of this chapter is reprinted with permission from "Use of differential scanning calorimetry to study phase behavior of hydrocarbon mixtures in nano-scale porous media" by S. Luo, J. L. Lutkenhaus, and H. Nasrabadi, 2018. *Journal of Petroleum Science and Engineering*, Volume 163, Pages 731-738, Copyright [2018] by Elsevier B.V., and "Confinement-Induced Supercriticality and Phase Equilibria of Hydrocarbons in Nanopores" by S. Luo, J. L. Lutkenhaus, and H. Nasrabadi, 2016. *Langmuir*, Volume 32, Pages 11506-11513, Copyright [2016] by American Chemical Society, and "Experimental Study of Confinement Effect on Hydrocarbon Phase Behavior in Nano-Scale Porous Media Using Differential Scanning Calorimetry" by S. Luo, J. L. Lutkenhaus, and H. Nasrabadi, 2015. SPE Proceedings, SPE-175095-MS, Copyright [2015] by Society of Petroleum Engineers.

Phase equilibrium indicates that the fugacities of component i in the vapor phase and in the liquid phase should be equal and can be calculated by PR EOS:

$$f_i^V(T, p^V, \underline{y}) = f_i^L(T, p^L, \underline{x}) \tag{3.1}$$

A pressure discontinuity exists between the vapor and liquid phase because of capillarity. The Young-Laplace equation[67] is used to relate the pressure difference between the two phases as capillary pressure (p^C). The capillary pressure is determined by the interfacial tension (σ), pore diameter (d) and contact angle (θ):

$$p^C = p^V - p^L = \frac{4\sigma \cos\theta}{d} \tag{3.2}$$

The interfacial tension (σ) is described with the relation reported by Danesh *et al.*:[68]

$$\sigma^{1/E} = \sum_{i=1}^{n_c} P_i(x_i\rho^L - y_i\rho^V) \tag{3.3}$$

$$E = 3.583 + 0.16(\rho^L - \rho^V) \tag{3.4}$$

It is reported that the contact angle of hexane on HMDS modified silica is 86°.[69] The contact angle is a function of temperature and it is estimated that the contact angle decreases with increasing temperature at the rate of ~0.1 K/deg.[70,71] Thus, we assume that for the hydrocarbons in CPGs at the bubble point, contact angle θ=75°.

The initial guess K factors $K_i=y_i/x_i$ are obtained from the Wilson's equation[72] with bulk bubble point T_b.

$$K_i = \frac{p_{c_i}}{p} exp(5.37(1+\omega_i)\left(1 - \frac{T_{c_i}}{T_b}\right)) \tag{3.5}$$

The estimated confined fluid bubble point is obtained by searching a temperature array. The temperature giving the minimal $\left|ln\left(\frac{f_i^V}{f_i^L}\right)\right|$, which is closest to equal fugacity, is used as the initial guess in iteration.

3.1.2 Modeling experimental results

We solve the nonlinear equations, Eqs. (3.1)-(3.4) using the Newton-Raphson algorithm for confined bubble point temperature with the parameters shown in Table 5. Critical properties and acentric factors from Lyons and Plisga,[46] parachors from Danesh,[73] and binary interaction coefficient from CMG®.

Table 5. Parameters for modeling bubble point.[55,74]

Parameters	Octane	Decane
P_C	2486 kPa	2099 kPa
T_C	568.76 K	617.4 K
Ω	0.399	0.4904
P (parachor)	351.5	433.5
$\delta_{i,j}$	0.00069	
P	101.3 kPa	
Θ	75°	

Modeling results, in comparison with the experimentals, are shown in Figure 13. Generally, PR EOS/capillary pressure model calculation gives an increased bubble point temperature relative to the bulk and the deviation is greater at smaller pore diameter. At 37.9 nm, the modeling gives that the bubble point is 439.4 K for octane and 486.3 K for decane, which indicates that temperature increases are 40.7 K and 38.9 K, respectively. However, the experimental results at 37.9 nm show that the deviation from the bulk is less than 1 K. At 4.1 nm, greater bubble point increase is predicted: 495.3 K for octane and

542.9 K for decane. The experimental results show the bubble point shifts differently. The lower bubble points show a 10.6 K decrease to 388.3 K for octane and a 12.6 K decrease to 434.2 K for decane (Table 6). And the upper bubble points (octane: 416.9 K, decane: 467.1 K) don't agree with modeling results either, shown as purple round symbol in Figures 13a and 13b.

Bubble point inconsistency between modeling and experimental results are also found for octane:decane=55%:45% mixture (Figure 13c). At 37.9 nm, the experimentally measured bubble point shift is insignificant while the model predicts an increase of 41.1 K to 456.8 K; at 4.1 nm, the experiment gives a lower bubble point of 403.4 K and upper bubble point peak maximum of 453.2 K, but according to the modeling results, the bubble point is calculated as 515.5 K (Table 6). It is worth noting that experimentally, compared to single component case, the binary mixtures show a greater difference between the lower and upper bubble points at 4.1 nm, which is attributed to the composition change throughout the vaporization process.

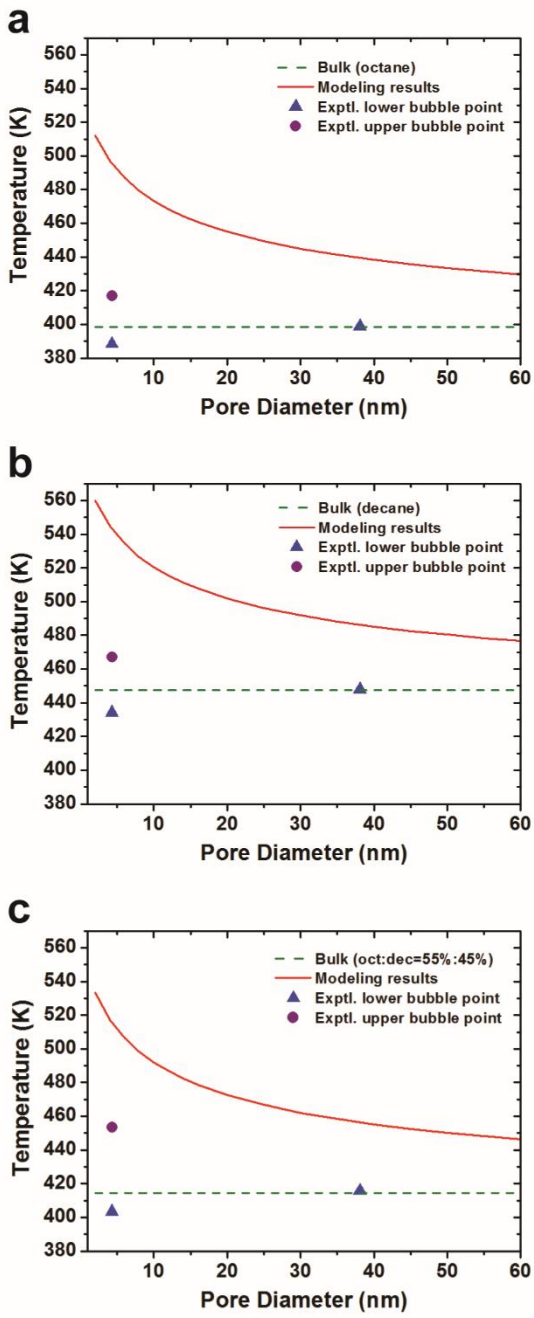

Figure 13. Bubble point temperature plot in relation to pore diameter for single component (a) octane, (b) decane and (c) binary mixture octane:decane=55%:45%.[74]

Table 6. DSC measured and PR EOS/capillary pressure modeled bubble point temperature of confined fluids. At 4.1 nm the experimental upper and lower bubble points are listed. The error percentage is calculated based on the experimental upper bubble point temperature.[55]

Pore Diameter	37.9 nm			4.1 nm		
Fluid	Octane	Decane	Mixture (55%:45%)	Octane	Decane	Mixture (55%:45%)
T_b (DSC) / K	398.8	447.8	415.8	388.3, 416.9	434.2, 467.9	403.3, 453.2
T_b (Modeling) / K	439.4	486.3	456.8	495.3	542.9	515.5
% Error	10.2%	8.6%	9.9%	18.8%	16.0%	13.7%

3.2 Extended Peng-Robinson equation of state

3.2.1 Formulations

A novel pore-size-dependent equation of state (PR-C EOS) has recently been presented by Travalloni *et al*.[31,32,75] The PR-C EOS employs molecular descriptions of fluid-fluid and fluid-pore surface interactions, and it relates the fluid PVT behavior to the fourth dimension of confining pore diameter. The EOS requires two confinement parameters of range and energy to describe the fluid-pore surface interaction. The PR-C EOS considers the interaction between the fluid and pore surface as a square-well potential (Figure 14), where two parameters of square well depth (ε_p) and square well width (δ_p) need to be determined by experiments. The method of directly considering fluid-pore surface interaction is in agreement with the molecular interaction treatments in molecular simulation and density function theory, and the formulations yield the explicit expression of fluid chemical potential in nanopores, Eq. (3.7). The equation of state describes the fluid in pores with a parameter of cylindrical pore diameter (d_p) and it reverts to PR EOS at the large pore diameter.

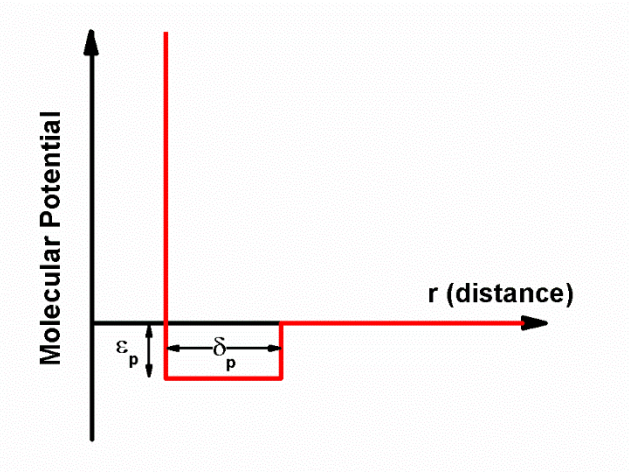

Figure 14. Square-well potential model for the fluid-pore surface interaction. $\boldsymbol{\varepsilon_p}$: square-well depth; $\boldsymbol{\delta_p}$: square-well width. $\boldsymbol{\varepsilon_p}$ and $\boldsymbol{\delta_p}$ need to be determined by experiments.[76]

The PR-C EOS is written as follows:[32]

$$\mathrm{P} = \frac{RT}{v - b_p} - \frac{a_p}{v^2 + 2b_p v - b_p^2} - \sum_{i=1}^{NC}\left(\frac{x_i^2\theta_i b_{p,i}}{v^2}\left(1 - \frac{x_i b_{p,i}}{v}\right)^{\theta_i - 1}\left(1 - F_{pr,i}\right)\left(RT\left(1 - \exp\left(-\frac{N_{av}\varepsilon_{p,i}}{RT}\right)\right) - N_{av}\varepsilon_{p,i}\right)\right) \tag{3.6}$$

$$\mu_i = \mu_{0,i} + RTln\left(\frac{N_{av}x_i\lambda_i^3}{v - b_p}\right) + \frac{RTb_{p,i}}{v - b_p} - \frac{a_p b_{p,i} v}{b_p\left(v^2 + 2b_p v - b_p^2\right)} + \frac{\sqrt{2}}{4}\ln\left(\frac{v + \left(1 + \sqrt{2}\right)b_p}{v + \left(1 - \sqrt{2}\right)b_p}\right)\left(\frac{a_p b_{p,i}}{b_p^2} - \frac{2}{b_p}\sum_{j=1}^{NC}\left(x_j a_{p,ij}\right)\right) - F_{pr,i}N_{av}\varepsilon_{p,i} + \left(1 - (\theta_i + 1)\frac{x_i b_{p,i}}{v}\right)\left(1 - \frac{x_i b_{p,i}}{v}\right)^{\theta_i - 1}\left(1 - F_{pr,i}\right) \cdot \left(RT\left(1 - \exp\left(-\frac{N_{av}\varepsilon_{p,i}}{RT}\right)\right) - N_{av}\varepsilon_{p,i}\right) \tag{3.7}$$

The a_p and b_p are confinement-modified energy and volume parameters for the equations of state. r_p is the cylindrical pore radius. σ_i is the molecular diameter of component i from

Eq. (3.13). σ_{ij} is the average molecular diameter of component *i* and *j*, Eq. (3.14). Binary interaction parameters k_{ij} are included in the mixing rule, Eq. (3.10). a_p is given as:

$$m_i = \begin{cases} 0.37464 + 1.54226\omega_i - 0.26992\omega_i^2, & 0 < \omega_i \leq 0.5 \\ 0.3796 + 1.485\omega_i - 0.1644\omega_i^2 + 0.01667\omega_i^3, & \omega_i > 0.5 \end{cases} \tag{3.8}$$

$$a_i = \frac{0.45724\mathrm{R}^2 T_{C,i}^2}{P_{C,i}} \left(1 + m_i \left(1 - \sqrt{\frac{T}{T_{C,i}}}\right)\right)^2 \tag{3.9}$$

$$a_{p,ij} = (1 - k_{ij})\sqrt{a_i a_j}\left(1 - \frac{2}{5}\frac{\sigma_{ij}}{r_p}\right) \tag{3.10}$$

$$a_p = \sum_{i=1}^{NC}\sum_{j=1}^{NC}(x_i x_j a_{p,ij}) \tag{3.11}$$

b_p is given as:

$$b_i = \frac{0.07780 R T_{C,i}}{P_{C,i}} \tag{3.12}$$

$$\sigma_i = \sqrt[3]{\frac{1.158 b_i}{N_{av}}} \tag{3.13}$$

$$\sigma_{ij} = \frac{\sigma_i + \sigma_j}{2} \tag{3.14}$$

$$b_{p,i} = \frac{N_{av}\sigma_i^3}{1.158 - 0.479\exp\left(0.621\left(0.5 - \frac{r_p}{\sigma_i}\right)\right) + 0.595\exp\left(4.014\left(0.5 - \frac{r_p}{\sigma_i}\right)\right)} \tag{3.15}$$

$$b_p = \sum_{i=1}^{NC} x_i b_{p,i} \tag{3.16}$$

For component *i*, θ_i is the geometric term and $F_{pr,i}$ is the fraction of fluid within the pore surface attractive field under random distribution:

$$\theta_i = \frac{r_p}{\delta_{p,i} + \frac{\sigma_i}{2}} \tag{3.17}$$

$$F_{pr,i} = \frac{\left(r_p - \frac{\sigma_i}{2}\right)^2 - \left(r_p - \frac{\sigma_i}{2} - \delta_{p,i}\right)^2}{\left(r_p - \frac{\sigma_i}{2}\right)^2} \tag{3.18}$$

In addressing the two-dimensional phases adsorption problem, the phase equilibrium is solved by relating the fugacities of the adsorbed phase and bulk phase, using the methodology proposed by Hoory and Prausnitz.[77] The calculation results of adsorption has been compared with Monte Carlo simulations in satisfactory agreement.[78] In application of the extended van der Waals equations, Travalloni *et al.*[31,32] models the multicomponent adsorption in nanoporous media by solving the adsorption equilibrium equations, which is,

$$\mu_{i,a}\left(T, \rho_a, \underline{x_a}, r_p\right) = \mu_{i,b}\left(T, P_b, \underline{x_b}\right), i = 1,2, \dots, NC \tag{3.19}$$

Where *NC* is the number of components, $\mu_{i,a}$ and $\mu_{i,b}$ are the chemical potential for component i of adsorbed and bulk phase, and $\underline{x_a}$ and $\underline{x_b}$ denote all molar fractions of components 1, 2,…, *NC* in adsorbed and bulk phase, P_b is the bulk phase pressure, ρ_a is the adsorbed phase density and r_p is the pore radius.

Adsorption can be predicted by solving Eq. (3.19) for relation of adsorbed phase density and bulk vapor pressure. Taking type IV (IUPAC classification) isotherms of mesoporous sorption as an example: fluids exist as a dilute phase (vapor) at pressure lower than pore condensation pressure, stay as vapor-liquid equilibrium at pore condensation pressure and turn into dense phase (liquid) by further increasing pressure.[6,31,32,51] For our experiments, the phase transition occurs by increasing temperature at constant bulk vapor pressure,

which can be described as the process of Figure 13a to 13b to 13c. The reverse path captures the adsorption process. In this study, the phase transition of the confined liquid to vapor is termed as the apparent bubble point and determined as the onset of the confined fluid "boiling". It needs to be noted that the confined fluid is connected to bulk vapor and confined supercritical fluid will also vaporize into bulk when confined fluid chemical potential reaches that of bulk atmospheric pressure vapor. Similar desorption phenomenon has been reported[79,80] and further investigated in this work.

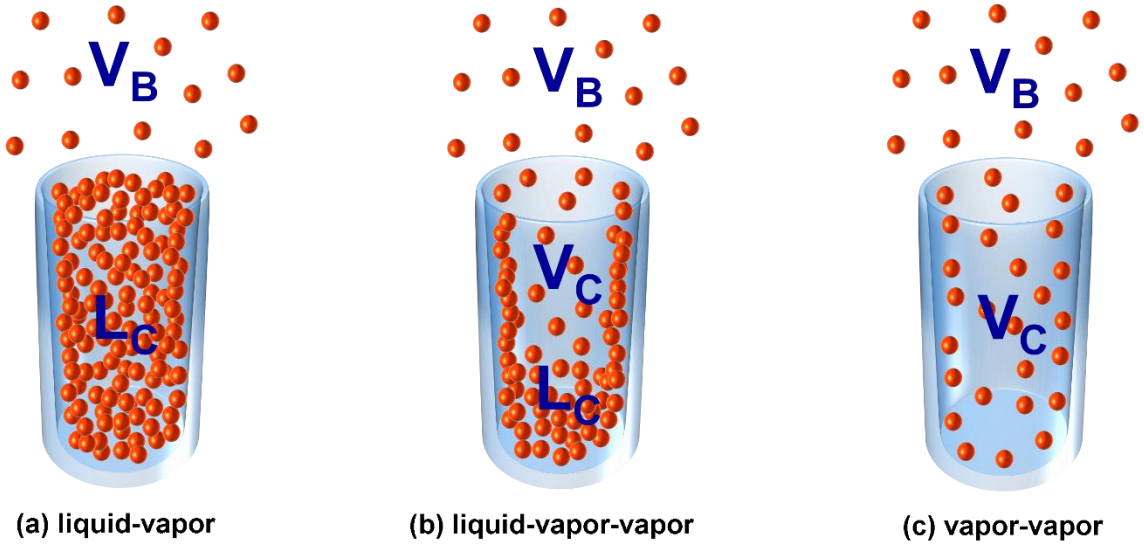

Figure 15. Phase states in adsorption systems by porous media. (a) Confined liquid in equilibrium with bulk vapor. (b) Liquid and vapor are in equilibrium within the pore, which are in equilibrium with the bulk vapor outside. This phase transition is generally termed as capillary condensation/evaporation. (c) Confined vapor in equilibrium with bulk vapor. (a) to (b) to (c) is desorption, and the opposite process is adsorption. L_C: confined liquid; V_C: confined vapor; V_B: bulk vapor.[50]

Table 7. Bulk and confinement parameters in the equation of state: molecular weight (*MW*), critical temperature (T_c), critical pressure (P_c), acentric factor (ω), square well potential depth (ε_p) and width (δ_p).[50]

Parameters		*n*-Hexane	*n*-Octane	*n*-Decane
Bulk	MW (g/mol)	86.178	114.232	142.286
	P_C (kPa)	2968.8	2482.5	2107.6
	T_C (K)	507.4	568.8	617.6
	ω	0.296	0.394	0.490
Confinement	ε_p/k_B (K)	1852	2090	2306
	δ_p/σ	0.5	0.5	0.5

3.2.2 Modeling experimental results

The phase transition boundary is experimentally observed as the bubble point of vaporization (Figure 7). To establish the phase transition criteria for the subcritical confined fluid, the chemical potential of the liquid phase inside the pore and the bulk vapor phase outside the pores are equal, as Eq. (3.20); inside the pore, the coexisting liquid and vapor phase have equal chemical potentials, as Eq. (3.21). *P* is the bulk phase pressure, which is atmospheric pressure in our experiments.

$$\mu_{pore}^{L}\left(\rho^{L}, T, \varepsilon_p, r_p\right) = \mu_{bulk}^{V}(P, T) \tag{3.20}$$

$$\mu_{pore}^{V}\left(\rho^{V}, T, \varepsilon_p, r_p\right) = \mu_{pore}^{L}\left(\rho^{L}, T, \varepsilon_p, r_p\right) \tag{3.21}$$

The equation of state developed by Travalloni *et al*[32] is used in modeling phase equilibria under confinement. As discussed above, ε_p and δ_p are the derived parameters by extending the PR-EOS to cylindrical nanoconfined geometries, and represent the depth and width square-well potential between the fluid molecular and pore wall. Following the literature,[32,81,82] it is specified that $\delta_p/\sigma = 0.5$ (σ is molecular diameter). In the modeling

work, ε_p is determined with experimental results. With the experimentally obtained bubble point temperature at the specific pore size, the interaction potential parameter (ε_p) can be determined. Using the bubble point temperature at 6.0 nm, ε_p is solved from Eqs. (3.20) and (3.21) as $1852k_B$, $2090k_B$ and $2306k_B$ for hexane, octane and decane, respectively (k_B is Boltzmann's constant). At this point, this leads to a full set of pore-size-dependent equation of state for the PVT-d (4D) phase behavior as confirmed by experiment. The EOS parameters are summarized in Table 7.

The phase transition temperature-pore diameter relation is calculated using the ε_p obtained as above (Figure 5, blue curves). A bisection algorithm is applied to solve the Eqs. (3.20) and (3.21) for liquid-vapor phase transition temperature. The calculated bubble points (phase boundaries between liquid and vapor) capture the experimental results well from 4 up to 40 nm: from 40 to 20 nm, the transition temperature increases slowly; from 20 to 4 nm, the transition temperature increases significantly and reaches a peak bubble point temperature around 4 nm.

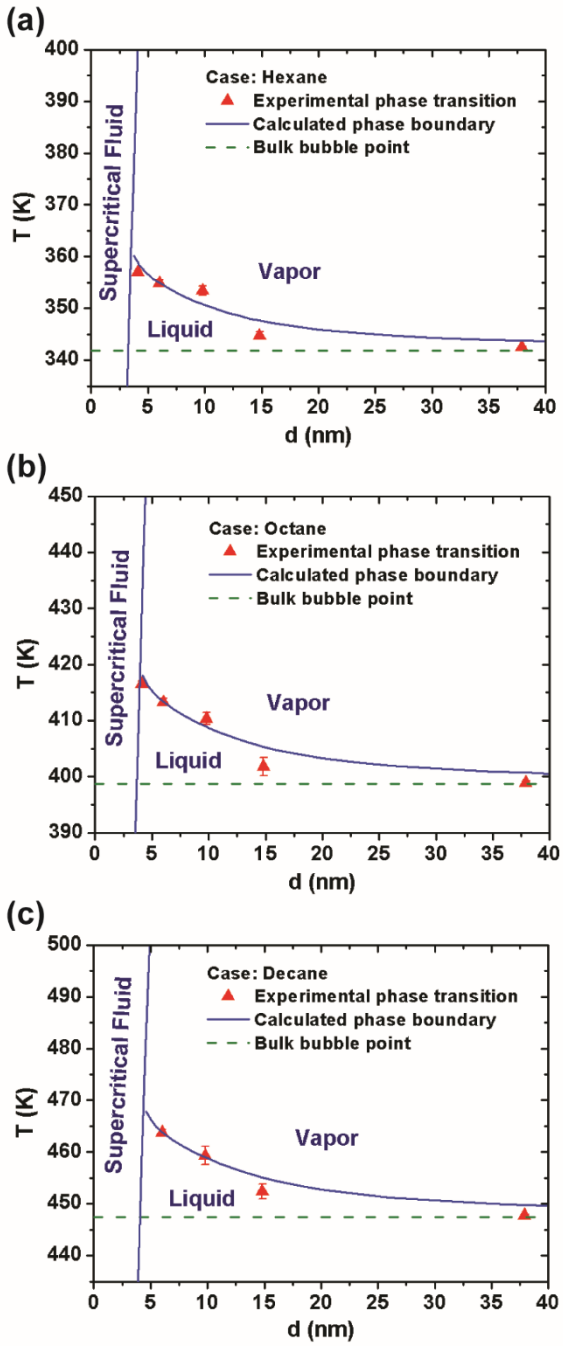

Figure 16. Results of the experimental bubble points and modeled T-d phase diagrams at atmospheric pressure (101.325 kPa) bulk vapor for (a) hexane, (b) octane and (c) decane. The experimental bubble points increased from 37.9 nm to 4.1 nm (red triangles with error bars). The phase boundaries (blue lines) dissect the diagram into three regions: liquid, vapor and supercritical fluid and are calculated from Eqs. (3.20-3.23) for the confined fluid in equilibrium with bulk vapor. Error bars, s.e.m, are obtained from experiments repeated three times.[50]

However, at *ca.* 4 nm, the confined fluid's critical temperature is reached and Eq. (3.21) becomes redundant. Confined critical behavior has been mentioned in previous studies. Evans *et al.* showed that the coexistence of confined liquid and vapor disappeared as the critical temperature is approached.[83] Findenegg *et al.* studied the critical behavior of confined fluids and showed the isochore as a continuous curve in the supercritical region.[7] As the equation of state is pore-size-dependent, solving Eqs. (3.22) and (3.23) gives the critical point[75,84] of the confined fluid for a specific pore diameter. The critical temperature – pore diameter relation is shown as the boundary between supercritical fluid and liquid/vapor region in Figure 5. The critical temperature is generally lower than that of bulk and the critical temperature significantly lowers as the pore size decreases, which are in agreement with previous experimental[7] and simulation studies.[37,39] It is found that at 3.3 and 2.2 nm the experimental phase transition points of confined hexane and octane were in the supercritical region, while for decane, the phase transitions occurred in the supercritical region at 4.1–2.2 nm. The criticality analysis gives important implications in that the critical points exactly lie in the area of the bubble point's change in trend. It can be concluded that the phase behavior of confined hydrocarbons is altered after entering the supercritical state at *ca.* 4 nm.

$$\left(\frac{\partial P}{\partial v}\right)_{T_c} = \left(\frac{\partial^2 P}{\partial v^2}\right)_{T_c} = 0 \tag{3.22}$$

$$\left(\frac{\partial^3 P}{\partial v^3}\right)_{T_c} < 0 \tag{3.23}$$

It would be counterintuitive to observe phase transitions when the fluid is supercritical (e.g. below 4 nm). To rationalize it, it is important to clarify that the case of the bulk-

confined connected system differs from the case of single bulk or confined region system. The phase transitions observed through this experiment represent the confined supercritical fluid into bulk vapor. In the experiment, the bulk vapor pressure was kept constant and by increasing temperature the phase transition from confined supercritical fluid to bulk vapor was triggered. And the phase transition point is defined as the phase equilibrium between the confined supercritical fluid and bulk vapor, shown as in Eq. (3.24). The phase transition observed below 4 nm here is unlikely to involve any solid or glass-like states. If there is any solid or glass-like hydrocarbons in the pore, the temperature needs to in the range of 160 – 220 K or below.[44,85] Phase transitions of confined hydrocarbons has been observed elsewhere by temperature-programmed desorption studies in less than 4 nm nanopores, where the fluid is likely in supercritical state.[39,53,86]

$$\mu_{pore}^{sup}\left(\rho^{sup}, T, \varepsilon_p, r_p\right) = \mu_{bulk}^{V}(P, T) \tag{3.24}$$

Adsorption/desorption equilibrium in nanoporous media can be divided as fluid phase equilibrium where the confined fluid is in (i) subcritical state Eqs. (3.20-3.21) or (ii) supercritical state Eq. (3.24). From that point of view, the phase transition of confined supercritical fluid to bulk vapor can be treated as desorption and Eq. (3.24) is consequently regarded as a specific form of sorption equilibrium. To solve Eq. (3.24) for phase transition temperature (T), the confined supercritical fluid density (ρ^{sup}) is experimentally estimated by identifying the fluid density when the pores are saturated. In relating the experimental fluid density to the molar volume in the EOS, the volume translation parameter (c_{vt}) is

obtained by applying the confined fluid critical temperature from Eqs. (3.23) and (3.24) in Monnery's correlation.[87] The parameters c_{vt} are -0.0056 m^3/kmol, -0.0825 m^3/kmol and -0.1375 m^3/kmol at 3.3 nm for hexane, octane, decane, respectively, and -0.0765 m^3/kmol for decane at 4.1 nm. The calculated confined phase transition point (desorption temperature) at 3.3 nm is 350.7 K, 407.8 K, 456.7 K for hexane, octane, and decane, respectively. And the desorption temperature at 4.1 nm for decane given from calculation is 469.9 K (Table 8). Besides, the phase transition at 2.2 nm cannot be calculated with this method, since there's no major peak for confined fluid from DSC thermograms and the confined fluid density cannot be obtained.

Table 8. Experimental and calculated desorption temperatures of fluid below 4.1 nm.[50]

	n-Hexane		*n*-Octane		*n*-Decane	
	Expr. T_{desorb} (K)	Calc. T_{desorb} (K)	Expr. T_{desorb} (K)	Calc. T_{desorb} (K)	Expr. T_{desorb} (K)	Calc. T_{desorb} (K)
SBA-16 (3.3 nm)	348.4±0.3	350.7	405.4±0.7	407.8	455.2±0.7	456.7
CPG-4[a] (4.1 nm)	-	-	-	-	465.2±0.3	469.9

[a]In 4.1 nm nanopore, hexane and octane are determined as in subcritical state, so they are not solved as supercritical fluid desorption.

The work above investigated the confined phase equilibria by experimental isobaric thermal analysis and phase equilibria modeling with EOS. Here we show the application of the EOS modeling by predicting capillary sorption isotherms using the same parameters ε_p and δ_p as obtained above. In previous studies, the phase behavior of confined fluid was accessed through adsorption/desorption of fluid in mesoporous media at constant temperature. The phase equilibria for single component sorption equilibrium is given as Eq. (3.24), where ρ_a is the adsorbed phase density.[31] Matsumoto *et al* studied the *n*-hexane

adsorption by surface silylated mesoporous material MCM-48,[88] which is close to the materials used in this work on surface chemical properties. Their experimental isotherms of hexane in surface-modified MCM-48 (2.4 nm) at 298 K is shown as triangles in Figure 17. We model the adsorption isotherm by solving Eq. (3.25) for ρ_a at specific pressure P. (c_{vt} -0.0062 m^3/kmol) The predicted adsorption isotherm generally correlates well with the experimental results as a Type IV curve: the condensation mainly occurs at 3 kPa < P < 6 kPa; above 8 kPa, the adsorption amount increases very little as the pores are saturated with adsorbate. However, some deviations can be found such as the early adsorption uptake and saturation density. The deviations may arise from the limitation of the model to fluid in ideal cylindrical pore. And because of the minor difference in pore connectivity and surface roughness, parameters characterized from our experiment may not perfectly reflect the properties of the materials by Matsumoto.

$$\mu_{pore}(\rho_a, T, \varepsilon_p, r_p) = \mu_{bulk}^{V}(P, T) \tag{3.25}$$

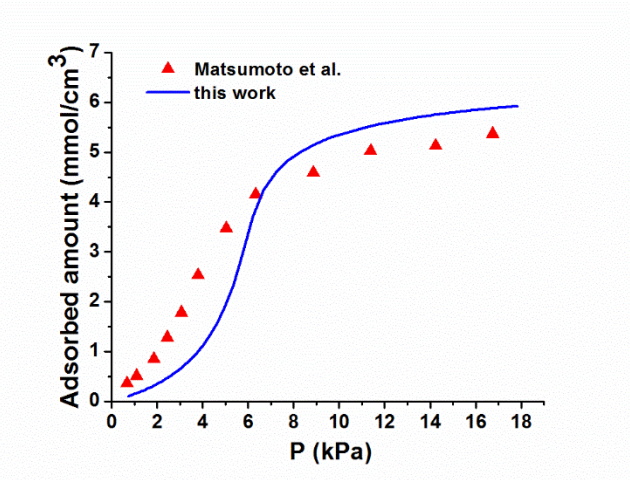

Figure 17. Experimental results and predicted isotherm of *n*-hexane adsorption in MCM-48 OSM2 at 298 K. The material is prepared by silylating the surface of MCM-48 and the pore diameter is 2.4 nm. The y-axis was originally reported as filling ratio and here it is converted into adsorbed amount (mmol/cm^3).[88] In this work, the isotherm is calculated from (3.25) using the completed EOS as above. The predicted isotherm correlates well with the experimental results on condensation and pore saturation pressure.[50]

The confinement parameters of square-well depth (ε_p) and width (δ_p) for fluid-pore surface interactions are required to be determined from experiments. We developed an isobaric measurement of differential scanning calorimetry (DSC) for fluid in nanopores,[74] and the phase transition temperatures of *n*-hexane, *n*-octane and *n*-decane were measured in pores from 2.0 to 37.9 nm. The confinement parameters of ε_p and δ_p were determined accordingly. The phase boundaries between liquid, vapor, and supercritical fluid predicted by PR-C EOS overlap very well with experimental findings.[50] Recently, we measured the phase transitions of intermediate to heavy hydrocarbons in nanopores and obtained the confinement parameters (ε_p, δ_p) for C_5~C_{14}. For the light hydrocarbons (C_1~C_4), the parameters were determined by fitting the adsorption isotherms in nanoporous media.[13,88,89]

In calculating the confinement parameters by experimental data, we observed that, for a specific species, ε_p and δ_p are in negative correlation and the product (area of square well) is positively correlated to molecular weight. Therefore, we suggest a normalized fluid-pore surface affinity factor, κ, as the product of ε_p and δ_p over molecular weight Eq. (3.26). The κ factor describes the interaction strength between the fluid and pore surface per molecular weight. On a given surface, κ factor should be dependent on the fluid molecular structure. The κ factor relation to molecular weight of n-alkanes is shown in Figure 18. In practice, it is suggested that $\delta_p/\sigma = 0.5$, in agreement with the set in molecular simulations,[90,91] as too large or small ratio may lead to deviated phase equilibrium.[81]

$$\text{Fluid-pore surface affinity factor: } \kappa = \frac{\varepsilon_p \cdot \delta_p}{MW} \tag{3.26}$$

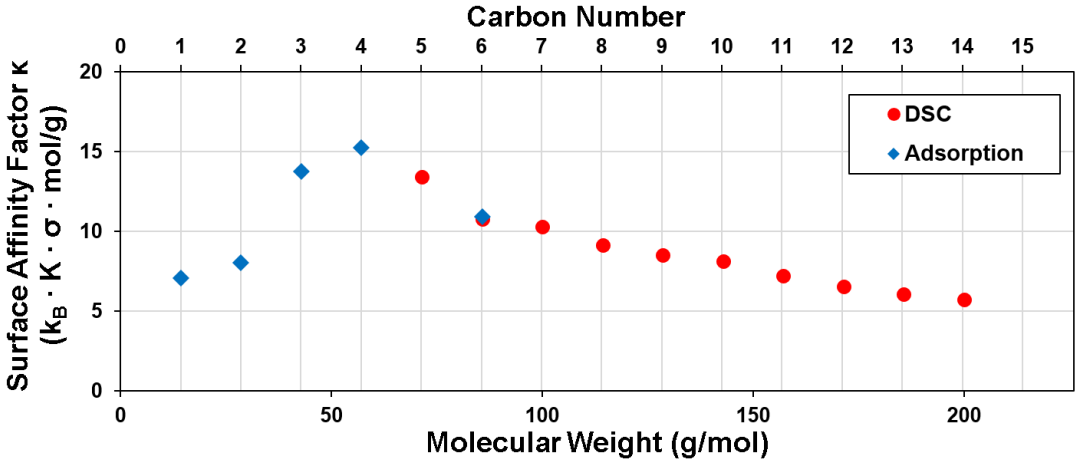

Figure 18. Fluid-pore surface affinity factor κ in relation to molecular weight and carbon number of *n*-alkanes. $\boldsymbol{\varepsilon_p}$ is defined with the unit of k_B·K (k_B: Boltzmann constant) and $\boldsymbol{\delta_p}$ is defined with the unit of fluid molecular diameter (σ). Confinement parameters for C_1~C_4 and C_6 are obtained by fitting the adsorption isotherms in nanopores of diameters 2.4-3.8 nm.[13,88,89] Parameters for C_5~C_{14} are determined by the liquid-vapor phase transition temperature in 6.0 nm pore, measured by differential scanning calorimetry (DSC). All experimental measurements utilized nanoporous silica with silylated surface.[76]

It is worth noting that the confinement parameters in Figure 18 are determined from the DSC/adsorption experiments with silylated nanoporous silica. The silylation modification renders organic characteristics to the media surface, which are experimentally observed as hydrophobicity (non-water-wet) and oleophilicity (oil-wet).[92] In that, the silylated surface makes the experimental nanoporous media a reasonable analog to organic matter (OM), where most nanopores are located in shale.[93,94]

4. PHASE BEHAVIOR OF SHALE RESERVOIR FLUIDS*

4.1 Multi-Scale fluid phase behavior model

The scales of porous geometries in shale reservoirs range across several orders of magnitude. Natural fractures are commonly found to have the widths of a few micrometers to millimeters.[95,96] After hydraulic-fracture stimulation, macro-scale fractures are introduced to the formation in connection to the wellbore,[97] and a significant amount of natural microfractures are reactivated.[98] Within the shale matrix, the pore sizes are in the range of nanometers to micrometers. The matrix pores are classified into mineral pores and organic-matter (OM) pores. The minerals pores are in micrometers, and the organic-matter pores range from a few to hundreds of nanometers, though organic-matter bubble pores can be a few micrometers.[93,94] The actual pore size distributions usually vary from case to case.[99,100] Cho, et al. [101] comparatively measured the pore sizes of shale samples by mercury injection capillary pressure (MICP) and discovered several pore size distribution patterns. The middle Bakken shales exhibit a unimodal pore size distribution (30~50 nm) or a bimodal pore size distribution (30 nm and 100 nm). For the Niobrara formation, the pore size distributions are mostly unimodal, and the pore diameters range from 4 to 11 nm. Recently, Ko, et al. [94] presented a quantitative analysis of pore structures with Eagle Ford shale samples by different analytical methods. By SEM imaging and pore-tracing, they identified that the pore diameters distribute bimodally at 10-30 nm and 35-

* Part of this chapter is reprinted with permission from "Multi-Scale Fluid Phase Behavior Simulation in Shale Reservoirs by a Pore-Size-Dependent Equation of State" by S. Luo, J. L. Lutkenhaus, and H. Nasrabadi, 2017. SPE Proceedings, SPE-187422-MS, Copyright [2017] by Society of Petroleum Engineers.

1000 nm. However, the SEM/pore-tracing method is limited to resolving pore diameters from ca. 20 nm to 15 μm (Figure 19, blue columns). Nitrogen adsorption is able to measure pores from diameter 0.3 to 200 nm, and the measurement shows significant volumetric portions of nanopores smaller than 10 nm (Figure 19, red shaded columns).[94] SEM/pore-tracing and nitrogen adsorption analyses combine to form the whole picture of pore size distribution: both nanopores and macropores constitute important porosities in the Eagle Ford shale.

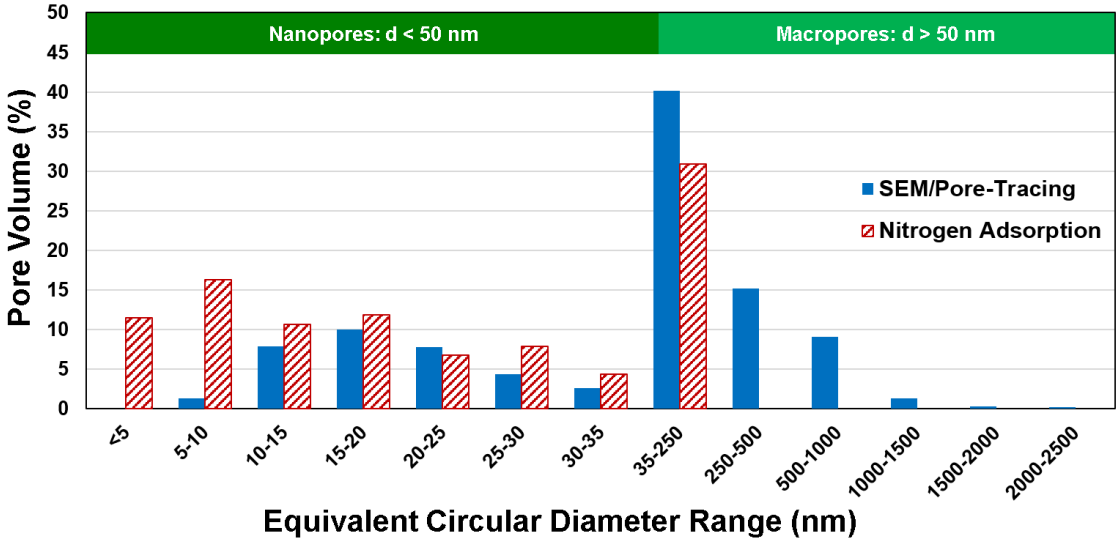

Figure 19. Pore size distribution of an upper Eagle Ford core by SEM/pore-tracing and nitrogen adsorption analyses.[94] SEM/pore-tracing method resolves pore diameters from ca. 20 nm to 15 μm, and nitrogen adsorption measures pores in 0.3-200 nm. The combination of results from two methods forms the whole picture of pore size distribution (1 μm = 1000 nm).[76]

A multi-scale model of fluid in shale is conceived based on distinct phase behaviors under different confining scales: the porous space is divided into a bulk region and nanopores (Figure 20). The bulk region refers to the hydraulic fractures, natural fractures and

macropores in the shale matrix, where the reservoir fluid behaves as bulk fluid; the nanopores are the pores in the matrix with a diameter less than 50 nm, where the phase behavior deviates from the bulk. Due to the strong confinement in small nanopores (<10 nm) but weak confinement above 30 nm,[50] the nano-porosity is further discretized into pores of several diameters ($d_1, d_2, d_3, \ldots$). The multi-scale phase behavior model is analogous to the dual/multiple porosity (permeability) model,[102,103] whereas in this model we specifically investigate the thermodynamic phase equilibria among pore geometries of multiple scales. In this model, the pressure-volume-temperature relation and fluid compositions in nanopores and bulk region are dependent on the global phase equilibrium.

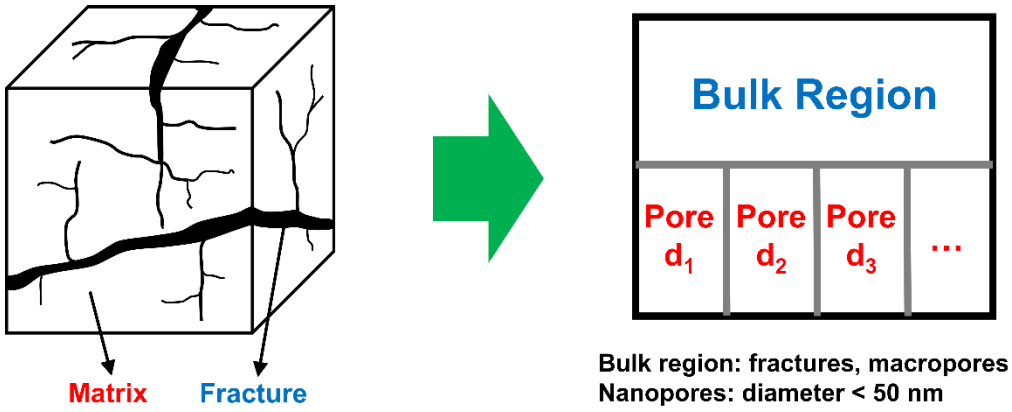

Figure 20. Multi-scale model for fluid phase behavior in fractured shale reservoirs. The shale porous space is divided into the bulk region where the fluid shows bulk behavior and nanopores where the fluid phase behavior is altered under the nano-confinement effect. The phase behavior of the whole system is the thermodynamic equilibria among the bulk region and multiple sizes of nanopores.[76]

Herein, we simulate the depletion of the shale reservoir by modeling the constant composition expansion (CCE) of the multi-scale system. The bulk region volume is repeatedly expanded, and the volumes of nanopores are fixed at the initial condition, in

light that the volumetric flow primarily takes place through the bulk-scale geometries such as fractures, while the transmissivity from small pores is very low.[104,105]

We consider the isothermal-isochoric fluid phase equilibria among the bulk region and NP sizes of nanopores with pore diameters noted as $d_1, d_2, \dots, d_{NP}$. The multi-scale system is defined with given moles of NC components $(n_1, n_2, \dots, n_{NC})$, volumes (bulk region volume V_b and volumes of nanopores $V_1, V_2, \dots, V_{NP}$) and temperature (T). The numbers of fluid phases are noted as NF_b phases in the bulk region and NF_k phases in the nanopore of diameter $d_k (k = 1,2, \dots, NP)$. The total Helmholtz free energy (A) is the sum of the bulk region and all nanopores Eqs. (4.1)-(4.3). The constraints are the conservations of moles and regional volumes Eqs. (4.4)-(4.6), where *i* denotes the properties of component *i* and *j* denotes the properties for phase *j*.

The total Helmholtz free energy of the bulk- NP nanopores system:

$$A = A_b + \sum_{k=1}^{NP} A_{p,k} \tag{4.1}$$

$$A_b = \sum_{j=1}^{NF_b} \left(-P_{j,b} V_{j,b} + \sum_{i=1}^{NC} n_{ij,b} \mu_{ij,b} \right) \tag{4.2}$$

$$A_{p,k} = \sum_{j=1}^{NF_k} \left(-P_{j,k} V_{j,k} + \sum_{i=1}^{NC} n_{ij,k} \mu_{ij,k} \right) \tag{4.3}$$

The constraints are molar and volumetric conservations:

$$\sum_{j=1}^{NF_b} V_{j,b} = V_b \tag{4.4}$$

$$\sum_{j=1}^{NF_k} V_{j,k} = V_k \quad \forall k \in \{1,2,\dots,NP\} \tag{4.5}$$

$$\sum_{j=1}^{NF_b} n_{ij,b} + \sum_{k=1}^{NP}\sum_{j=1}^{NF_k} n_{ij,k} = n_i \tag{4.6}$$

Under isothermal conditions:

$$T_b = T_{p,1} = T_{p,2} = \cdots = T_{p,NP} \tag{4.7}$$

The global phase equilibrium of the multi-scale system can be determined as the state of minimized Helmholtz free energy.[32,78,84] At the first order optimality conditions, the system naturally satisfies the equality of chemical potentials for any component *i* among phases from all regions and equality of pressures among phases within each region:

$$\mu_{i,b} = \mu_{i,1} = \mu_{i,2} = \cdots = \mu_{i,NP} \tag{4.8}$$

$$\mu_{i,b} = \mu_{ij,b} \quad \forall j \in \{1,2,\dots,NF_b\} \tag{4.9}$$

$$\mu_{i,k} = \mu_{ij,k} \quad \forall j \in \{1,2,\dots,NF_k\} \; and \; \forall k \in \{1,2,\dots,NP\} \tag{4.10}$$

4.2 Constant composition expansion

4.2.1 Case description

We use a case of modified black oil from the Eagle Ford liquid-rich shale (LRS) by Orangi, et al. [106] The reservoir fluids are grouped into 6 pseudo-components. The PR-C EOS parameters are listed in Table 10 and 11, where the critical properties, acentric factors, volume shift parameters and binary interaction parameters are bulk species parameters. The confinement parameters ε_p and δ_p of the pseudo-components are obtained by interpolating or extrapolating using the κ factor-molecular weight plot in Figure 18 (assuming $\delta_p/\sigma = 0.5$).

The reservoir conditions are presented in Table 9.[106] The shale oil reservoir is initially undersaturated at 6000 psia, 240 ^{o}F. The ratio between the bulk region volume and nanopores volume (diameter < 50 nm) should be dependent on the exact formation and also the specific location within the reservoir. Ko, et al. [94] showed that for Eagle Ford shale the bulk region volume is similar to the volume of nanopores (Figure 19). Herein, we assume the initial volume ratio between the bulk region and nanopores as 1:1, except for the single-scale case where all the space is assigned as bulk. In simulating the constant composition expansion, the bulk region volume is repeatedly expanded while the volumes of nanopores are kept constant, as the volumetric flow mainly takes place through the bulk-scale geometries (e.g. fractures).[104,105] The bulk region is given a typical macropore diameter of 10 microns. The diameters of nanopores are specified as 5 nm or 15 nm based on the nano-scale pore size distribution of an Eagle Ford shale (Figure 19).[76]

Table 9. Reservoir conditions of an Eagle Ford liquid-rich shale (LRS).[76]

Properties	Value
Reservoir Temperature	240 ^{o}F
Initial Reservoir Pressure	6000 psia
Initial V_{bulk}:$V_{nanopores}$	1:01
Reservoir Fluid Type	Oil

Table 10. PR-C EOS properties for Eagle Ford oil modified from Orangi *et al*.[76,106]

Species	MW (g/mol)	T_C (°R)	P_C (psia)	ω	VSP	ε_p/k_B (K)	δ_p/σ	Mole Fraction
N_2-C_1	16.07	343.02	672.7	0.01306	-0.154	227	0.5	0.3130
C_2	30.07	549.8	708.4	0.0986	-0.1002	481	0.5	0.0431
CO_2-C_3	44.08	644.14	690.06	0.16954	-0.083	1209	0.5	0.0543
C_4-C_6	72.04	839.26	488.86	0.24541	-0.0386	1932	0.5	0.1330
C_7-C_{10}	114.4	1060.5	402.8	0.3739	0.0191	2091	0.5	0.1630
C_{11+}	238.07	1391.01	234.71	0.67743	0.18412	2407	0.5	0.2935

Table 11. Binary interaction parameters for Eagle Ford oil from Orangi *et al*.[76,106]

	N_2-C_1	C_2	CO_2-C_3	C_4-C_6	C_7-C_{10}	C_{11+}
N_2-C_1	0.000	0.000	0.005	0.021	0.038	0.077
C_2	0.000	0.000	0.004	0.018	0.034	0.072
CO_2-C_3	0.005	0.004	0.000	0.006	0.016	0.045
C_4-C_6	0.021	0.018	0.006	0.000	0.002	0.019
C_7-C_{10}	0.038	0.034	0.016	0.002	0.000	0.008
C_{11+}	0.077	0.072	0.045	0.019	0.008	0.000

4.2.2 Single-Scale PVT (conventional reservoirs)

The PVT model using PR-C EOS is firstly validated by simulating the fluid PVT at the single bulk scale, i.e. the conventional reservoir conditions. The single-scale system is set up with a bulk pore diameter of 10 μm. The phase diagram and pressure-volume relations are calculated. The results from our model match with the simulation output of a commercial software using PR EOS (Figure 21). The bubble point pressure of the bulk fluid is 2074 psia. In the following discussions, the single bulk-scale PVT is referred to as conventional reservoir phase behavior.

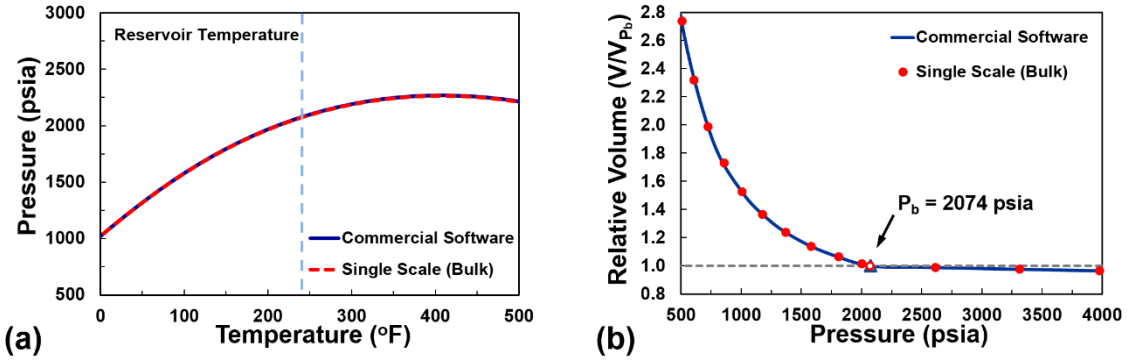

Figure 21. (a) Phase diagram and (b) pressure-volume plot. The red dashed lines in Fig. 5a and red round symbols in Figure 19b show results from PR-C EOS PVT model using a single bulk size (pore diameter: 10 microns). In Figure 19b, the open symbol mark the bubble point pressure. The results agree with the output by a commercial software using PR EOS (solid blue lines).[76]

4.2.3 Dual-Scale PVT

The dual-scale constant composition expansion (CCE) is simulated by the multi-scale PR-C EOS model. The bulk-scale size is 10 μm, and the nanopore diameter is specified as 15 nm (Figure 22), representing a major nanopore diameter from the Eagle Ford shale pore size distribution in Figure 19.[94] The initial volumes of the bulk region and nanopores are assumed equal. The bulk region volume is expanded while the nanopore volume is fixed to consider that most volumetric flows take place through the bulk geometries.[104]

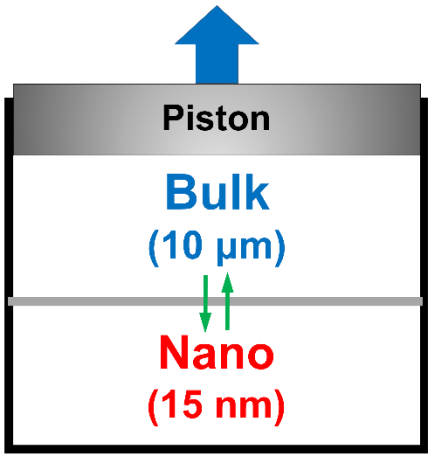

Figure 22. Dual-scale model (bulk-15 nm) for constant composition expansion. The bulk region is given a pore diameter of 10 microns, and the nanopores are specified with the diameter of 15 nm. The initial volumes of the bulk region and nanopores are assumed equal. The bulk space is expanded, and the volume of nanopores is fixed. The component exchange between the bulk region and nanopores is enabled for global phase equilibrium at each stage (1 μm = 1000 nm).[76]

The molar density profiles of the simulated CCE are shown in Figure 23. The first bubble forms in the bulk region at 2002 psia, which is lower than the conventional reservoir bubble point (2074 psia). At the undersaturated conditions (P > 2002 psia), the fluids in both the bulk region and nanopores are in the liquid state, and the molar density is slightly higher in nanopores. There are some small compositional differences: the molar densities of C_2, CO_2-C_3, C_4-C_6 are higher in nanopores than in the bulk region, and these species are associated with relatively large surface affinity factors (Figure 18). As the pressure falls below the bubble point (2002 psia), the gas phase expands in the bulk region; the nanopores release the light hydrocarbons (Figure 24a) but retain the intermediate to heavy components (C_7-C_{10}, C_{11+}) (Figure 24 and 24c). Intermediates C_4-C_6 are not released into the bulk gas phase from 15 nm pores until the pressure falls below ca. 300 psia (Figure

24b). Due to the confinement effect and accumulations of heavy components (Figure 24c), the fluid in the nanopores remains undersaturated both above and below the bubble point. The liquid phase in the bulk region undergoes a compositional shift towards the heavier side in a similar manner with the liquid in nanopores (Figure 23). Assuming an ultimate recovery at the pressure of 501 psia (Figure 23), the nanopores retain large amounts of intermediate to heavy hydrocarbons, which indicates a significant oil loss in shale nanopores.

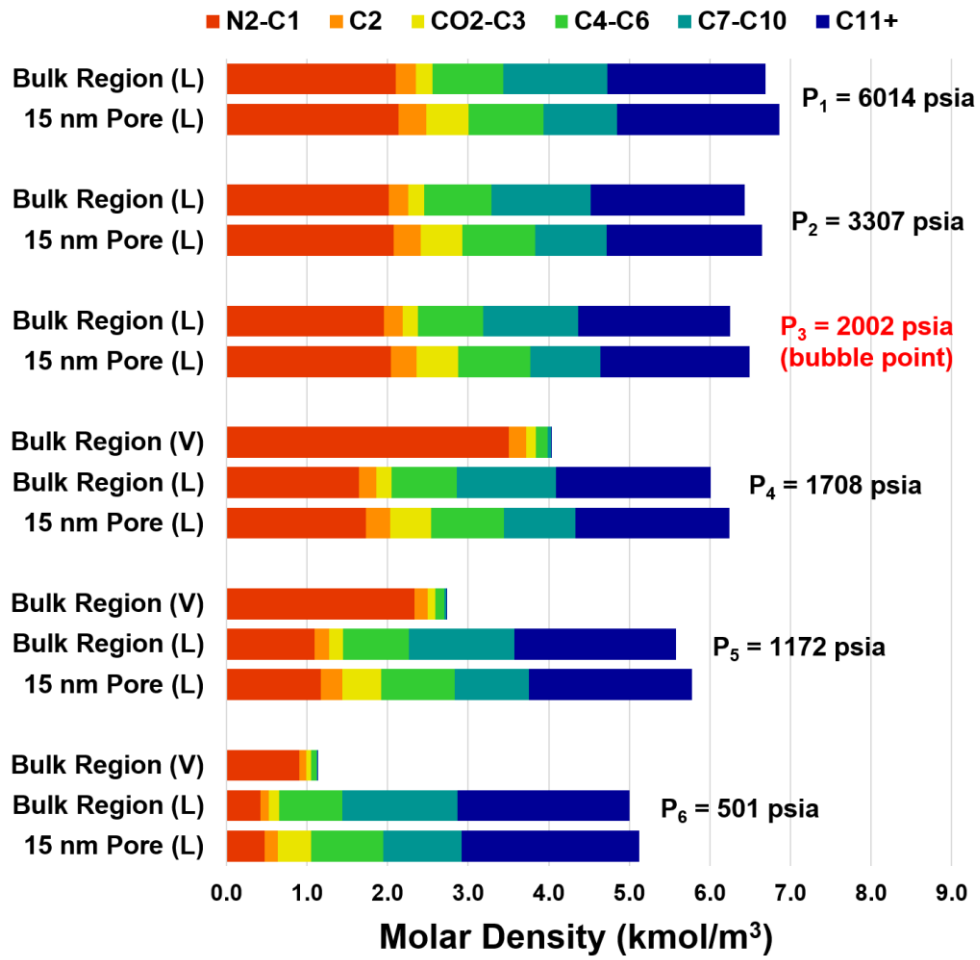

Figure 23. Molar density profiles of all phases at selected pressures in the dual-scale constant composition expansion. The length of a cylinder section refers to the actual molar density (kmol/m^3) of a specific species in the corresponding phase. The noted pressure is the bulk region pressure. The bubble point pressure is 2002 psia (72 psia lower than the conventional reservoir fluids), and the first bubble emerges from the bulk region. As the pressure is lowered, the gas phase expands in the bulk region, but in 15 nm nanopores the fluid is always undersaturated. In the end, a significant amount of intermediate and heavy components are trapped in nanopores.[76]

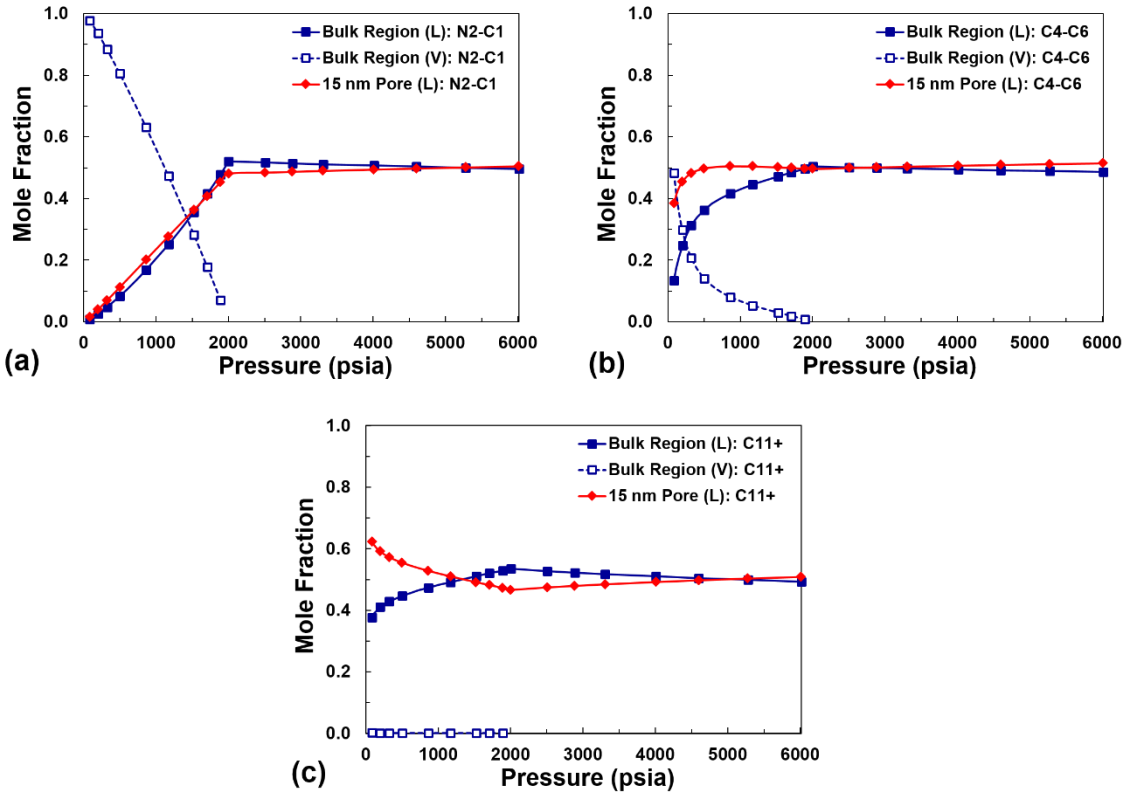

Figure 24. Mole fractions of (a) light component: N_2-C_1, (b) intermediate: C_4-C_6, and (c) heavy component: C_{11+} distributed in various phases during the dual-scale constant composition expansion. The bubble point pressure is 2002 psia. Below the bubble point, N_2-C_1 is quickly released from the bulk and confined liquid phases into the bulk gas phase, and C_4-C_6 is released into the gas phase from the nanopores at a very low pressure (ca. 300 psia). C_{11+} accumulates in the liquid phase of the nanopores below the bubble point.[76]

The liquid volumetric saturation of the dual-scale shale system is compared with that of conventional reservoir fluids in Figure 25a. In nanopores, the reservoir fluid is always liquid. The bubble point is slightly suppressed, and the liquid saturation in the bulk region quickly declines with decreasing pressure. The liquid saturation in the bulk region is generally lower (5~15%) than those in conventional reservoirs. In the oil production from shale, the fast decline of liquid saturation should lead to a sharp rise of GOR once entering the two-phase stage. This can be correlated to the observations by Jones [107] that in LRS

production a quick rise of GOR occurs after the flowing bottom hole pressure falls below bubble point. The pressure-volume relation is plotted in Figure 25b. The volume of shale nanopores is fixed, and the bulk region volume expands faster with decreasing pressure than it does in the conventional reservoir.

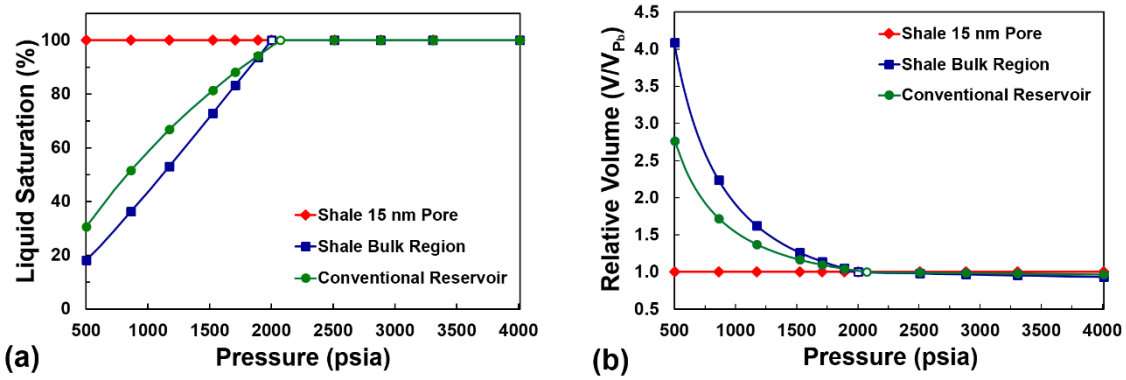

Figure 25. (a) Liquid volumetric saturation of each region in relation to pressure: in the bulk region, P_b is slightly suppressed and, at the two-phase stage, the liquid saturation drops faster than that in the conventional reservoir. In nanopores (15 nm), the fluids are undersaturated at all pressures. (b) Pressure-volume relations: the nanopore volume is fixed. The bulk region expands with lowered pressure, at a rate faster than that in conventional reservoirs. The bubble point pressure for shale is marked as an open blue square, and for conventional reservoirs it is marked as a green circle.[76]

4.2.4 Triple-Scale PVT and criticality

As shown by nitrogen porosimetry (Figure 19), there is a significant amount of small nanopores (diameter < 10 nm) in shale.[94] To consider this, we refine the model by introducing the 5 nm pores in the nanopores region. The initial volume ratio is specified as 3:2:1 for the bulk region, 15 nm, and 5 nm pores (Figure 26). In the same manner with the dual-scale CCE, the bulk volume is expanded, but the volumes of nanopores are fixed.

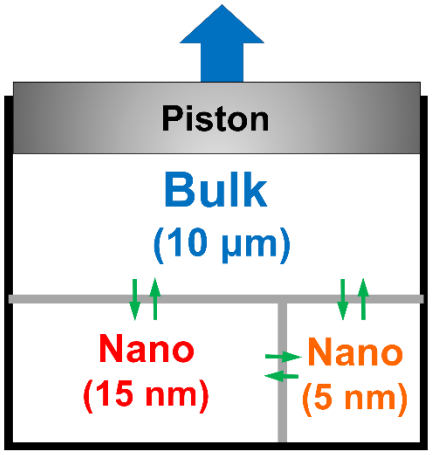

Figure 26. Triple-scale model (bulk-15 nm-5 nm) for constant composition expansion. The bulk region is given a pore diameter of 10 microns and the nanopores are specified with the diameters of 15 and 5 nm. The initial volumes of the bulk region, 15 nm, and 5 nm nanopores are assumed as 3:2:1. The bulk space is expanded and the volumes of nanopores are fixed. The component exchanges between the bulk region, 15 nm, and 5 nm pores are enabled for global phase equilibrium at each stage (1 μm = 1000 nm).[76]

The molar density profiles of the triple-scale CCE are shown in Figure 27. The bubble point pressure is 1936 psia, and the first bubble occurs in the bulk region, which is similar to the behavior in the dual-scale CCE. Above the bubble point, fluids in all regions are in the liquid state. However, the compositions in 5 nm pores significantly deviate from those in 15 nm pores and the bulk region. The mole percentages of light and intermediate species are high in 5 nm pores, but the mole percentage of heavy component (C_{11+}) is relatively low (Figure 27). The fluid in 5 nm pores is classified as volatile oil. The fluids in the bulk region and 15 nm pores are typical black oil by composition. As the pressure decreases below the bubble point, the gas phase in the bulk region expands and gathers a great portion of light components (N_2-C_1, C_2) (Figure 28a). The fluids in nanopores become further undersaturated by releasing the light components and accumulating the

intermediate to heavy components (Figures 27, 28b and 28c). During the two-phase stage (of the bulk region), the compositional change in 5 nm pores shifts the fluid type from volatile oil towards black oil. Assuming the ultimate recovery pressure as 500 psia (Figure 27), large amounts of intermediates and heavy hydrocarbons are trapped in 5 and 15 nm pores.

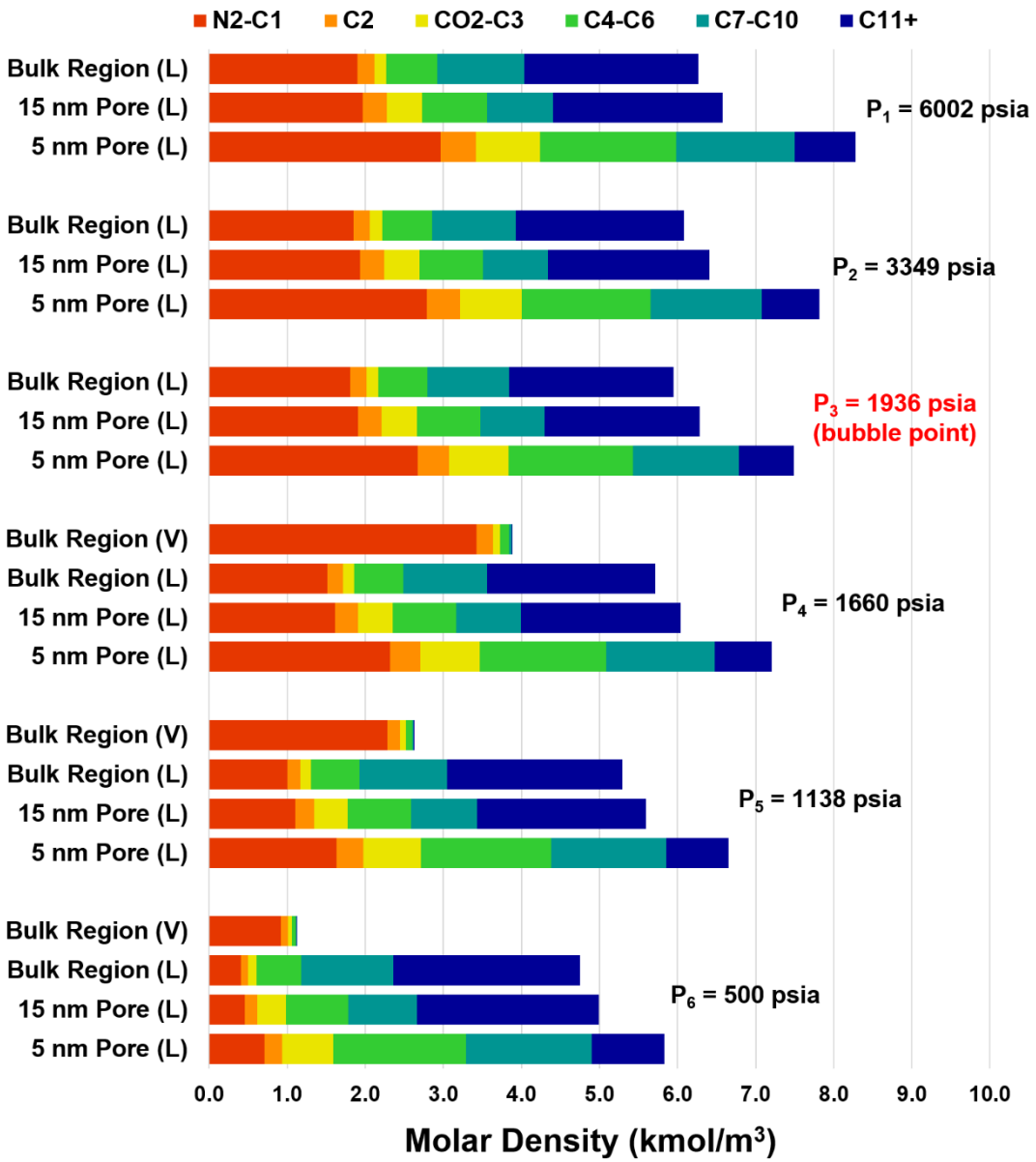

Figure 27. Molar density profiles of all phases at selected pressures in the triple-scale constant composition expansion. The length of a cylinder section refers to the actual molar density (kmol/m^3) of a specific species in the corresponding phase. The noted pressure is the bulk region pressure. The bubble point pressure is 1936 psia (138 psia lower than the conventional reservoir fluids), and the first bubble emerges from the bulk region. As the pressure is lowered, the gas phase expands in the bulk region, but the fluids are always undersaturated in 5 and 15 nm nanopores. The 5 nm pores have relatively high fractions of C_1~C_6. In the end, a significant amount of intermediate and heavy components are trapped in nanopores.[76]

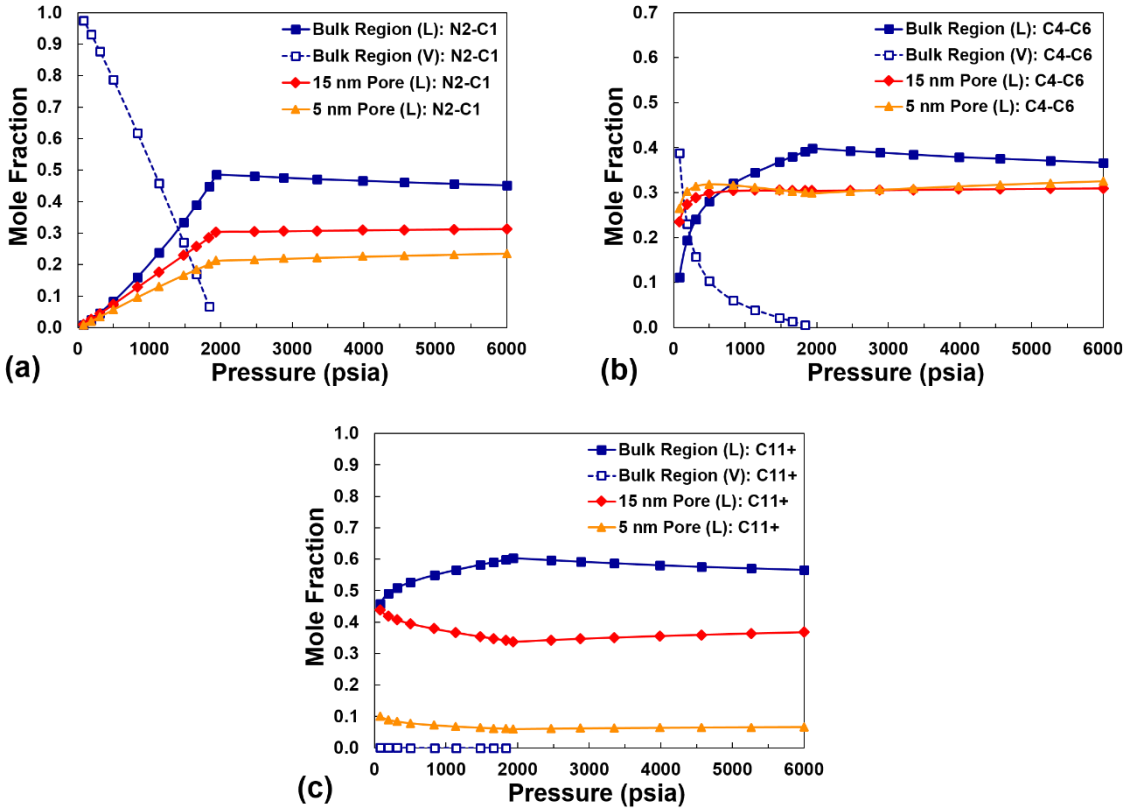

Figure 28. Mole fractions of (a) light component: N_2-C_1, (b) intermediate: C_4-C_6, and (c) heavy component: C_{11+} distributed in various phases during the triple-scale constant composition expansion. The bubble point pressure is 1936 psia. Below the bubble point, N_2-C_1 is quickly released from the bulk and confined liquid phases into the bulk gas phase, and C_4-C_6 is released into the gas phase from the nanopores at a very low pressure (ca. 300 psia). C_{11+} accumulates in the liquid phases of the nanopores (5 and 15 nm) below the bubble point.[76]

The oil properties are also investigated by examining the critical temperature. For each stage in the CCE, the critical temperature of fluid in a specific size of pore is calculated from Eqs. (4.11) and (4.12).[84] Above the bubble point (P > 1936 psia), the critical temperature of the liquid-state fluid in the nanopores (15 and 5 nm) is lower than those in the bulk region. The decrease of the critical temperature in nanopores is consistent with previous findings from adsorption experiments[7] and molecular simulations.[38,40] By differential scanning calorimetry, we also observed that the supercriticality of

hydrocarbons was induced by confinement effects in the nanopores less than ca. 4 nm in diameter.[50] In 5 nm pores, due to the confinement effect and high fractions of light hydrocarbons, the critical temperature is significantly lowered to ca. 263 ^{o}F, which is slightly above the reservoir temperature (240 ^{o}F). In this scenario, the fluid is near-critical volatile oil (Figure 29). Below the bubble point, the critical temperature in the nanopores increases with decreasing pressure, as the liquid-state fluid in the nanopores become richer in heavy hydrocarbons. In 5 nm pores, the compositional change is so large that it ultimately turns the fluid to black oil. As the fluid composition changes in the nanopores, the viscosity is expected to alter notably, which should significantly affect the fluid flow during the later stage of production in liquid-rich shale.

$$\left(\frac{\partial P}{\partial v}\right)_{T_C} = \left(\frac{\partial^2 P}{\partial v^2}\right)_{T_C} = 0 \tag{4.11}$$

$$\left(\frac{\partial^3 P}{\partial v^3}\right)_{T_C} < 0 \tag{4.12}$$

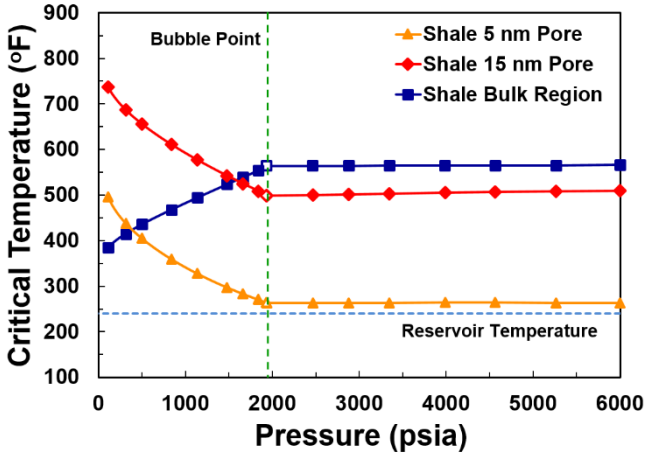

Figure 29. Critical temperatures of fluid in the bulk region/nanopores with respect to pressure over the constant composition expansions. The reservoir temperature is 240 °F (light blue dashed line, horizontal) and the bubble point is 1936 psia (green dashed line, vertically crossing the open symbols). At the undersaturated stage, the fluid in 5 nm pores is (near-critical) volatile oil. As the pressure falls below the bubble point, the fluid critical temperature in 5 nm pores shifts away from the reservoir temperature, and the fluid type turns into black oil.[76]

The liquid volumetric saturation-pressure behavior in the triple-scale system (bulk-15 nm-5 nm) is similar to the dual-scale behavior. The bubble point (1936 psia) is suppressed, and the liquid saturation decreases as the bulk region fluid enters the two-phase state (Figure 30a). The impact on production GOR can be referred to the discussions in the dual-scale section. The bulk region expands remarkably with decreasing pressure, and by assumption, the volumes of the nanopores are fixed (Figure 30b).

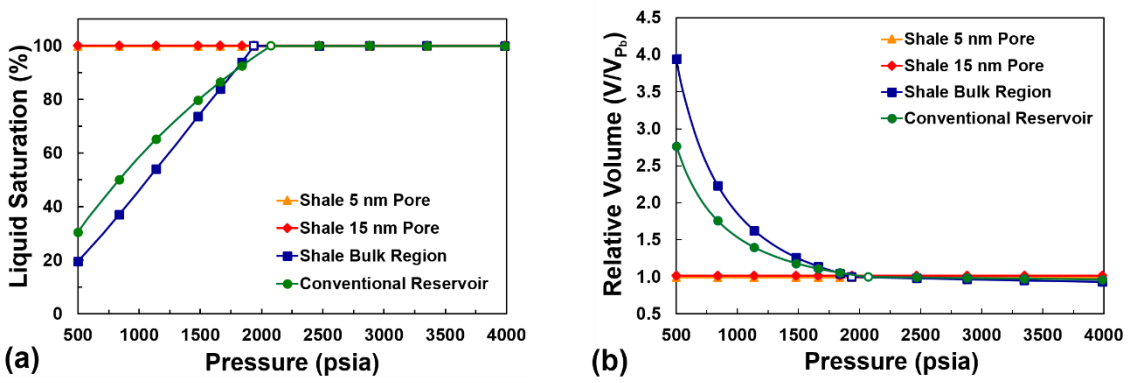

Figure 30. (a) Liquid volumetric saturation of each region in relation to pressure: in the bulk region, P_b is suppressed, and the liquid saturation declines faster than that in the conventional reservoir. In nanopores (5 and 15 nm), the fluid is undersaturated at all pressures. (b) Pressure-volume relations: the nanopore volumes (5 and 15 nm) are fixed. The bulk region expands with lowered pressure at a rate faster than that in conventional reservoirs. The bubble point pressure for shale is marked as an open blue square, and for conventional reservoirs it is marked as a green circle.[76]

4.2.5 Apparent bubble point

The reservoir fluids behave quite differently in the broad pore size distribution (nanometers to a few micrometers) of shale porous structure. The fluid evaporation/condensation pressure in nanopores is commonly lower than the bulk saturation pressure due to the confinement effect. The lowered phase transition pressures of pure fluids in nano-capillaries have been well recorded in isothermal adsorption experiments[8,11] and simulation studies.[41] For the multicomponent shale reservoir fluids, the vaporization in nanopores is further suppressed by the compositional extraction of light components (e.g. C_1, C_2) into the gas phase of the bulk region. In the simulated CCE, the liquid-vapor transitions are completely suppressed in 5 and 15 nm pores, i.e. the fluids in nanopores are undersaturated throughout the reservoir depletion. On the other hand, the

first bubble of shale oil emerges from the bulk region at a deviated pressure from the single-scale bulk bubble point.

For the multi-scale shale system, we suggest the term “apparent bubble point pressure” as the pressure when the first bubble forms in a certain region of scale while the fluids in the remaining regions stay undersaturated. In the case of Eagle Ford oil, the first bubble always occurs in the bulk region while the fluids in nanopores remain in the liquid-state. As discussed, the apparent bubble point is associated with the onset of two-phase flow in the bulk porous geometries of shale (e.g. fractures) and the sharp rise of production GOR.

The apparent bubble point is rationalized to be dependent on the compositional distributions between the bulk region and nanopores. Due to the compositional heterogeneities, the apparent bubble point which occurs in the bulk region is slightly suppressed in the bulk-15 nm case (Figure 23). With the small-scale nanopores (e.g. 5 nm), the bubble point is further suppressed (Figure 28). The apparent bubble point pressures in shale are 2002 psia for the bulk-15 nm case and 1936 psia for the bulk-15 nm-5 nm case, which are lower than the bulk bubble point in the conventional reservoir (2074 psia).

5. SHALE RESERVOIR FLUIDS IN GAS INJECTION*

5.1 Gas injection for shale reservoirs

Due to the rapid decline of production rate, the shale wells suffer very low oil recovery compare to conventional reservoirs. For example, the oil recovery factor was in the range of 4-6% in Bakken play.[108] With a significant amount of resources remaining in the reservoir, improved/enhanced oil recovery (IOR/EOR) has attracted much interest. Gas injection shows high displacement efficiency and applicability to low permeability reservoirs, and is considered a potential approach for improved oil recovery in shale fluids production. In the previous studies, the injected gas species include CO2,[109-112] natural gas[113] and nitrogen.[114] However, most studies focus on simulations and experimental work. There are very few field operation results reported. Todd et al. reported the injection pilots in the Bakken formation and found that none of the wells have so far produced any incremental oil, probably due to the very early breakthrough.[115] On the other hand, EOG Resources disclosed that the by injecting natural gas, production increases on 15 wells were gained in 30 to 70%. In another 32-well test, 300,000 bbl of oil were produced at the cost of $6/bbl through gas injection.[116]

* Part of this chapter is reprinted with permission from "Effect of Nano-Scale Pore Size Distribution on Fluid Phase Behavior of Gas IOR in Shale Reservoirs" by S. Luo, J. L. Lutkenhaus, and H. Nasrabadi, 2018. SPE Proceedings, SPE-190246-MS, Copyright [2018] by Society of Petroleum Engineers.

There are several challenges for gas injections in shale reservoirs, which include unknown phase behavior, low permeability and complex hydraulic/natural fracture systems.[117-119] The challenge in phase behavior is resulted from the broad pore size distribution in shale reservoirs. In gas injection, the phase behavior is critical in assessing swelling effect, gas solubility and minimal miscible pressure (MMP). As discussed in the previous chapter, the fluid phase behavior in shale reservoirs is multi-scale: in fractures and macropores (>50 nm), fluid behaves the same as bulk; in nanopores (<50 nm), the phase behavior deviates significantly from the bulk behavior by confinement effect. However, to the best knowledge, there are very few studies considers the confinement-induced phase behavior deviation in gas injection for shale reservoirs. The bulk fluid thermodynamics, such as Peng-Robinson EOS, is the most used approach in reservoir simulations for gas injections for shale reservoirs.[109,111]

In this chapter, the phase behavior in gas injection is investigated in two models. Firstly, the multi-scale constant composition expansion (CCE) processes is studied for the mixture of original oil and injected gas. The bubble point and volumetrics are discussed. Next, the swelling of nanopore-fluid is simulated. The gas is injected into a specific nanopore and the phenomenon that fluid swells out of the pore is investigated.

5.2 Multi-scale PVT of original oil and gas mixture

5.2.1 Case description

A case of Anadarko basin black oil is used as the original oil in reservoir before gas injection. The initial reservoir pressure is assumed as 5000 psia and the pore size distribution is V_{bulk}:V_{15nm}:V_{5nm}=3:2:1. The reservoir fluid has a bubble point of 2000 psia under bulk PVT conditions. The reservoir conditions are shown in Table 12.[120]

Table 12. Reservoir conditions of an Anadarko basin formation.[120]

Properties	Value
Initial Reservoir Pressure	5000 psia
Reservoir Temperature	165 ^{o}F
Initial V_{bulk}:V_{15nm}:V_{5nm}	3:2:1
Reservoir Fluid Type	Black Oil
Current Reservoir Pressure	2000 psia
Injected Fluid	Gas (methane)

The fluid properties used in PR-C EOS are listed in Table 13 and 14. The confinement parameters (ε_p, δ_p) are determined from the κ factor in Chapter 3.2.2.

Table 13. PR-C EOS properties for Anadarko basin oil.[120]

Species	MW (g/mol)	T_C (R)	P_C (psia)	ω	VSP	ε_p/k_B (K)	δ_p/σ	Mole Fraction
C_1	16.04	343.08	667.2	0.008	-0.0595	227	0.5	0.35354
C_2-CO_2-C_3	35.93	599.85	673.39	0.12156	-0.05381	747	0.5	0.14643
C_4-C_6	69.28	823.38	511.04	0.22632	-0.00866	1908	0.5	0.13527
C_7-C_{12}	116.61	1080.04	385.52	0.33607	0.15057	2108	0.5	0.18576
C_{13}-C_{22}	238.31	1389.92	206.2	0.69687	0.21568	2408	0.5	0.14544
C_{23+}	497.15	1733.72	111.27	1.20213	0.26619	2781	0.5	0.03356

Table 14. Binary interaction parameters for Anadarko basin oil.[120]

	C_1	C_2-CO_2-C_3	C_4-C_6	C_7-C_{12}	C_{13}-C_{22}	C_{23+}
C_1	0	0.005	0.019	0.039	0.081	0.122
C_2-CO_2-C_3	0.005	0	0.005	0.017	0.048	0.083
C_4-C_6	0.019	0.005	0	0.004	0.023	0.050
C_7-C_{12}	0.039	0.017	0.004	0	0.009	0.027
C_{13}-C_{22}	0.081	0.048	0.023	0.009	0	0.005
C_{23+}	0.122	0.083	0.050	0.027	0.005	0

5.2.2 Multi-Scale PVT of mixed fluid

The multi-scale phase behavior model is used in studying the phase behavior of gas injection in shale reservoirs. The gas is injected into the multi-scale system and the fluid phase behavior is determined as the thermodynamic equilibria among different pores (Figure 31). The original oil and injected gas are mixed in the multi-scale system and the phase equilibrium is calculated as the minimized Helmholtz free energy of the total system. The constant composition expansion (CCE) is conducted for the gas injection under different ratios of original oil/injected gas mixing.

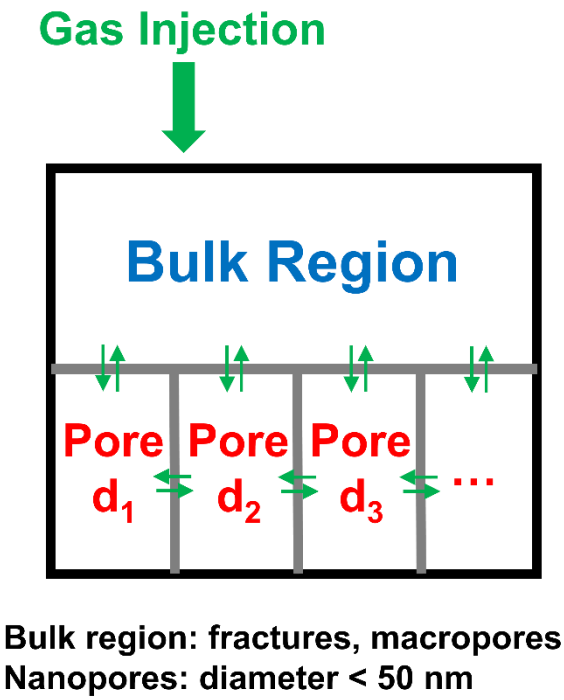

Figure 31. Multi-scale model for gas injections for fractured shale reservoirs. The gas injection operation adds light components into the system and the species distribute among different regions by multi-scale phase equilibrium.[120]

Firstly, the phase behavior of original reservoir fluid in the system with discretized sizes of nanopores is examined. The triple-scale constant composition expansion (CCE) of the original oil is simulated. As shown in Figure 32, the bubble point is 1821 psia, which is lower than the bubble point (2000 psia) of bulk fluid. As the pressure is further lowered, the fluid remain undersaturated in 5 and 15 nm nanopores. There are less heavy components (C_{13}-C_{22}, C_{23+}) in nanopores due to the nano-confinement effect. Upon entering the two-phase state in the bulk region, light components (C_1, C_2-CO_2-C_3) are released from the liquid phases in nanopores to the vapor phase in the bulk region. At the

end (1002 psia), the intermediate and heavy components (C_4-C_6, C_7-C_{12}, C_{13}-C_{22}, C_{23+}) are retained in the nanopores, which suggests an oil loss by the nanopores in production.[76,120]

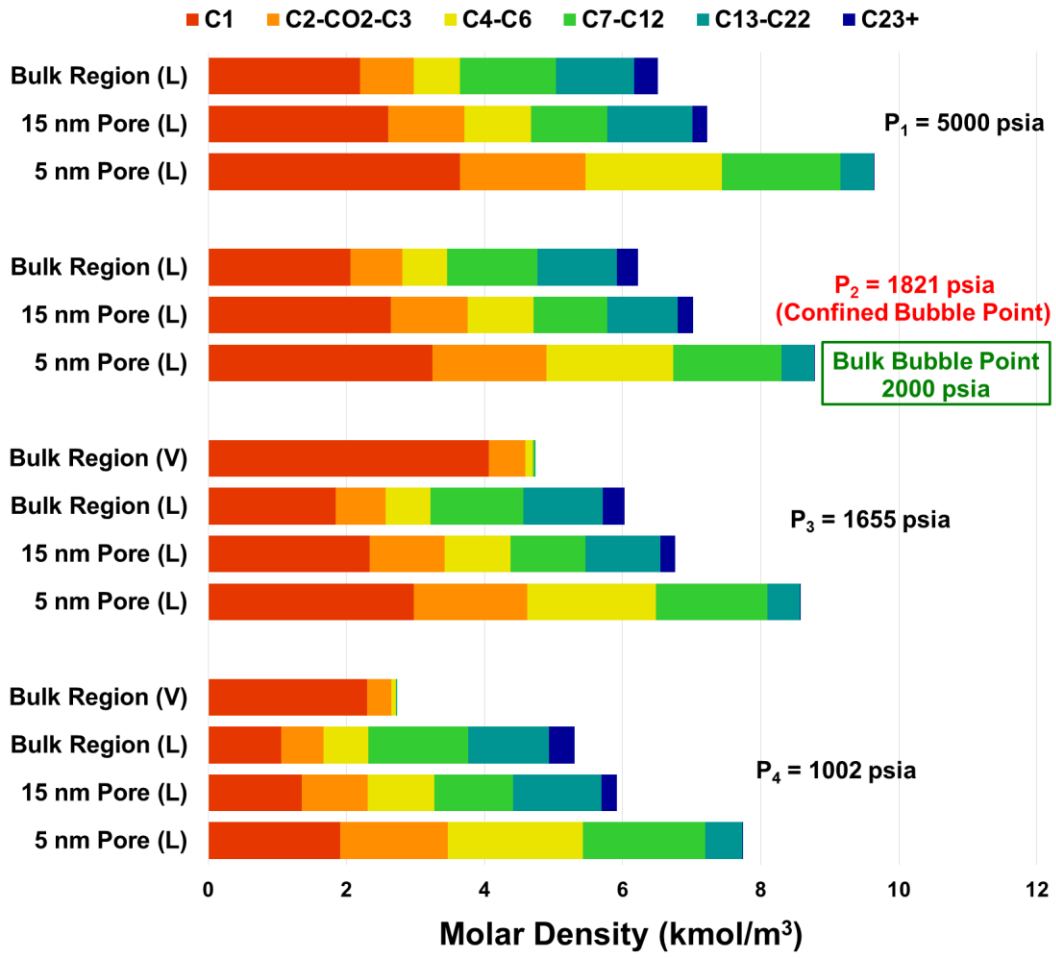

Figure 32. Original reservoir fluid molar density profiles of all phases at selected pressures in the triple-scale confined constant composition expansions. The length of a cylinder section refers to the actual molar density (kmol/m^3) of a specific species in the corresponding phase. V denotes the vapor phase, and L denotes the liquid phase.[120]

Next, the CCE processes for the reservoir fluid mixed with injected gas is studied. For the case of 22.3 mol% injected gas (overall 50 mol% C_1) (Figure 33), similar behavior is observed as the original oil. The fluid in 5 and 15 nm pores remains undersaturated throughout the process. The bubble point is 2935 psia. It's worth noting that at 5000 psia

in 5 nm pores, the fluid is at supercritical state. The supercriticality is associated with the increased mole fraction of light components C_1 in the system. Also, the nano-scale confinement contributes to a decrease of critical temperature,[7,50,76] and fluid in the smallest 5 nm pores enters the supercritical state first. As the pressure decreases, the fluid in 5 nm pores turns to liquid-state.[120]

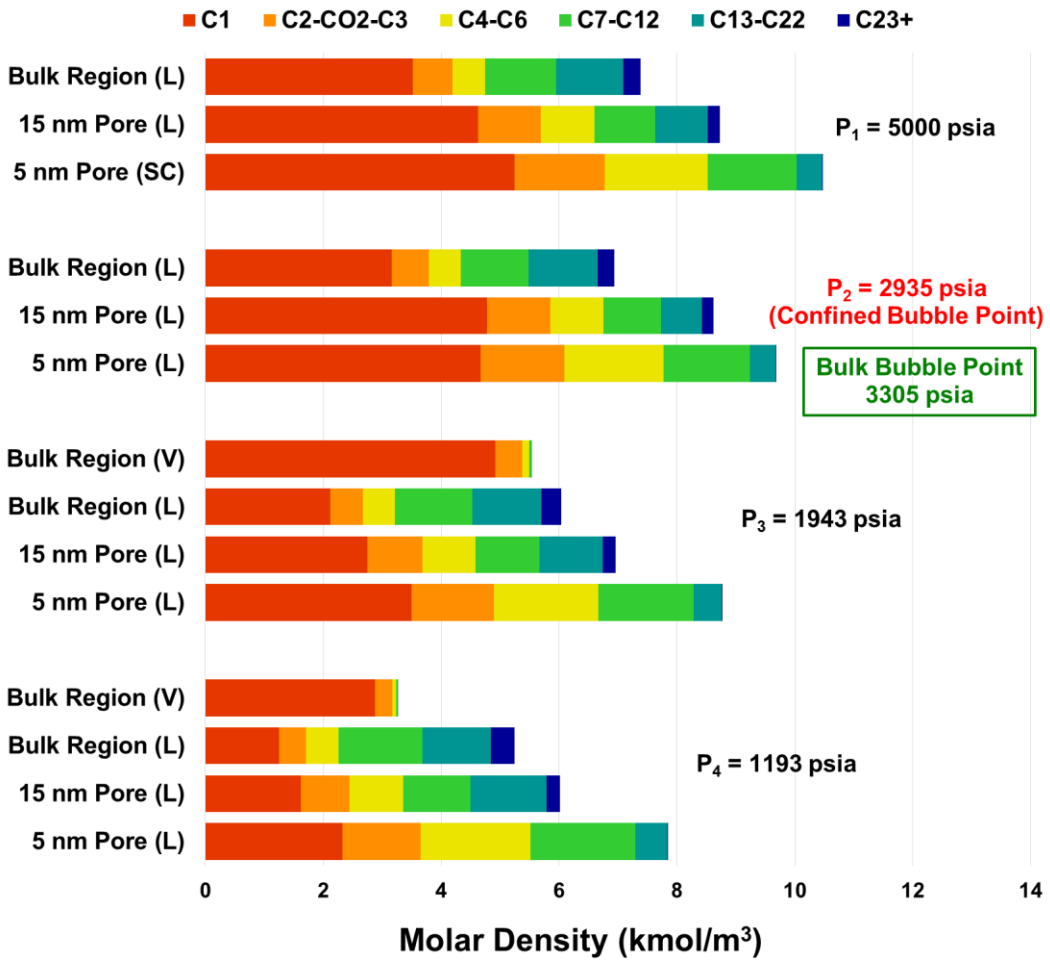

Figure 33. Reservoir fluid mixture with 22.3 mol% injected gas (overall 50 mol% C_1) molar profiles of all phases at selected pressures in the triple-scale confined constant composition expansions. The length of a cylinder section refers to the actual molar density (kmol/m3) of a specific species in the corresponding phase. V denotes the vapor phase, and L denotes the liquid phase. SC stands for supercritical state.[120]

Supercritical state fluid is observed at multiple stages for the fluid mixture with 53.6 mol% injected gas (overall 70 mol% C_1) (Figure 34). As discussed above, this is attributed to the increased mole fraction of C_1 in the whole system. It is observed that the bubble point is 6054 psia in the triple-scale confined system, 968 psia lower than the bubble point of bulk-state reservoir fluid. Fluid in both 5 and 15 nm pores are in the supercritical state above or slightly below bubble point. However, as the pressure is lowered, the fluid turns into the subcritical state, because the light and intermediate components are released from the nanopores and accumulate in the vapor phase in the bulk region.[120]

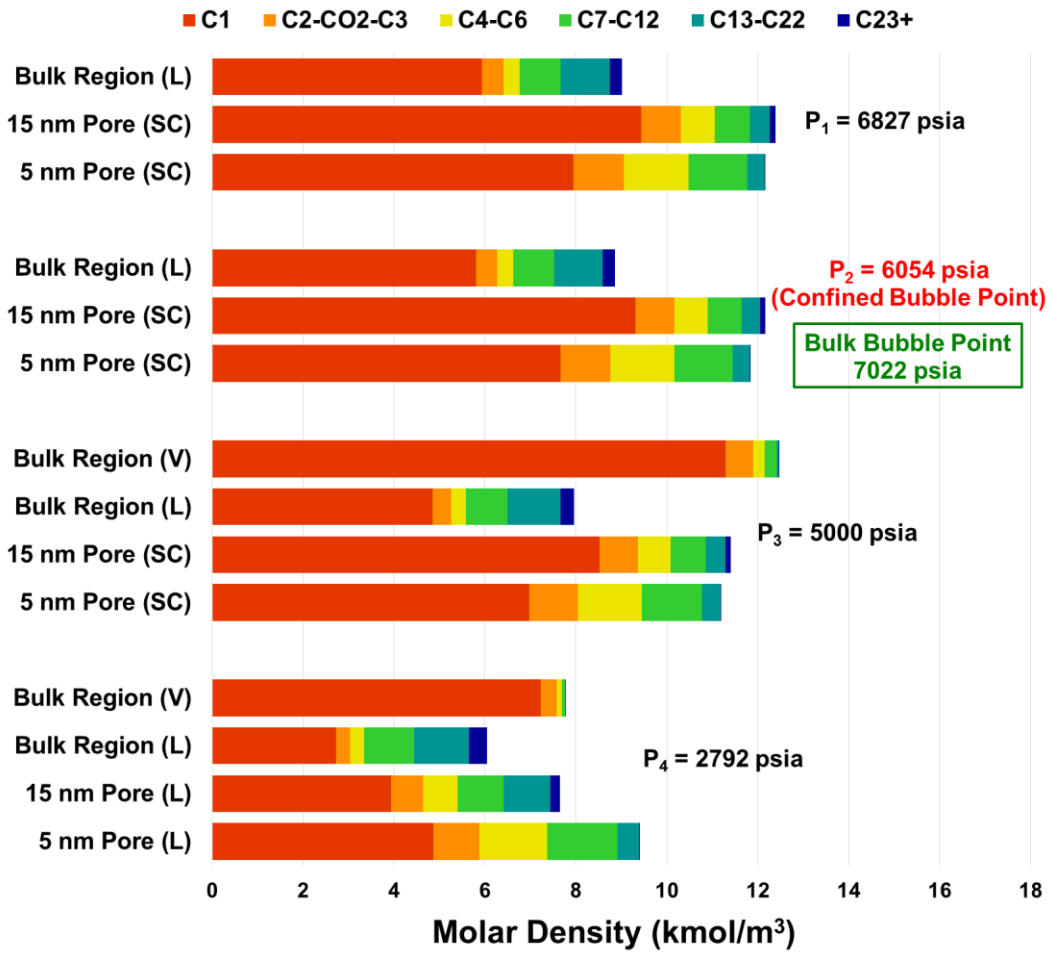

Figure 34. Reservoir fluid mixture with 53.6 mol% injected gas (overall 70 mol% C_1) molar density profiles of all phases at selected pressures in the triple-scale confined constant composition expansions. The length of a cylinder section refers to the actual molar density (kmol/m^3) of a specific species in the corresponding phase. V denotes the vapor phase, and L denotes the liquid phase. SC stands for supercritical state.[76]

Herein, the relative volume (RV) is defined as Eq. (5.1), where V is the sum of pore volumes for all sizes.

$$RV = \frac{V(T,P)}{V(T,P_b)} \tag{5.1}$$

Generally, relative volume curves of the confined shifted to the lower than the bulk relative volume curves (Figure 35). It is also worth noting that the distance between the confined

and bulk curve narrows in the two-phase stage. It indicates that the total volume of the confined fluid increases very fast. This behavior is due to the fast increase of gas saturation, which is also observed in the Chapter 4.2.[76]

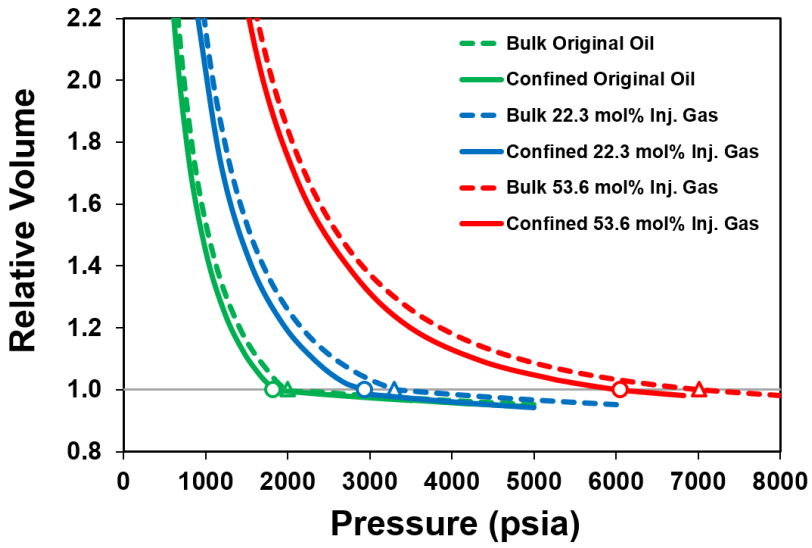

Figure 35. Relative volume – pressure relation for the CCE tests with or without injected gas. The circles and triangles show the bubble points of corresponding cases. The relative volume of confined fluid is the sum of fluid volumes of all sizes of pores.[120]

The bubble point of the reservoir oil and injected gas mixture has a generally lower bubble point than the bulk-state bubble point (Figure 36). At low fractions of injected gas, the bubble point decrease is as small as 200 psia. However, with the higher fractions of injected gas, the nano-confinement effect becomes greater. At 60 mol% injected gas, the bubble point is ca. 1000 psia below bulk bubble point. The critical pressure of the bulk fluid mixture is 10203 psia (62.5 mol% injected gas). Above the critical point, the reservoir fluid is gas condensate. However, for the multi-scale confined system, the fluid exhibits phase changes into the supercritical state in nanopores at lower mole fractions of injected gas (Figures 33-34).[120]

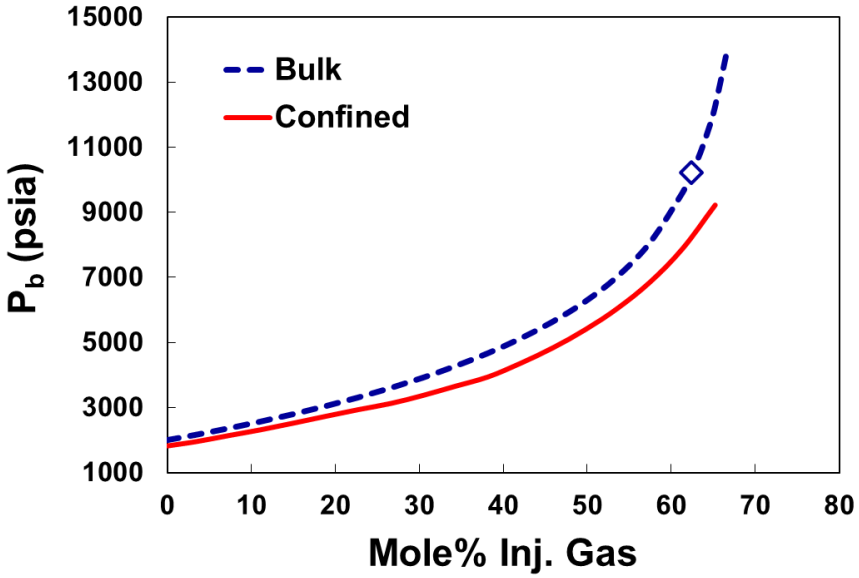

Figure 36. Bubble point pressure with respect to mole fractions of injected gas. The red line is confined fluid in the V_{bulk}:V_{15nm}:V_{5nm}=3:2:1 system, and the blue line is bulk fluid. The diamond symbol denotes the critical point of bulk fluid.[120]

5.3 Nanopore-Fluid swelling

In the previous section, the model is that gas is injected into multi-scale system. Next, the gas injection into a single-scale nanopore is simulated. The object of part is to probe the behavior of nanopore's fluid expanding into the bulk region. As shown in Figure 37, the gas is injected into the nanopore and mixes with the original pore-fluid. Under the swelling effect, the fluid in the nanopore expands into the bulk region (macropores and fractures) and the swelled fluid is envisioned to further flow into the well stream.

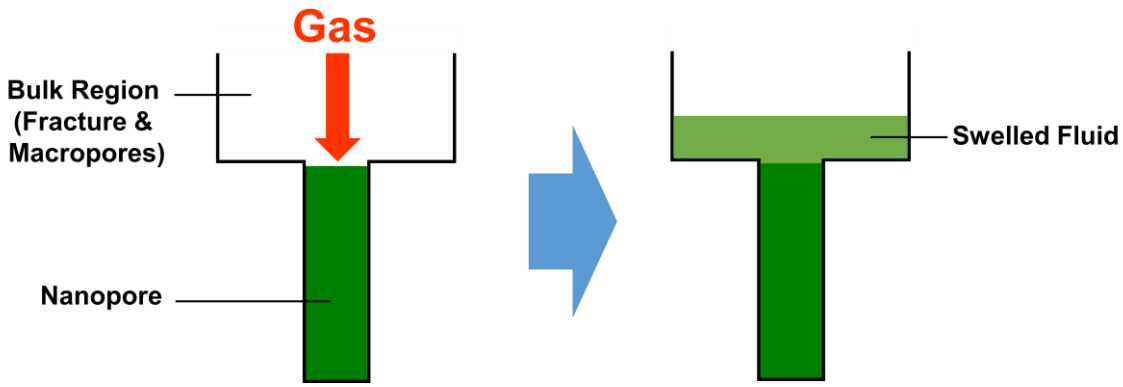

Figure 37. Gas injection into a nanopore and confined fluid swelling.

Based on the model, a swelling ratio is defined as:

$$Swelling\ Ratio = \frac{V_{swelled} + V_{nanopore\ residual}}{V_{nanopore\ original}} \tag{5.2}$$

The case described in Chapter 5.2.1 is used. 20 mol% gas (methane) is injected into the nanopores at 4000 psia at the state given by the original oil triple-scale CCE. Multi-stage separator conditions are applied: (200 psia, 100 ^{o}F) → (50 psia, 80 ^{o}F) → stock tank.

Firstly, gas injection into 15 nm pore by the fraction of 20 mol% is studied (Figure 38). The swelling of bulk state oil is simply a mixing effect of oil and injected gas, and the compositions are therefore given by dilution. However, due to the compositional heterogeneity between the nanopore and the bulk region, the swelling behavior is different. The swelling ratios are nearly the same (swelling ratio 1.11) but the swelled fluid from 15 nm pore has more heavy ends (C_{7+}) and C_1. This indicates that under confinement effect, the volumetrical behavior is almost the same between confined and bulk systems, but there are more oil extracted from the nanopore. Under the multi-stage separator conditions, the

swelled oil has a smaller volume formation factor (B_o) and solution gas/oil ratio (R_s) (Table 15).

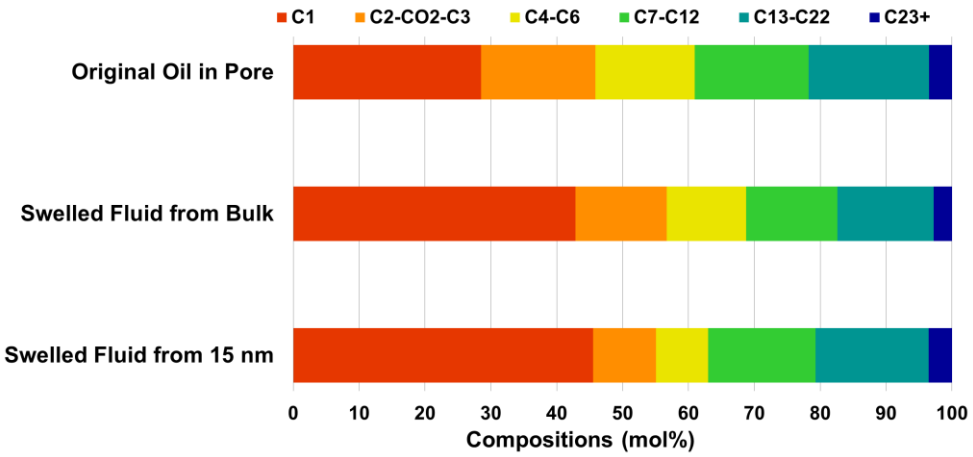

Figure 38. Swelled fluid: bulk state vs 15 nm (original oil mixed with 20 mol% injected gas at 4000 psia).

Next, gas injection into 5 nm pore is investigated (Figure 38). Similar to the results with 5 nm pore, the swelled fluid has more heavy ends (C_{7+}) and C_1. Overall, the swelled fluid has more oil since B_o and R_s are smaller than those in the bulk state swelling (Table 15). The volumetric expansion is slightly greater for bulk fluid, where the swelling ratio is 1.17, compared to the confined swelling ratio of 1.13.

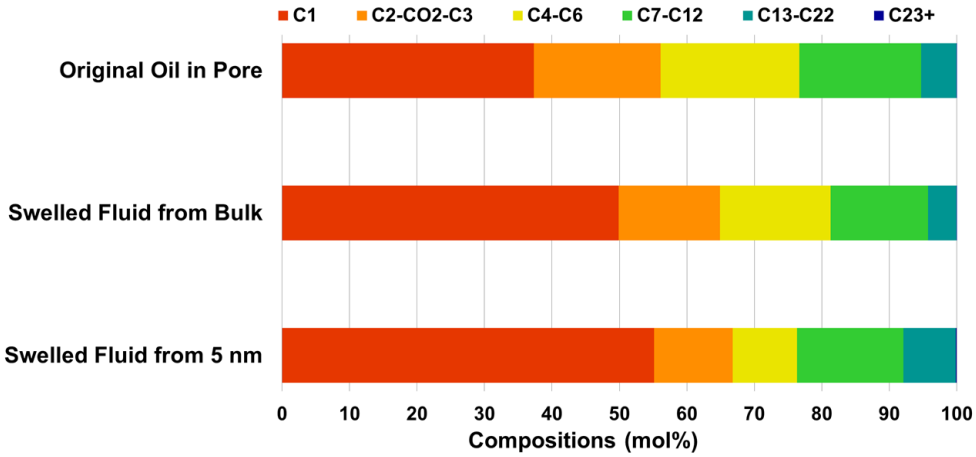

Figure 39. Swelled fluid: bulk state vs 5 nm (original oil mixed with 20 mol% injected gas at 4000 psia).

Table 15. Properties of swelled fluid (original oil mixed with 20 mol% injected gas).

Case	Injection into 15 nm Pore		Injection into 5 nm Pore	
Confinement	Bulk State	15 nm	Bulk State	5 nm
Swelling Ratio	1.11	1.11	1.17	1.13
B_o (rb/stb)	1.51	1.33	2.01	1.83
R_s (scf/stb)	1008	704	1885	1634

6. SUMMARY

6.1 Summary and conclusions

6.1.1 Summary

In this work, we have explored the phase behavior of nano-confined hydrocarbons by both experimental and theoretic methods. It has been clearly shown by experiments that the fluid confined in nanopores behaves significantly different from the fluid at bulk state. The equation of state simulations suggest that the petroleum fluids behavior in shale is highly heterogeneous because of the nano-scale pore size distribution. The conventional bulk thermodynamics is not applicable for liquid-rich shale reservoirs. Molecule-based simulations or theories are highly desired.

6.1.2 Experimental studies

Differential scanning calorimetry (DSC) is a useful method for measuring the phase transition temperature of confined hydrocarbons in nanopores. Silica-based nanoporous media can effectively serve as hosts for hydrocarbons. By studying the bubble point temperatures of hydrocarbon in different sizes of nanopores, it is found that at 40 nm or above, the fluid phase behavior is very close to bulk; as the pore size decreases, the fluid phase behavior deviates from the bulk and the confined bubble point increases; at small pore sizes (e.g. less than 4 nm), the phase behavior undergoes an alteration, which is observed as bubble point decreases with decreasing of pore size. Theoretical studies suggest that the alteration is associated with the confinement induced supercriticality.

The phase behavior is found to be affected by several factors, such as pore loading, pore size distribution and surface property. As the pore loading decreases, the bubble point temperature decreases. In the pore size distribution system, the fluid fills the small nanopores prior to filling the large pores. On native silica or trimethylsilylated silica, the confined hydrocarbons show different levels of deviations. Besides, for fluid mixtures in nanopores, it is inferred that there is a composition separation of a heavier surface-adsorbed phase and lighter confined-core phase.

6.1.3 Thermodynamic modeling

The molecule-based thermodynamics modeling is necessary in understanding the phase behavior of nano-confined fluid. The capillary pressure, which is based on the classic bulk thermodynamics, fails to model the experimental results. The pore-size-dependent equation of state, PR-C EOS, which is based on molecular description of fluid-pore wall interaction, successfully correlates to experimental results. The supercriticality induced by nanopores is also predicted by PR-C EOS, which correlates with an alteration of phase transition in experiments. The confinement parameters of PR-C EOS are determined from various hydrocarbons (C_1~C_{14}) based on experimental data.

In shale reservoirs, the macro- to nano-scale pore size distribution requires a specific strategy in modeling the fluid phase behavior. The fluid in the bulk region (macropores and fractures) behaves in the same way as bulk fluid; in the nanopores, the fluid phase behavior is significantly affected by the confinement effect. The pore-size-dependent

equation of state, PR-C EOS, gives a natural solution to model the multi-scale phase behavior in shale system. Fluid phase behavior in each pore is described by pore diameter and the multiscale phase equilibrium is calculated by minimizing the Helmholtz free energy.

The multi-scale constant compositions expansions are simulated for an Eagle Ford oil system. The compositional heterogeneity between different sizes of nanopores are observed, and as the pressure decreases, the bubble point is reached at a pressure ca. 100 psi lower than the bulk bubble point. The vapor phase only emerges from the bulk region, but the nanopores remains undersaturated to the end of depletion, which results in a significant oil recovery loss.

For the multi-scale phase behavior of gas injection, injected gas contributes to an increase in the fraction of light components and turns the fluid state towards critical point. Confinement effect further lowers the critical point, and the fluid in nanopores enters the supercritical state, in the order of small pores prior to large pores. The bubble points of nano-confined fluid mixtures are generally lower than those of bulk. From the nanopore-fluid swelling simulations, the extraction from nanopores is predicted to give more oil than the conventional swelling of bulk fluid.

6.2 Future work

Experimental studies in confined fluid mixtures will be highly valuable. Tests of fluid mixtures, especially crude oil, will very useful. Another good step is high pressure differential scanning calorimetry. The current instrument setup is limited to atmospheric pressure. High pressure test will bring the conditions towards the high pressure high temperature in reservoirs. The high pressure data will also be very valuable for validating thermodynamic models.

For the modeling work, molecular simulation and density functional theory can give insight to the fluid details in nanopores and also support equation of state modelings. These sophisticated methods are also very useful in probing the fluid mixing effect. The hysteresis effect is another object to look into, as the thermodynamic phase equilibrium may not hold in the nanoporous network, and the shale system may be controlled by the kinetics.

REFERENCES

1. *Annual Energy Outlook 2018 with projections to 2050*; U.S. Energy Information Administration: Washington, DC 205852018.
2. Civan, F.; Devegowda, D.; Sigal, R. Theoretical fundamentals, critical issues, and adequate formulation of effective shale gas and condensate reservoir simulation. *AIP Conf. Proc.* **2012,** *1453* (1), 155-160.
3. Du, L.; Chu, L. Understanding Anomalous Phase Behavior in Unconventional Oil Reservoirs. In *SPE Canadian Unconventional Resources Conference*; Society of Petroleum Engineers: Calgary, Alberta, Canada, 2012, pp SPE-161830-MS.
4. Nojabaei, B.; Johns, R. T.; Chu, L. Effect of Capillary Pressure on Phase Behavior in Tight Rocks and Shales. *SPE J.* **2013,** *16* (3), 281-289, SPE-159258-PA.
5. Whitson, C. H.; Sunjerga, S. PVT in Liquid-Rich Shale Reservoirs. In *SPE Annual Technical Conference and Exhibition*; Society of Petroleum Engineers: San Antonio, Texas, USA, 2012, pp SPE-155499-MS.
6. Ball, P. C.; Evans, R. Temperature dependence of gas adsorption on a mesoporous solid: capillary criticality and hysteresis. *Langmuir* **1989,** *5* (3), 714-723.
7. Thommes, M.; Findenegg, G. H. Pore Condensation and Critical-Point Shift of a Fluid in Controlled-Pore Glass. *Langmuir* **1994,** *10* (11), 4270-4277.
8. Russo, P. A.; Carrott, M. M. L. R.; Carrott, P. J. M. Hydrocarbons adsorption on templated mesoporous materials: effect of the pore size, geometry and surface chemistry. *New J. Chem.* **2011,** *35* (2), 407-416.

9. Russo, P. A.; Ribeiro Carrott, M. M. L.; Carrott, P. J. M. Trends in the condensation/evaporation and adsorption enthalpies of volatile organic compounds on mesoporous silica materials. *Microporous Mesoporous Mater.* **2012,** *151*, 223-230.

10. Qiao, S. Z.; Bhatia, S. K.; Nicholson, D. Study of Hexane Adsorption in Nanoporous MCM-41 Silica. *Langmuir* **2004,** *20* (2), 389-395.

11. Thommes, M.; Köhn, R.; Fröba, M. Sorption and pore condensation behavior of pure fluids in mesoporous MCM-48 silica, MCM-41 silica, SBA-15 silica and controlled-pore glass at temperatures above and below the bulk triple point. *Appl. Surf. Sci.* **2002,** *196* (1–4), 239-249.

12. Zhu, H. Y.; Ni, L. A.; Lu, G. Q. A Pore-Size-Dependent Equation of State for Multilayer Adsorption in Cylindrical Mesopores. *Langmuir* **1999,** *15* (10), 3632-3641.

13. Kuraoka, K.; Chujo, Y.; Yazawa, T. Hydrocarbon separation via porous glass membranes surface-modified using organosilane compounds. *J. Membr. Sci.* **2001,** *182* (1–2), 139-149.

14. Sing, K. S. W. Reporting physisorption data for gas/solid systems with special reference to the determination of surface area and porosity (Recommendations 1984). In *Pure and Applied Chemistry*, 1985; Vol. 57, p 603.

15. Rouquerol, J.; Avnir, D.; Fairbridge, C. W.; Everett, D. H.; Haynes, J. M.; Pernicone, N.; Ramsay, J. D. F.; Sing, K. S. W.; Unger, K. K. Recommendations

for the characterization of porous solids (Technical Report). In *Pure and Applied Chemistry*, 1994; Vol. 66, p 1739.

16. Lev, D. G.; Gubbins, K. E.; Radhakrishnan, R.; Sliwinska-Bartkowiak, M. Phase separation in confined systems. *Rep. Prog. Phys.* **1999,** *62* (12), 1573.

17. Floquet, N.; Coulomb, J. P.; Llewellyn, P. L.; André, G.; Kahn, R. Adsorption and neutron scattering studies: a reliable way to characterize both the mesoporous MCM-41 and the filling mode of the adsorbed species. In *Studies in Surface Science and Catalysis*, P.L. Llewellyn, F. R.-R. J. R.; Seaton, N., Eds.; Elsevier, 2007; Vol. Volume 160, pp 71-78.

18. Gruszkiewicz, M. S.; Rother, G.; Wesolowski, D. J.; Cole, D. R.; Wallacher, D. Direct Measurements of Pore Fluid Density by Vibrating Tube Densimetry. *Langmuir* **2012,** *28* (11), 5070-5078.

19. Alfi, M.; Nasrabadi, H.; Banerjee, D. Experimental investigation of confinement effect on phase behavior of hexane, heptane and octane using lab-on-a-chip technology. *Fluid Phase Equilib.* **2016,** *423*, 25-33.

20. Wang, L.; Neeves, K.; Yin, X.; Ozkan, E. Experimental Study and Modeling of the Effect of Pore Size Distribution on Hydrocarbon Phase Behavior in Nanopores. In *SPE Annual Technical Conference and Exhibition*; Society of Petroleum Engineers: Amsterdam, the Netherlands, 2014, pp SPE-170894-MS.

21. Alfi, M.; Nasrabadi, H.; Banerjee, D. In *Confinement effects on phase behavior of hydrocarbon in nanochannels*, ASME 2015 International Mechanical Engineering Congress and Exposition, 2015; American Society of Mechanical Engineers.

22. Aukett, P. N.; Quirke, N.; Riddiford, S.; Tennison, S. R. Methane adsorption on microporous carbons—A comparison of experiment, theory, and simulation. *Carbon* **1992,** *30* (6), 913-924.

23. Brown, A. J.; Burgess, C. G. V.; Everett, D. H.; Nuttall, S. *Characterisation of porous solids IV*; Cambridge: Royal Society of Chemistry1997.

24. Stroud, W. J.; Curry, J. E.; Cushman, J. H. Capillary Condensation and Snap-off in Nanoscale Contacts. *Langmuir* **2001,** *17* (3), 688-698.

25. Alharthy, N. S.; Nguyen, T.; Kazemi, H.; Teklu, T.; Graves, R. Multiphase Compositional Modeling in Small-Scale Pores of Unconventional Shale Reservoirs. In *SPE Annual Technical Conference and Exhibition*; Society of Petroleum Engineers: New Orleans, Louisiana, USA, 2013, pp SPE-166306-MS.

26. Wang, L.; Yin, X.; Neeves, K. B.; Ozkan, E. Effect of Pore-Size Distribution on Phase Transition of Hydrocarbon Mixtures in Nanoporous Media. *SPE J.* **2016,** *21* (6), 1981-1995.

27. Dong, X.; Liu, H.; Hou, J.; Wu, K.; Chen, Z. Phase Equilibria of Confined Fluids in Nanopores of Tight and Shale Rocks Considering the Effect of Capillary Pressure and Adsorption Film. *Ind. Eng. Chem. Res.* **2016,** *55* (3), 798-811.

28. Zhang, Y.; Yu, W.; Sepehrnoori, K.; Di, Y. Investigation of nanopore confinement on fluid flow in tight reservoirs. *J. Pet. Sci. Eng.* **2017,** *150*, 265-271.

29. Tan, S. P.; Piri, M. Equation-of-state modeling of associating-fluids phase equilibria in nanopores. *Fluid Phase Equilib.* **2015,** *405*, 157-166.

30. Tan, S. P.; Piri, M. Equation-of-state modeling of confined-fluid phase equilibria in nanopores. *Fluid Phase Equilib.* **2015,** *393*, 48-63.

31. Travalloni, L.; Castier, M.; Tavares, F. W.; Sandler, S. I. Thermodynamic modeling of confined fluids using an extension of the generalized van der Waals theory. *Chem. Eng. Sci.* **2010,** *65* (10), 3088-3099.

32. Travalloni, L.; Castier, M.; Tavares, F. W. Phase equilibrium of fluids confined in porous media from an extended Peng–Robinson equation of state. *Fluid Phase Equilib.* **2014,** *362*, 335-341.

33. Barbosa, G. D.; Travalloni, L.; Castier, M.; Tavares, F. W. Extending an equation of state to confined fluids with basis on molecular simulations. *Chem. Eng. Sci.* **2016,** *153*, 212-220.

34. Barbosa, G. D.; D'Lima, M. L.; Daghash, S. M. H.; Castier, M.; Tavares, F. W.; Travalloni, L. Cubic equations of state extended to confined fluids: New mixing rules and extension to spherical pores. *Chem. Eng. Sci.* **2018,** *184*, 52-61.

35. Li, Z.; Jin, Z.; Firoozabadi, A. Phase Behavior and Adsorption of Pure Substances and Mixtures and Characterization in Nanopore Structures by Density Functional Theory. *SPE J.* **2014,** *19* (6), SPE-169819-PA.

36. Jin, Z.; Firoozabadi, A. Thermodynamic Modeling of Phase Behavior in Shale Media. *SPE J.* **2016,** *21* (1), 190-207. SPE-176015-PA.

37. Singh, S. K.; Sinha, A.; Deo, G.; Singh, J. K. Vapor−Liquid Phase Coexistence, Critical Properties, and Surface Tension of Confined Alkanes. *J. Phys. Chem. C* **2009,** *113* (17), 7170-7180.

38. Singh, S. K.; Saha, A. K.; Singh, J. K. Molecular Simulation Study of Vapor−Liquid Critical Properties of a Simple Fluid in Attractive Slit Pores: Crossover from 3D to 2D. *J. Phys. Chem. B* **2010,** *114* (12), 4283-4292.

39. Singh, S. K.; Singh, J. K. Effect of pore morphology on vapor–liquid phase transition and crossover behavior of critical properties from 3D to 2D. *Fluid Phase Equilib.* **2011,** *300* (1–2), 182-187.

40. Jin, B.; Nasrabadi, H. Phase behavior of multi-component hydrocarbon systems in nano-pores using gauge-GCMC molecular simulation. *Fluid Phase Equilib.* **2016,** *425*, 324-334.

41. Walton, J. P. R. B.; Quirke, N. Capillary Condensation: A Molecular Simulation Study. *Molecular Simulation* **1989,** *2* (4-6), 361-391.

42. Quiñonero, D.; Frontera, A.; Deyà, P. M. Feasibility of Single-Walled Carbon Nanotubes as Materials for CO2 Adsorption: A DFT Study. *J. Phys. Chem. C* **2012,** *116* (39), 21083-21092.

43. Madani, S. H.; Hu, C.; Silvestre-Albero, A.; Biggs, M. J.; Rodríguez-Reinoso, F.; Pendleton, P. Pore size distributions derived from adsorption isotherms, immersion calorimetry, and isosteric heats: A comparative study. *Carbon* **2016,** *96*, 1106-1113.

44. Jackson, C. L.; McKenna, G. B. The melting behavior of organic materials confined in porous solids. *J. Chem. Phys.* **1990,** *93* (12), 9002-9011.

45. Wang, L.; Han, X.; Li, J.; Qin, L.; Zheng, D. Preparation of modified mesoporous MCM-41 silica spheres and its application in pervaporation. *Powder Technol.* **2012,** *231*, 63-69.

46. Lyons, W. C.; Plisga, G. J. *Standard handbook of petroleum & natural gas engineering*; 2nd ed.; Gulf Professional Pub.: Burlington, MA, Oxford, UK, 2005.

47. Luo, S.; Nasrabadi, H.; Lutkenhaus, J. L. Effect of confinement on the bubble points of hydrocarbons in nanoporous media. *AlChE J.* **2016,** *62* (5), 1772-1780.

48. Rennie, G. K.; Clifford, J. Melting of ice in porous solids. *J. Chem. Soc., Faraday Trans.* **1977,** *73* (0), 680-689.

49. Jackson, C. L.; McKenna, G. B. Vitrification and Crystallization of Organic Liquids Confined to Nanoscale Pores. *Chem. Mater.* **1996,** *8* (8), 2128-2137.

50. Luo, S.; Lutkenhaus, J. L.; Nasrabadi, H. Confinement-Induced Supercriticality and Phase Equilibria of Hydrocarbons in Nanopores. *Langmuir* **2016,** *32* (44), 11506-11513.

51. Li, Z.; Cao, D.; Wu, J. Layering, condensation, and evaporation of short chains in narrow slit pores. *J. Chem. Phys.* **2005,** *122* (22), 224701.

52. Wongkoblap, A.; Do, D. D.; Birkett, G.; Nicholson, D. A critical assessment of capillary condensation and evaporation equations: A computer simulation study. *J. Colloid Interface Sci.* **2011,** *356* (2), 672-680.

53. Makowski, W.; Kuśtrowski, P. Probing pore structure of microporous and mesoporous molecular sieves by quasi-equilibrated temperature programmed

desorption and adsorption of n-nonane. *Microporous Mesoporous Mater.* **2007,** *102* (1–3), 283-289.

54. Mittelmeijer-Hazeleger, M. C.; Van Der Linden, B.; Bliek, A. Temperature Programmed Desorption of n-nonane; the method to measure the micropore size distribution. *J. Porous Mater.* **1995,** *2* (1), 25-34.

55. Luo, S.; Lutkenhaus, J. L.; Nasrabadi, H. Use of differential scanning calorimetry to study phase behavior of hydrocarbon mixtures in nano-scale porous media. *J. Pet. Sci. Eng.* **2018,** *163*, 731-738.

56. Ma, Y.; Jamili, A. Modeling the density profiles and adsorption of pure and mixture hydrocarbons in shales. *J. Unconv. Oil Gas Resour.* **2016,** *14*, 128-138.

57. Lewis, R.; Singer, P.; Jiang, T.; Rylander, E.; Sinclair, S.; McLin, R. H. NMR T2 Distributions in the Eagle Ford Shale: Reflections on Pore Size. In *SPE Unconventional Resources Conference*; Society of Petroleum Engineers: The Woodlands, Texas, USA, 2013, pp SPE-164554-MS.

58. Vishnyakov, A.; Neimark, A. V. Studies of Liquid−Vapor Equilibria, Criticality, and Spinodal Transitions in Nanopores by the Gauge Cell Monte Carlo Simulation Method. *J. Phys. Chem. B* **2001,** *105* (29), 7009-7020.

59. Hartmann, M.; Vinu, A. Mechanical Stability and Porosity Analysis of Large-Pore SBA-15 Mesoporous Molecular Sieves by Mercury Porosimetry and Organics Adsorption. *Langmuir* **2002,** *18* (21), 8010-8016.

60. Kim, J.; Kwak, J.; Jun, S.; Ryoo, R. Ion-Exchange and Thermal-Stability of MCM-41. *J. Phys. Chem.* **1995,** *99* (45), 16742-16747.

61. Rouquerol, J.; Rouquerol, F.; Llewellyn, P.; Maurin, G.; Sing, K. S. W. *Adsorption by Powders and Porous Solids: Principles, Methodology and Applications*; 2nd ed.; Academic Press: Amsterdam; Boston; Heidelberg; London; New York; Oxford; Paris; San Diego; San Francisco; Singapore; Sydney; Tokyo, 2013. p 646.

62. Peng, D.-Y.; Robinson, D. B. A New Two-Constant Equation of State. *Industrial & Engineering Chemistry Fundamentals* **1976,** *15* (1), 59-64.

63. Fisher, L. R.; Israelachvili, J. N. Experimental studies on the applicability of the Kelvin equation to highly curved concave menisci. *J. Colloid Interface Sci.* **1981,** *80* (2), 528-541.

64. Shapiro, A. A.; Stenby, E. H. Thermodynamics of the multicomponent vapor–liquid equilibrium under capillary pressure difference. *Fluid Phase Equilib.* **2001,** *178* (1–2), 17-32.

65. Wang, Y.; Yan, B.; Killough, J. Compositional Modeling of Tight Oil Using Dynamic Nanopore Properties. In *SPE Annual Technical Conference and Exhibition*; Society of Petroleum Engineers: New Orleans, Louisiana, USA, 2013, pp SPE-166267-MS.

66. Wang, L.; Parsa, E.; Gao, Y.; Ok, J. T.; Neeves, K.; Yin, X.; Ozkan, E. Experimental Study and Modeling of the Effect of Nanoconfinement on Hydrocarbon Phase Behavior in Unconventional Reservoirs. In *SPE Western North American and Rocky Mountain Joint Meeting*; Society of Petroleum Engineers: Denver, Colorado, 2014, pp SPE-169581-MS.

67. Sing, K. S. W.; Williams, R. T. Historical aspects of capillarity and capillary condensation. *Microporous Mesoporous Mater.* **2012,** *154*, 16-18.

68. Danesh, A. S.; Dandekar, A. Y.; Todd, A. C.; Sarkar, R. A Modified Scaling Law and Parachor Method Approach for Improved Prediction of Interfacial Tension of Gas-Condensate Systems. In *SPE Annual Technical Conference and Exhibition*; Society of Petroleum Engineers: Dallas, Texas, USA, 1991, pp SPE-22710-MS.

69. Deshpande, R.; Smith, D. M.; Brinker, C. J. Preparation of high porosity xerogels by chemical surface modification. United States Patent US 5565142, 1996.

70. Petke, F. D.; Ray, B. R. Temperature dependence of contact angles of liquids on polymeric solids. *J. Colloid Interface Sci.* **1969,** *31* (2), 216-227.

71. Bernardin, J. D.; Mudawar, I.; Walsh, C. B.; Franses, E. I. Contact angle temperature dependence for water droplets on practical aluminum surfaces. *Int. J. Heat Mass Transfer* **1997,** *40* (5), 1017-1033.

72. Wilson, G. M. A modified Redlich-Kwong equation of state applicable to general physical data calculations. In *65th AIChE National Meeting*, 1968, p Paper No 15C.

73. Danesh, A. *PVT and phase behaviour of petroleum reservoir fluids*; Amsterdam; New York: Elsevier.1998.

74. Luo, S.; Lutkenhaus, J. L.; Nasrabadi, H. Experimental Study of Confinement Effect on Hydrocarbon Phase Behavior in Nano-Scale Porous Media Using Differential Scanning Calorimetry. In *SPE Annual Technical Conference and*

Exhibition; Society of Petroleum Engineers: Houston, Texas, USA, 2015, pp SPE-175095-MS.

75. Travalloni, L.; Castier, M.; Tavares, F. W.; Sandler, S. I. Critical behavior of pure confined fluids from an extension of the van der Waals equation of state. *J. Supercrit. Fluids.* **2010,** *55* (2), 455-461.

76. Luo, S.; Lutkenhaus, J. L.; Nasrabadi, H. Multi-Scale Fluid Phase Behavior Simulation in Shale Reservoirs by a Pore-Size-Dependent Equation of State. In *SPE Annual Technical Conference and Exhibition*; Society of Petroleum Engineers: San Antonio, Texas, USA, 2017, pp SPE-187422-MS.

77. Hoory, S. E.; Prausnitz, J. M. Monolayer adsorption of gas mixtures on homogeneous and heterogeneous solids. *Chem. Eng. Sci.* **1967,** *22* (7), 1025-1033.

78. Cabral, V. F.; Castier, M.; Tavares, F. W. Thermodynamic equilibrium in systems with multiple adsorbed and bulk phases. *Chem. Eng. Sci.* **2005,** *60* (6), 1773-1782.

79. Choudhary, V. R.; Mantri, K. Temperature-Programmed Desorption of Benzene on Mesoporous Si−MCM-41, Na−AlSi−MCM-41, and H−AlSi−MCM-41. *Langmuir* **2000,** *16* (21), 8024-8030.

80. Millot, B.; Methivier, A.; Jobic, H. Adsorption of n-Alkanes on Silicalite Crystals. A Temperature-Programmed Desorption Study. *J. Phys. Chem. B* **1998,** *102* (17), 3210-3215.

81. Vega, L.; de Miguel, E.; Rull, L. F.; Jackson, G.; McLure, I. A. Phase equilibria and critical behavior of square-well fluids of variable width by Gibbs ensemble Monte Carlo simulation. *J. Chem. Phys.* **1992,** *96* (3), 2296-2305.

82. Singh, J. K.; Kwak, S. K. Surface tension and vapor-liquid phase coexistence of confined square-well fluid. *J. Chem. Phys.* **2007,** *126* (2), 024702.

83. Evans, R.; Marconi, U. M. B.; Tarazona, P. Fluids in narrow pores: Adsorption, capillary condensation, and critical points. *J. Chem. Phys.* **1986,** *84* (4), 2376-2399.

84. Firoozabadi, A. *Thermodynamics and Applications of Hydrocarbons Energy Production*; 1st ed.; McGraw-Hill Education: United States of America, 2015. p 496.

85. Dosseh, G.; Xia, Y.; Alba-Simionesco, C. Cyclohexane and Benzene Confined in MCM-41 and SBA-15: Confinement Effects on Freezing and Melting. *J. Phys. Chem. B* **2003,** *107* (26), 6445-6453.

86. Millot, B.; Méthivier, A.; Jobic, H.; Clemençon, I.; Rebours, B. Adsorption of Branched Alkanes in Silicalite-1: A Temperature-Programmed-Equilibration Study. *Langmuir* **1999,** *15* (7), 2534-2539.

87. Monnery, W. D.; Svrcek, W. Y.; Satyro, M. A. Gaussian-like Volume Shifts for the Peng−Robinson Equation of State. *Ind. Eng. Chem. Res.* **1998,** *37* (5), 1663-1672.

88. Matsumoto, A.; Misran, H.; Tsutsumi, K. Adsorption Characteristics of Organosilica Based Mesoporous Materials. *Langmuir* **2004,** *20* (17), 7139-7145.

89. Lourenço, M. A. O.; Siquet, C.; Sardo, M.; Mafra, L.; Pires, J.; Jorge, M.; Pinto, M. L.; Ferreira, P.; Gomes, J. R. B. Interaction of CO2 and CH4 with Functionalized Periodic Mesoporous Phenylene–Silica: Periodic DFT

Calculations and Gas Adsorption Measurements. *J. Phys. Chem. C* **2016,** *120* (7), 3863-3875.

90. Chapela, G. A.; Martínez-Casas, S. E.; Varea, C. Square well orthobaric densities via spinodal decomposition. *J. Chem. Phys.* **1987,** *86* (10), 5683-5688.

91. Carley, D. D. Thermodynamic properties of a square-well fluid in the liquid and vapor regions. *J. Chem. Phys.* **1983,** *78* (9), 5776-5781.

92. Zhao, X. S.; Lu, G. Q. Modification of MCM-41 by Surface Silylation with Trimethylchlorosilane and Adsorption Study. *J. Phys. Chem. B* **1998,** *102* (9), 1556-1561.

93. Loucks, R. G.; Reed, R. M.; Ruppel, S. C.; Jarvie, D. M. Morphology, Genesis, and Distribution of Nanometer-Scale Pores in Siliceous Mudstones of the Mississippian Barnett Shale. *J. Sediment. Res.* **2009,** *79* (12), 848-861.

94. Ko, L. T.; Loucks, R. G.; Ruppel, S. C.; Zhang, T.; Peng, S. Origin and characterization of Eagle Ford pore networks in the south Texas Upper Cretaceous shelf. *AAPG Bulletin* **2017,** *101* (3), 387-418.

95. Gale, J. F.; Laubach, S. E.; Olson, J. E.; Eichhubl, P.; Fall, A. Natural fractures in shale: A review and new observations. *AAPG bulletin* **2014,** *98* (11), 2165-2216.

96. Anders, M. H.; Laubach, S. E.; Scholz, C. H. Microfractures: A review. *Journal of Structural Geology* **2014,** *69, Part B*, 377-394.

97. Warpinski, N. Measurement of width and pressure in a propagating hydraulic fracture. *Society of Petroleum Engineers Journal* **1985,** *25* (01), 46-54.

98. Dahi-Taleghani, A.; Olson, J. E. Numerical modeling of multistranded-hydraulic-fracture propagation: Accounting for the interaction between induced and natural fractures. *SPE J.* **2011,** *16* (03), 575-581.

99. Kuila, U.; Prasad, M. Specific surface area and pore-size distribution in clays and shales. *Geophys. Prospect.* **2013,** *61* (2), 341-362.

100. Honarpour, M. M.; Nagarajan, N. R.; Orangi, A.; Arasteh, F.; Yao, Z. Characterization of Critical Fluid PVT, Rock, and Rock-Fluid Properties - Impact on Reservoir Performance of Liquid Rich Shales. In *SPE Annual Technical Conference and Exhibition*; Society of Petroleum Engineers: San Antonio, Texas, USA, 2012, pp SPE-158042-MS.

101. Cho, Y.; Eker, E.; Uzun, I.; Yin, X.; Kazemi, H. Rock Characterization in Unconventional Reservoirs: A Comparative Study of Bakken, Eagle Ford, and Niobrara Formations. In *SPE Low Perm Symposium*; Society of Petroleum Engineers: Denver, Colorado, USA, 2016, pp SPE-180239-MS.

102. Warren, J.; Root, P. J. The behavior of naturally fractured reservoirs. *Society of Petroleum Engineers Journal* **1963,** *3* (03), 245-255.

103. Gilman, J. R.; Kazemi, H. Improvements in simulation of naturally fractured reservoirs. *Society of Petroleum Engineers Journal* **1983,** *23* (04), 695-707.

104. Bear, J.; Tsang, C.-F.; Marsily, G. d. *Flow and contaminant transport in fractured rocks*; Academic Press, San Diego, CA (United States): New York, NY., 1993.

105. Choi, E. S.; Cheema, T.; Islam, M. R. A new dual-porosity/dual-permeability model with non-Darcian flow through fractures. *J. Pet. Sci. Eng.* **1997,** *17* (3), 331-344.

106. Orangi, A.; Nagarajan, N. R.; Honarpour, M. M.; Rosenzweig, J. J. Unconventional Shale Oil and Gas-Condensate Reservoir Production, Impact of Rock, Fluid, and Hydraulic Fractures. In *SPE Hydraulic Fracturing Technology Conference*; Society of Petroleum Engineers: The Woodlands, Texas, USA, 2011, pp SPE-140536-MS.

107. Jones, R. S., Jr. Producing-Gas/Oil-Ratio Behavior of Multifractured Horizontal Wells in Tight Oil Reservoirs. *SPE Reservoir Evaluation & Engineering* **2017,** *20* (03), 589-601.

108. Hawthorne, S. B.; Gorecki, C. D.; Sorensen, J. A.; Steadman, E. N.; Harju, J. A.; Melzer, S. Hydrocarbon mobilization mechanisms from upper, middle, and lower Bakken reservoir rocks exposed to CO2. In *SPE Unconventional Resources Conference Canada*; Society of Petroleum Engineers: Calgary, Alberta, Canada, 2013, pp SPE-167200-MS.

109. Alharthy, N.; Teklu, T. W.; Kazemi, H.; Graves, R. M.; Hawthorne, S. B.; Braunberger, J.; Kurtoglu, B. Enhanced oil recovery in liquid-rich shale reservoirs: laboratory to field. *SPE Reservoir Evaluation & Engineering* **2017,** *21* (1), 137-159.

110. Chen, C.; Balhoff, M. T.; Mohanty, K. K. Effect of reservoir heterogeneity on primary recovery and CO2 Huff'n'Puff recovery in shale-oil reservoirs. *SPE Reservoir Evaluation & Engineering* **2014,** *17* (03), 404-413.

111. Yu, W.; Lashgari, H. R.; Wu, K.; Sepehrnoori, K. CO2 injection for enhanced oil recovery in Bakken tight oil reservoirs. *Fuel* **2015,** *159* (Supplement C), 354-363.

112. Phi, T.; Schechter, D. CO2 EOR Simulation in Unconventional Liquid Reservoirs: An Eagle Ford Case Study. In *SPE Unconventional Resources Conference*; Society of Petroleum Engineers: Calgary, Alberta, Canada, 2017, pp SPE-185034-MS.

113. Hoffman, B. T. Comparison of Various Gases for Enhanced Recovery from Shale Oil Reservoirs. In *SPE Improved Oil Recovery Symposium*; Society of Petroleum Engineers: Tulsa, Oklahoma, USA, 2012, pp SPE-154329-MS.

114. Yu, Y.; Sheng, J. J. Experimental Investigation of Light Oil Recovery from Fractured Shale Reservoirs by Cyclic Water Injection. In *SPE Western Regional Meeting*; Society of Petroleum Engineers: Anchorage, Alaska, USA, 2016, pp SPE-180378-MS.

115. Todd, H. B.; Evans, J. G. Improved Oil Recovery IOR Pilot Projects in the Bakken Formation. In *SPE Low Perm Symposium*; Society of Petroleum Engineers: Denver, Colorado, USA, 2016, pp SPE-180270-MS.

116. Rassenfoss, S. Shale EOR Works, But Will It Make a Difference? *Journal of Petroleum Technology* **2017,** *69* (10), 34-40.

117. Yan, B.; Killough, J. E.; Wang, Y.; Cao, Y. Novel Approaches for the Simulation of Unconventional Reservoirs. In *Unconventional Resources Technology Conference*: Denver, Colorado, USA, 2013, pp 1304-1313.

118. Wang, L.; Tian, Y.; Yu, X.; Wang, C.; Yao, B.; Wang, S.; Winterfeld, P. H.; Wang, X.; Yang, Z.; Wang, Y.; Cui, J.; Wu, Y.-S. Advances in improved/enhanced oil recovery technologies for tight and shale reservoirs. *Fuel* **2017,** *210*, 425-445.

119. Yan, B.; Mi, L.; Wang, Y.; Tang, H.; An, C.; Killough, J. E. Mechanistic Simulation Workflow in Shale Gas Reservoirs. In *SPE Reservoir Simulation Conference*; Society of Petroleum Engineers: Montgomery, Texas, USA, 2017, pp SPE-182623-MS.

120. Luo, S.; Lutkenhaus, J. L.; Nasrabadi, H. Effect of Nano-Scale Pore Size Distribution on Fluid Phase Behavior of Gas IOR in Shale Reservoirs. In *SPE Improved Oil Recovery Conference*; Society of Petroleum Engineers: Tulsa, Oklahoma, USA, 2018, pp SPE-190246-MS.